

Diss. ETH Nr. 14609

**Generalization of a 3-dimensional fault interaction model
including tectonics, fluids, and stress transfer**

A dissertation submitted to the
SWISS FEDERAL INSTITUTE OF TECHNOLOGY (ETH)
ZÜRICH

for the degree of
DOCTOR OF NATURAL SCIENCE

presented by
DELPHINE DANIELLE FITZENZ

Engineer Geophysicist
Institut de Physique du Globe (EPG), Strasbourg

born 6. June 1976

French citizen

Accepted on the recommendation of
Prof. Dr. Simon Löw, examiner
Dr. Stephen A. Miller, co-examiner
Prof. Dr. Domenico Giardini, co-examiner
Dr. Jacques Deverchère, co-examiner.

2002

Seite Leer /
Blank leaf

Preface

Un peu d'histoire - morceaux choisis:

Ne désespérons pas de la Science

C'est par le labeur constant et infatigable des savants dévoués au progrès, et souvent au milieu de l'injustice des hommes ignorants et aveugles, que la science avance graduellement dans ses nobles conquêtes. On entend tous les jours des sots et des ignares déblatérer contre la science et les savants, tout en prenant le chemin de fer ou le bateau à vapeur, en se servant du télégraphe, du téléphone, de l'électricité, sans avoir l'air de se douter que, sans les efforts des hommes laborieux qui ont créé les sciences pures et appliquées, ils seraient encore, aujourd'hui, de misérables troglodytes habitant les cavernes en compagnie des ours et des loups. La logique ne les gêne pas.

Malgré les travaux perpétuels et les recherches persévérantes des esprits dont nous parlons, auxquels l'humanité doit sa grandeur et sa gloire en même temps que son bien-être, les diverses branches de la science n'avancent pas uniformément. Il est bien remarquable, par exemple, que la connaissance du ciel a marché d'un pas beaucoup plus rapide que celle de la terre et que l'astronomie a toujours été considérablement en avance sur la géologie. Est-ce une raison pour tourner ces recherches en ridicule, comme on l'entend faire quelquefois?

On ne peut trouver qu'en cherchant. Bien des études, aujourd'hui fécondes en heureuses découvertes, ont demandé des centaines et des milliers d'années. L'électricité a été devinée -et nommée- au temps de Thalès il y a vingt-quatre siècles! Depuis combien de temps l'applique-t-on?

Admirons donc les chercheurs et soyons leur reconnaissants de leurs travaux, même infructueux. La science marche. Nous lui devons déjà tout ce que nous possédons. Elle nous réserve bien d'autres satisfactions, bien d'autres valeurs. Applaudissons tous les travailleurs.

Camille Flammarion (1842-1925).

Extrait d'un article publié dans le Petit Marseillais le 26 juin 1909, après le séisme de Lambesc du 11 juin 1909.

Natural Questions VI

Let us ask, then, what it is that moves the earth from the depths, what pushes such a great mass of weight; what is stronger than the earth that by its force it can shake so great a load. Let us investigate why the earth sometimes trembles, sometimes collapses and sinks, now is divided into sections and gapes open; why in one place it preserves for a long time the gap caused by its destruction, in other places it quickly compresses it again. Why at one time does it channel within itself rivers of noteworthy size, and at another time causes new rivers to appear. Why does it sometimes open veins of hot water, sometimes makes the water cold, and sometimes emits fire through a previously unknown opening of a mountain or a rock, but at other times suppresses fires that have been known and famous for ages? An earthquake produces a thousand strange things and changes the appearance of places and carries away mountains, elevates plains, pushes valleys up, raises new islands in the sea. What causes these things to happen is a subject worth investigating.

What, you ask, will make it all worth while? To know nature - no reward is greater than this. Although the subject has many features which will be useful, the study of this material has nothing more beautiful in itself than that it involves men in its magnificence and is cultivated not for profit but for its marvelousness.

Seneca (4 BC - 65 AD).

Naturales Quaestiones VI, 3.2-4.1

Corcoran, T.H. (Hg.): Seneca in ten volumes, vol. X: Naturales quaestiones I & II, Cambridge (Mass.) 1971-1972

Acknowledgments

This work has been conducted at the Swiss Federal Institute of Technology (Zürich) in the framework of a Swiss National Fund project led by Steve Miller, in the team of Engineering Geology chaired by Professor Löw. Some of the computations were performed on the SGI supercomputer of the EPFL.

None of this would have happened without some key people. I think first of my family (grand-parents, parents, sister, and relatives). Beyond the obvious reasons (one needs to exist to make a PhD ;-)), they provided me with two strong motos: “Quand on veut on peut” (when one wants, one can, or “where there is a will, there is a way”, as Steve would put it), and “il faut savoir se donner les moyens de ses ambitions” (you need to give yourself the means of realizing your ambitions). In other words, dreams can be fulfilled if you believe they can, and if you work hard enough. But this wouldn't have been enough. My family also represents an extraordinary, intarissable reservoir of positive waves!!

I can not write an exhaustive list of the people who influenced me, inspired me, or helped me. By the beginning of the last year of my studies, in Strasbourg, I already knew I wanted to study the link between rock physics, fluids, and seismic hazards. I tried hard to find a research project (diploma work) that would allow me to do that. And found nothing. I was about to give up the DEA (university master's degree, that I was preparing in parallel with the engineering master's) when Philippe Pezard convinced me to hold on and proposed me a very interesting subject on the evaluation of profiles of permeability and overpressure across the Barbados accretionary prism. After 8 months of interesting and intensive work, the hunt started again, for a PhD this time. I'd like to thank Anne-Marie Boullier and Jean-Pierre Gratier (as well as my friends Alain and Hamed from Montpellier, and Caro, and Véro from the LMF) for their support in that period. After realizing that I wouldn't find something in “my” preferred research field in France at that particular time, I looked at the web site of ETHZ. That was a lucky move. I found the homepage of Engineering Geology and the project of Steve. I contacted him (and David Estoppey. Thanks again David!!) and when I learned about the subject he was proposing I decided to lay siege to Steve (or at least to his mailbox) until I would get something. And this happened!! I got a great support from Philippe and from my former teachers in Strasbourg. Simon welcomed me in his group, and the adventure of this PhD started.

A small group of critical researchers of ETH, LGIT, and Nice kept an eye on my work and I thank them for that. These include Domenico Giardini, Alain Geiger, Yuri Pod-

ladchikov, Michel Bouchon, and Jacques Deverchère. Some others were kind enough to accept to communicate their (then) unpublished results on the Izmit earthquake, Bertrand Delouis, Jérôme Salichon, and Michel Bouchon.

The study of earthquake mechanics and the forward modeling of such phenomena require knowledge in a broad range of research fields. The workshop “Fault interaction by stress transfer” held in Erice in 2000 helped me greatly to understand some notions such as ... rate and state friction (!), because they were explained by the experts in each field, Jim Dieterich and Mike Blanpied in this example. I could meet and get a feedback on my work from Mark Zoback, Maria-Elena Belardinelli, Michel Bouchon, and others. That was a great experience, namely thanks to the kindness of the participants and to the organization of Massimo, Silvia, and Ross. In December that same year, giving a seminar at the USGS and staying three days talking to many researchers there was also utterly stimulating (though brain frying!!). Thanks to all of them.

Preparing talks or writing papers (or a thesis) is often done with a sense of emergency. I’d like to thank here my colleagues and flatmates who had to bear me :-). They helped me with their understanding, but also with their special skills. If I was to make a list, I’d start with Philippe Renard (UNIX, Latex), Volker (PC) and David (PC), Christian Z. (real fault zones, outcrops+photos), Christian K. (real faults in tunnels, real porosity, classification systems, geophysics/geology discussions + introduction to Mozart and others), Heike (german teacher! kondi-colleague), Dani (f90/matlab), Yuri (theory), Matt (seismicity figure), all the members of the Friday “pre-beer” seminars, Thomas (UNIX emergencies, e.g., last December from Stanford!), Igor Zacharov (SGI code optimization shortcourse), Jean-Michel Chenais and Trach-Minh Tran for their help with Eridan... Mike Blanpied, Greg Beroza, and Kaj should also be in this list. They enabled me to finish preparing my last AGU talk. My endless gratitude is theirs!

To be allowed to defend our PhD, we have to take classes outside our field of research. I’d like to thank Professor Vickers and his assistant Stefan for the great time (hmm sometimes too long time, when working on the exams, for example) I spent studying English literature. Thanks also for communicating your interest in earthquakes as seen by Seneca and others, Professor!

Mary Lou and Mark, Bill, Steve H., Mike, and Steve M. all encouraged me and helped me write a proposal for a post-doc, and Alan Green and Jean-Pierre Burg gave me their advices. Merci!

Have I mentioned how I enjoyed my work in Zürich during these 3 years and 3 months? It was not always easy (or usually not easy), rarely quiet, sometimes overwhelming, sometimes tense, sometimes exciting, sometimes depressing (have you ever tried installing an MPI network?), sometimes awful when doubts were stronger than confidence or when time was running short as pressure was increasing. Well, just a piece of life. Steve, these were 3 full years, oder? :-). Besides ice-skating, modern-dancing, yoga, karate, kondi, skating (oops!), sledging (re-oops!), and ... physiotherapy!

Finally, I'd like to thank Rita and Bettina; all Ingeols for a great time and solidarity (several injuries); all those who courageously took part in cooking experiments either at Josefstrasse or at the office, in particular Christian Z. and Auke; those who organized the superbe buffet and who helped for the party on my defense day, under the supervision of Heike; my friends, who leave far away, but were always present, Noura, Seb R., Seb G., Cedric M., Pauline et Cedric F., O., etc...; and my fan club secretary Danielle F..

Wow! that turns out to be a long list! Writing acknowledgements is something everybody should do when feeling blue. One can only be cheered up when realizing how numerous the people are who helped and counted in one's life!

Seite Leer /
Blank leaf

Table of contents

Preface	iii
Acknowledgments	v
Table of contents	ix
List of figures	xiii
List of tables	xxi
Abstract-Résumé	xxiii
Introduction and summary	xxvii
1 Elasticity and stress transfer: Theory and application to the Izmit (Turkey 1999) earthquake	1
1.1 Elasticity and dislocation theory	2
1.1.1 Elastostatics and dislocation theory in an infinite medium	3
1.1.2 Elastic half-space	6
1.2 Rock mechanics and stress transfer	7
1.2.1 Introduction to rock mechanics	7
1.2.2 Optimal orientation for failure	8
1.2.3 Change in Coulomb failure stress. Introduction to stress triggering .	10
1.3 Comment on regional stress	12
1.4 Application to the Izmit (1999, Turkey) M_w 7.4 earthquake	14
1.4.1 Location and slip distribution of the Izmit (Turkey, 1999) earthquake	15
1.4.2 Changes in volumetric strain and in Coulomb failure stress	15
1.5 Limits of the method	19
2 Forward model of earthquake generation on interacting faults including tectonics, fluids, and stress transfer	23
2.1 Introduction	24
2.2 The Model	26
2.2.1 Choice of Initial Conditions and Processes	28
2.2.2 The numerical model	31
2.3 Model Results	34

2.3.1	Seismicity Time Line and Frequency-Magnitude Statistics	34
2.3.2	Fault Stress State Evolution	35
2.3.3	Slip Vectors During Rupture	38
2.3.4	Fault Interaction: Separating the Effects of Shear Stress and Pore Pressure	41
2.3.5	Total Local Stress Direct Calculation	46
2.3.6	Map and Cross Sections of Δ CFS and Comparison with Seismicity Distribution	48
2.4	Discussion and Conclusions	51
2.4.1	Key Features of the Model	51
2.4.2	Advantages of the Model	51
2.4.3	Limitations of the Model	52
2.4.4	Conclusion and Future Perspectives	53
3	Fault compaction and overpressured faults: Results from a 3D model of a ductile fault zone.	55
3.1	Introduction	57
3.2	Conceptual model of fault zone hydraulics	59
3.3	The numerical model	61
3.3.1	A viscoelastic fault core: shear creep and compaction rate	62
3.4	3D model	68
3.4.1	Interseismic hydraulic property changes	70
3.4.2	Coseismic hydraulic property changes	70
3.4.3	New calculation of time steps	72
3.4.4	Results of the full 3D model and interpretation	73
3.5	Discussion	76
3.5.1	Controls on pore pressure evolution	76
3.5.2	Creep slip distribution	78
3.6	Conclusion and perspectives	79
4	Developing regional models of fault systems	81
4.1	Model developments	82
4.2	Constraints on tectonic loading and stress maps from a 3-dimensional forward fault interaction model including tectonics, fluids and stress transfer. Application to the Transpressional Big Bend area in Central California . .	82
4.2.1	Introduction	83
4.2.2	Tectonic set-up	84
4.2.3	Initial loading conditions	85
4.2.4	Ductile compaction and shear creep	87
4.2.5	Evolved stress state and seismicity on the model faults	87
4.2.6	Resulting regional tectonic evolution	91
4.2.7	Fluids	91
4.2.8	Conclusion	96
4.3	Appendix A: permeability evaluation	97
4.4	Appendix B: Interseismic in-plane fluid diffusion	97

5	Conclusions and perspectives	99
5.1	Summary of the principal results	100
5.1.1	From semi-forward stress transfer to a fluid-controlled forward model	100
5.1.2	Rheology and hydraulics of fault zones	100
5.1.3	Regional model	101
5.2	Methodological aspects	101
5.2.1	The quasi-static approach	101
5.2.2	A modular, flexible tool	102
5.3	Perspectives	102
5.3.1	Test of model hypotheses	102
5.3.2	Theoretical follow-ups	103
5.3.3	Investigation of, and coupling to, alternative models	104
5.3.4	Test against data, example of Central California	105
5.4	Concluding remark	105
	Bibliography	107
	Curriculum Vitae	117

Seite Leer /
Blank leaf

List of figures

1.1	Standard definition of fault-plane and slip-vector orientation parameters.	3
1.2	Interferogram showing deformation fringes for the Landers earthquake. One fringe corresponds to a displacement in the direction ground/satellite equals to one half of the wavelength of the radar. The patterns formed by interferogram fringes (top) and attributed to coseismic deformation were successfully modeled using planar dislocation sources (bottom) (from Massonnet et al., 1993).	4
1.3	Representation of rectangular dislocation planes as used by Okada (1985, 1992). The surface $z=0$ is the free surface. For each dislocation rectangle (shaded area) of any dip angle δ , a unique constant slip vector of any rake angle can be defined (slip normal to the plane, e.g., opening, is also possible).	7
1.4	A typical bi-axial laboratory experiment. When a rock sample is stressed (vertical maximum stress σ_1 , horizontal minimum stress σ_3), then a rupture plane develops at an angle β to σ_3 . On this plane, shear τ and normal σ_n stress can be defined. If the fault gouge contains fluids at a pressure P_f , the effective stress σ_{eff} is defined as $\sigma_n - P_f$. The three numbered plots show three ways to reach the Coulomb failure criterion represented by the bold line of slope $\mu = \tan(\phi)$, where μ is the friction of the rock.	9
1.5	Mohr circles: $n_i = constant$ define three families of circles in Mohr space. The circle $n_2 = 0$ defines the locus of maximum shear stress and we will consider $n_2 = 0$ for optimally oriented planes.	10
1.6	Investigating stress transfer: needed input and expected output	11
1.7	Coulomb failure stress changes ($\Delta CFS = \Delta\tau - \mu'\Delta\sigma_n$). Due to a nearby earthquake, normal and shear stress (and pore pressure by poroelasticity) can be perturbed at any location in the crust. We can interpret these changes in terms of variations in the proximity to failure. Positive values of ΔCFS mean that the point was brought closer to failure whereas negative values mean that it was taken further from the failure.	12

- 1.8 Simple stress transfer case: a right-lateral strike-slip displacement of 3 m on a rectangular vertical plane. (a) Strain and stress transfer. Strain changes are positive for dilatation and negative for compression, and normal stress changes are positive in extension and negative in compression (the color scale saturates at -1 and +1 bar to show the maximum lateral extend of potentially significant changes), (b) Optimal orientation for failure. The model parameters are the maximum principal stress $\sigma_1 = 100$ bars, oriented N125E, and the apparent friction coefficient $\mu' = 0.4$. The background blue color corresponds to the optimal orientation for failure in the presence of the regional stress only. We observe rotations up to 60° when the stress perturbation of the main event is added. Note: the slip is uniform on the rectangle, resulting in sharp singularities at the edges of the dislocation plane. 13
- 1.9 Historical seismicity of the North Anatolian fault and location of the August 17, 1999 Turkish earthquake (after Okumura et al., 1993). 14
- 1.10 Location and slip distribution of the Izmit earthquake (from Delouis et al., 2000). (a) Map of surface rupture. The position of the epicenter (near the city of Izmit) is indicated with an open triangle and the colored lines displays the location and magnitude of the main surface breaks. The surface projection of the model fault used for the inversion (Table 1.1) is also shown. (b) to (f) Slip distributions obtained by Delouis et al. (2000) with different data sets (SAR, SAR+surface offset, teleseismic, and teleseismic+surface offset, from top to bottom) and for the joint inversion (slip distribution that we use in the stress transfer study below). (g) Time history of the rupture. 16
- 1.11 The Izmit earthquake (August 1999), volumetric strain variations calculated at 12 km depth. The distances along the x axis are given with respect to the hypocenter location. The white dots show the aftershock location and the black star shows the hypocenter of the $M_w = 7.2$ Duzce earthquake (November 1999) 17
- 1.12 The Izmit earthquake (August 1999), optimal orientation for failure calculated at 12 km depth on vertical planes, with $\mu'=0.4$ and σ_1 oriented -35° to the East-West direction. The optimal orientations are essentially fixed by the regional stress except close to the fault ($\sim 10-15$ km) where the stress change caused by slip on the master fault is comparable to the regional stress. 18
- 1.13 The Izmit earthquake, Coulomb failure stress changes calculated at 12 km depth on the planes defined on Figure 1.12. (a) ΔCFS with $\mu'=0.2$, and (b) $\mu'=0.4$. The white dots show the aftershock hypocenters. The variation in μ' does not affect the shape of the ΔCFS patterns significantly. At distances greater than 20 km, the earthquake brought the crust further from failure but the complex patterns near the fault show areas of increased CFS 21

- 2.1 Model of a coupled blind-dipping, strike-slip fault system. The 3-D model is made of two faults discretized into computational cells, interacting through an elastic half-space, in a transpressional environment. Plate motion is imposed at the base of the seismogenic layer as a dislocation. The base is infinite in any direction, one edge being at the downward edge of the strike-slip fault. 27
- 2.2 Flowchart of model algorithm. The model includes quasi-static tectonic loading, fluid-saturated faults, fluid sources, elastic dislocation theory, poroelasticity in undrained conditions, small-scale coseismic changes in hydraulic properties, frictional dilatation, and monitoring of full stress tensor. (See text for more details.) 33
- 2.3 (left) Seismicity time line and (right) corresponding frequency-magnitude relationship for (top) the strike-slip fault and (bottom) the dipping fault. The minimum moment magnitude (M_w) is ~ 3.8 because of the size of the subfaults (or cells, i.e., 2 km along strike by 0.5 km along dip). M_w is calculated from the scalar seismic moment via equation (2.6). The maximum moment magnitude for the time window (~ 9300 years) studied is $M_w \sim 7.7$. The frequency-size statistics show that a wide range of event size are generated in this model with b -values ~ 1 for each fault. 34
- 2.4 Time evolution of the stress state (a-c) on the strike-slip fault and (d-f) on the dipping fault. The dipping fault is highly overpressured (the range in σ_{eff} is small). The stress state tends to fill the space available between the static friction and the line defined by the stress drop until a large rupture occurs and relieves the fault by dramatically reducing pore pressure. . . . 36
- 2.5 (a) Pore pressure compartments on the strike-slip fault at $t=1500$ years. The vertical axis is $\lambda = P_f/\sigma_n$. Its values range from 0.4 (e.g., at the top of the fault, referring to a hydrostatic pore pressure gradient) to values close to 0.9 (highly overpressured compartments). We note that the heterogeneity imposed in the pore pressure increase rate acts as noise superposed on significant heterogeneities due to slip and subsequent pore space creation and pore pressure redistribution. (b) Shear stress distribution on the strike-slip fault at the same time. (c) Pore pressure compartments on the dipping fault at $t=5400$ years. (d) Corresponding shear stress distribution. 37
- 2.6 Average properties of the faults versus time. (top) Mean shear stress, (middle) Mean effective stress, (bottom) Mean pore pressure. Each abrupt change in slope corresponds to a model earthquake. We notice the rather short onset of rupture on the strike-slip fault (bold lines) and how large events can reduce the mean shear stress but also, and to a larger extent, the mean pore pressure. Stress builds slowly on the dipping fault, and no earthquakes happen before the fault is highly overpressured. After 6000 years, both faults have reached a dynamic equilibrium (pseudo-steady state). 39

- 2.7 The propagation (a through f) of a large rupture ($M_w = 7.2$) occurring at $t=5541.78$ years on the strike-slip fault. The gray scale shows the cumulative slip, and the arrows show the change in the rake angle during the event (the updip component is shown with a vertical exaggeration of 10). Although the rupture initiates at $x=-82$ km, the rupture front “jumps” to $x=-60$ km and keeps on propagating. We can notice changes in the rake angle with rupture propagation. Note that the aspect ratio is not preserved. 40
- 2.8 Plate 1(a to f): Fault interaction. Pore pressure changes (first and third columns) and shear stress changes (second and fourth columns) on the strike-slip fault during the $M_w = 7.2$ event on the strike-slip fault. Changes in pore pressure are due both to poroelasticity (and hence to stress transfer during the rupture propagation) and to the redistribution of pore pressure itself. Changes in shear stress are due to the assumed stress drop and to the redistribution of stresses. Note different color bars for P_f for the two faults. 42
- 2.9 Plate 1(a to f): Fault interaction. Pore pressure changes (first and third columns) and shear stress changes (second and fourth columns) on the dipping fault (respectively) during the $M_w = 7.2$ event on the strike-slip fault. Changes in pore pressure are due both to poroelasticity (and hence to stress transfer during the rupture propagation) and to the redistribution of pore pressure itself. Changes in shear stress are due to the assumed stress drop and to the redistribution of stresses. Note different color bars for P_f for the two faults. 43
- 2.10 Local stress. Principal components are on a horizontal plane at 8.5 km depth for $t=9300$ years. The gray scale shows the angle of σ_1 with respect to the strike of the faults. The arrows show the directions of the principal stresses. Note that σ_2 is mostly vertical but that σ_3 can also be the vertical stress, denoting a transpressional regime. 47
- 2.11 Plate 2. Static changes in Coulomb failure stress on optimally oriented vertical planes at 8.5 km depth after the same $M_w = 7.2$ event on the strike-slip fault: map view, with $\mu' = 0.5$, $\sigma_1=200$ MPa, oriented -50° to the strike of the faults 49
- 2.12 Plate 3. Static changes in Coulomb failure stress and initial proximity to failure (τ/τ_{fail}) (a) on the strike-slip fault, and (b) on the dipping fault, with hypocenter distribution for the next 20 years of simulated seismicity. . 50

- 3.1 Model fault. (a) Model geometry, tectonic loading and boundary conditions. We consider the case of a vertical finite fault model consisting of a sealed tabular ductile body of width W embedded in an elastic country rock (half-space). The tectonic loading is performed via both a basal shear drag (30 mm yr^{-1} at 20 km depth) and a far field compression (3 mm yr^{-1}). We impose a constant hydraulic head condition at the top of the fault. (b) Structure of the model fault zone (adapted after Tanaka et al., 2001). Slip occurs on very narrow fault surfaces embedded in a zone of width W that increases with the total slip. This zone has a low permeability, roughly between 10^{-20} and 10^{-18} m^2 during interseismic periods and up to 10^{-15} m^2 coseismically. The (drained) damaged zone is not part of the model fault zone. A small leakage is allowed out of the fault core. 60
- 3.2 Degrees of freedom in the Mohr-space to consider when calculating the exact time step to the next failure of a cell in the model fault system. During interseismic periods, shear stress decreases on a cell due to shear creep and increases from both tectonic loading and stress transfer from other creeping cells, whereas the effective stress increases from normal stress increase and decreases due to pore pressure increase (from poroelastic effects and creep compaction). 62
- 3.3 Geometry and boundary conditions (map view) between the tabular sealed ductile fault zone of width W and the country rock. L is the effective width of the region which deforms elastically. The displacements imposed at the boundaries are d_1 and d_2 in the general case discussed in section 3.3.1. (a) case where no slip occurs in the fault zone; (b) case where a displacement d_f has occurred on the fault. 63
- 3.4 A 3-D case of ductile fault zone without in-plane flow: model results for a cell at 14 km depth for a 500 year simulation (constant fluid compressibility). From top to bottom: Stress state. The two solid lines show the time evolution of shear stress and pore pressure whereas the two dotted lines show the hydrostatic and the lithostatic pressure at 14 km depth. Porosity evolution. Creep slip. Seismic slip. Results show first a period of quiescence from $t=0$ to about 60 years. Shear stress increases due to tectonic loading, pore pressure increases due to compaction (from 9% to 8% porosity), and no slip has occurred yet. At the time of the first rupture where the average slip is about 1.5 m, porosity increases from 7.96 % to 8.91% by frictional dilatancy and pore pressure decreases from about 250 MPa to about 230 MPa, still above hydrostatic. The small drop in pore pressure after an event keeps the frictional strength at a low level, leading to a weak fault, with high pore pressure, short seismic cycles (about 8 years) and low shear stress. The sudden positive steps in shear stress show stress transfer from other cells. 69

- 3.5 Total displacement on the fault at $t=1020$ years. (a) Seismic slip: it ranges from 1 to 5.5 m, with the maximum values reached below 10 km depth. As in FM01, each time slip is evaluated on a cell, it is calculated to induce a drop of 25% of the current shear stress. It is therefore expected to get more slip at depth where the shear stress is the largest (e.g., tectonic loading). The total slip distribution corresponds to about 1500 events with magnitudes ranging from 3.9 to 6.5 and a slope of the frequency-magnitude relationship about 0.9. (b) Creep slip: the small scale of the heterogeneity of the distribution, as well as the overall increase with depth reflects more the variations in the shear stress distribution (Figure 3.6 (a)) than that of the width of the fault core. In this simulation, the intrinsic shear viscosity is 2.78×11 Pa yr and the creep slip is extremely small: maximum 5 cm (reached at depth lower than 12 km). This corresponds to a creep-seismic slip ratio of maximum 0.8 % 74
- 3.6 Stress and overpressure state on the fault at $t=1020$ years. (a) Shear stress distribution. The distribution shows small scale heterogeneities, as well as an overall increase with depth due to the tectonic loading, (b) Pore pressure to normal stress ratio (λ). The fault is strongly overpressured below 6 km depth and the pore pressure distribution is organized in small compartments. 75
- 3.7 Pore pressure re-equilibration after failure (and dilatancy) of the middle cell. After 3 months, pore pressure is almost uniform, above 240 MPa. This value is close to the 255 MPa calculated with equation (3.18). Reasonably homogeneous pore pressure equilibrium is achieved after about 6 months. . 77
- 4.1 Seismotectonic map of Southern California showing the major fault traces (red lines) and the seismicity between October 2000 and September 2001 (recorded by SCSN/TriNet). The yellow arrows show the boundary conditions for our model, the basal shear drag parallel to the Northern part of the San Andreas fault and the far-field compression perpendicular to it. The thick red lines show the two segment of the San Andreas fault included in our calculations. 85
- 4.2 Tectonic regimes calculated at 8.5 km depth for 10,000 years of basal shear drag and far field compression. The plate boundary lies in a pure strike-slip regime, while transpression is shown to develop south west of the Bend (e.g., transverse ranges, San Gabriel belt). The y axis shows the distance to the Northern segment of the San Andreas Fault (N. SAF). 86
- 4.3 Geometry of the model fault system and boundary conditions and Coulomb failure stress (CFS) calculated at 8.5 km depth due to 10,000 yr of tectonic loading. The two model faults, representing two segments of the San Andreas Fault, are shown to be the first faults to accumulate enough stresses to reach the failure criterion. The white color corresponds to $CFS = 0$. . . 86

- 4.4 Time evolution of the average properties on the Northern strike-slip fault; from top to bottom, shear stress, effective stress, the degree of overpressure λ and the amount of creep slip. The first part ($t = 0$ to $t \sim 2500$ yr) is the stress build-up phase. Seismicity then initiates, and the first large event ($t \sim 3000$ yr) induce large drops in pore pressure. Creep and ductile compaction initiate at $t = 3750$ yr. The pore pressure increase rate is much larger than the shear increase rate. Although the first large events allow the pore pressure to drop back to hydrostatic levels, ductile compaction leads to a progressive weakening of the fault. 88
- 4.5 Time evolution of the average properties on the Southern strike-slip fault. Same as Figure 4.4. Because of the 20° angle between the fault strike and plate motion, the normal stress build-up rate is larger than in the previous case, initially leading to a stronger fault. As ductile compaction initiates, the larger effective stress leads to a larger compaction rate and faster overpressurization of the fault. The fault can not sustain high shear stresses anymore and evolves to a weaker fault. The average amount of creep is $2/3$ the creep slip on the northern fault. 89
- 4.6 Seismicity timelines and frequency-magnitude statistics. (a) for the northern strike slip fault; (b) for the southern strike-slip fault. The first large events occur after $t = 2500$ yr. The arrows show the onset of shear creep and ductile compaction at $t = 3750$ yr. The density of the seismicity reflects the strength of the faults shown in figures 4.4 and 4.5. Thus, it doesn't increase immediately significantly on the first fault since it recovers a high strength after the first large earthquakes occurring after $t = 3750$ yr. The density of medium size events ($4.5 < M_w < 6$) increases dramatically on the second fault. Both faults exhibit Gutenberg-Richter laws with a b-value of 0.9 (shown by the straight line). 90
- 4.7 Surface deformation (arrows) and spatial variation of principal stresses (R) at $t = 4050$ yr. The maximum surface deformation rate along x is 32 mm yr^{-1} far from the plate boundary and along y 7 mm yr^{-1} . R , calculated at 8.5 km depth, shows values between 0.05 and 0.75 indicating a large spatial heterogeneity of the stress tensor (see text for details). 92
- 4.8 Maximum shear stress and orientation of σ_1 (black arrows). Shear stress is maximum along the plate boundary in a 20 km wide zone ($\sim 70 \text{ MPa}$) and is largely perturbed on the Southern fault. Although the level of shear stress is reduced on both sides of the fault, stress transfer from previous earthquakes locally increased the maximum shear stress near the fault up to 200 MPa . In the same manner, σ_1 is consistently oriented $\sim 45^\circ$ to the Northern fault, and $\sim 55^\circ$ to the Southern fault in a 20 km wide band. However, it locally rotates to be almost perpendicular to the fault strike near the southern fault. 93
- 4.9 Topographic view of the Big Bend (source: JPL) 93

-
- 4.10 Optimal orientation for failure at $t = 4050$ yr calculated at 8.5 km depth. The colors show the dip angle of the optimally oriented planes and the lines show the strike of some noticeable features. The subvertical strike-slip fault shown east of the Bend represents an analog to the Garlock fault, although this fault orientation prevails in the whole area within the red oval. The thrust faults that would develop in the model west of the Bend are analog to the transverse ranges and the San Gabriel thrust belt. 94
- 4.11 Degree of overpressure λ at $t = 4050$ yr (a) on the northern fault, (b) on the southern fault. The second fault is more overpressured than the first one. In both cases, large compartments of low pore pressure (hydrostatic levels) are generated by ruptures that reached the top layer constant head boundary condition. 95

List of tables

1.1	Geometry and dimensions of the model fault for the inversion of slip for the Izmit earthquake (Turkey, 1999). Three sub-vertical rectangular fault segments are used in the modeling (Delouis et al., 2000).	15
2.1	Model Parameters and Initial Conditions. ^a After <i>Sleep</i> [1995]	29
2.2	Coseismic stress triggering between the two faults. M1 and M2 refer to the moment magnitude (M_w) of strike-slip fault and dipping fault events, respectively, and are calculated from the scalar seismic moment M_0 via equation (2.6). The triggering event is always the larger of the two, except at $t=4585.5$ years, see row in parentheses.	45
3.1	Model Parameters and Initial Conditions. ^a After <i>Sleep</i> and <i>Blanpied</i> [1994], ^b After <i>Sleep</i> [1995]	67

Seite Leer /
Blank leaf

Abstract-Résumé

Abstract

A 3-dimensional fault interaction model was developed that incorporates the dominant aspects of the earthquake process. This includes large-scale plate-motion loading, small-scale hydraulics and fluid flow in fault zones, and elastic stress transfer from slip on one fault to all other faults in the system. The basis for modeling brittle faulting is the analytical solution for the displacement field resulting from slip on a dislocation plane of any orientation embedded in a 3-dimensional elastic half-space. Fault hydraulics are approximated by large co-seismic changes in fault zone permeability. A study of stress transfer investigated the changes in Coulomb failure stress (ΔCFS) on optimally oriented vertical faults following the Izmit (M_w 7.4, 1999, Turkey) earthquake. This study demonstrated the significant limitations to the ΔCFS approach, particularly with respect to the regional stress tensor and of pore pressure state in the medium. The ΔCFS approach is incorporated into a forward model that integrates large-scale tectonic loading (stress changes and pore pressure changes through poroelasticity), small-scale co-seismic hydraulic property evolution, and interseismic compaction processes. This allows monitoring the time evolution of the stress and pore pressure state on a fault system, model seismicity, and the consequent coseismic elastic surface deformation. The regional stress in the model area can be calculated (at any depth at any location) as a result of tectonic loading and slip along faults.

A 3-dimensional forward model of interacting faults (Fitzenz and Miller, 2001) generalizes the model of Miller et al. (1996,1999) to a fully three-dimensional model where faults of any strike and geometry interact through an elastic matrix. Simulation results are presented of the long-term evolution (≈ 9300 years) of a generic case of a blind, dipping fault and a subvertical strike-slip fault in a transpressional tectonic environment. These results show the development of pore pressure compartments, seismicity statistics that conform with theoretical and observed results, and realistic rupture propagation patterns that include changes in the rake angle. The important influence of fault zone fluids on the triggering of earthquakes from one fault to the other, via poroelastic effects is also investigated.

Constraints on fault zone hydraulics were investigated, and a fault compaction model is developed and implemented into the forward model. The modeled fault zone is derived from field and borehole observations of active crustal faults. It is shown that compaction of a ductile fault zone is a viable (and likely) mechanism for overpressuring faults, particularly if in-plane fault hydraulics are considered. We show and discuss how the large pore pressure drops following a seismic event shown in a 1-dimensional model (Sleep and Blanpied, 1992) do not occur when co- and post-seismic hydraulics of the 2nd and 3rd

dimension are considered.

The model developments discussed in this thesis are combined into a regional model of a transpressional San Andreas Fault (SAF) in Central California. The main aspects are plate motion loading, shear creep and ductile compaction, in-plane interseismic fluid diffusion, and out of plane leakage. Maps of tectonic regimes and Coulomb failure stress provide constraints on the boundary conditions (e.g., tectonic loading). We find that overpressured compartments on model faults through ductile compaction are a necessary consequence of the tectonic loading, specifically where high normal stress acts on long straight fault segments. It is shown that a transpressive tectonic regime develops South-West of the model Big Bend as a result of the loading boundary conditions, consistent with observations. Stress transfer from fault seismicity is shown to induce significant perturbations in the local stress tensor. Maps of maximum shear stress emphasize the need for future model developments to dynamically generate new fault planes that respond to the evolving stress field. The results of this study form the foundation for developing time-forward mechanistic assessment of seismic hazard for large-scale potentially destructive fault systems.

Résumé

Un modèle tridimensionnel incorporant les aspects dominants de la mécanique des tremblements de terre a été développé. Il prend en compte le chargement tectonique à grande échelle, les propriétés hydrauliques et les fluides à petite échelle dans les zones de faille, et les transferts de contraintes élastiques sur toutes les failles du système dus au glissement sur l'une des failles. La modélisation de la rupture fragile s'appuie sur les solutions analytiques décrivant le champ de déplacement résultant du glissement sur un plan de dislocation de géométrie quelconque dans un demi-espace élastique. L'hydraulique des failles est décrite sous la forme de grandes variations de perméabilité cosismiques. Une première étude s'est intéressée aux effets du séisme d'Izmit (M_w 7.4, 1999, Turquie) sur la proximité du seuil de rupture autour de la faille principale. Les variations de contrainte de rupture (Coulomb failure stress, *CFS*) ont été calculées sur des plans verticaux orientés optimalement pour la rupture. Cette étude a mis en évidence les limites de cette méthode, liées en particulier à la nécessité d'avoir une connaissance détaillée du tenseur de contraintes en trois dimensions et de la pression fluide dans le milieu. Cette approche semi-directe est la base des modèles directs d'interaction entre failles développés dans cette thèse. Les autres processus pris en compte sont le chargement tectonique, les variations cosismiques des propriétés hydrauliques de la zone de faille, et la compaction intersismique. Les contraintes, la pression fluide, la sismicité sont enregistrées, et le tenseur de contrainte régional peut être calculé en réponse à la tectonique et au glissement sur les failles du modèle.

Un modèle 3-D direct d'interaction entre failles (Fitzenz and Miller, 2001) généralise le modèle de Miller et al. (1996,1999). Les résultats des simulations montrent l'évolution dans le temps (≈ 9300 ans) d'un système comprenant une faille enfouie inclinée et une faille cisailante subverticale dans un environnement transpressif. Des compartiments de pression fluide se développent sur les failles, les statistiques de la sismicité sont en accord avec les observations et la théorie, et la propagation des ruptures est réaliste. L'influence des fluides dans le déclenchement de séismes d'une faille à l'autre par effet poroélastique est également étudiée.

Nous avons étudié comment contraindre l'hydraulique des zones de faille, et nous avons développé un modèle de compaction que nous avons intégré dans le modèle direct. La représentation des zones de faille est basée sur des observations de failles actives (terrain et forage). La compaction de zones de faille ductiles se révèle être un mécanisme viable (et vraisemblable) de surpressurisation des failles, en particulier quand les circulations de fluide dans le plan des failles sont inclus. Nous montrons et discutons comment les chutes de pression qui se produisent après une rupture dans le modèle 1-D de Sleep et Blanpied (1992) ne se produisent pas dans le modèle 3-D.

Les développements du modèle discutés dans cette thèse sont combinés dans un modèle régional, transpressif, de la faille San Andreas en Californie centrale. Les aspects principaux en sont les mouvements de plaques, le glissement asismique (shear creep), la compaction visqueuse, la diffusion intersismique dans le plan de faille, et la fuite de fluide hors de la zone de faille. Des cartes des régimes tectoniques et de seuils de rupture permettent de contraindre les conditions aux limites (chargement tectonique). Des compartiments surpressurisés se développent en réponse à la compaction, en particulier quand le chargement tectonique induit des grandes contraintes normales. Un régime transpressif

se développe dans le modèle au sud-ouest de la courbure dans la limite de plaque, en accord avec les observations. Les transferts de contrainte dus à l'activité sismique des failles modélisées provoquent des perturbations significatives dans le tenseur de contrainte local. Des cartes de contrainte cisailante maximale mettent en relief la nécessité d'intégrer la génération dynamique de nouvelles failles en réponse aux variations du champ de contrainte dans les prochains modèles. Les résultats de cette étude forment les fondations pour une évaluation du risque sismique basée sur la mécanique des tremblements de terre, pour les systèmes de failles potentiellement destructeurs.

Introduction and summary

Objective: model earthquake generation on interacting faults

A series of recent, large destructive earthquakes in or near large cities demonstrates the need for understanding the earthquake process and to mechanistically assess seismic hazard. Some of these events (e.g., the $M_w = 6.9$ Kobe earthquake, Japan, 1995; the $M_w = 7.4$ Izmit quake) occurred on strike-slip faults, while others (e.g., the $M_w = 7.6$ Chichi earthquake, Taiwan, 1999) occurred on buried thrust faults or on faults with significant dip-component, suggesting the 3-dimensional character of the earthquake process. Other large earthquakes are expected near urban areas in the future, including the “Big One” in California.

Since earthquakes occur deep within the brittle crust, they are not directly observable and signals detected at the surface must be analysed to describe the behavior of fault systems. These signals include seismicity records, surface strain fields, topography evolution, water level changes in wells, and subsurface geophysical surveys conducted in seismically active areas to image fault zones (e.g., magnetotelluric and seismic imaging). Data measured in boreholes drilled in active fault zones also provide valuable information on the geology of fault zones and on the physical processes acting at depth. These data show the major role of tectonic loading, the significant influence of fluids in fault zones, and fault interaction. Many individual studies of these aspects have lead to a general understanding of what controls brittle failure of the crust, but few models exist that try to synergize these components and these observations into an interacting system. Building and analysing such an integrative physics-based model is the goal of this thesis.

First basis for this work includes conceptual models describing the earthquake cycle, empirical laws of rock properties from laboratory experiments (e.g., friction evolution, effects of fluids on faulting, frictional dilatancy), knowledge on fault zone structure (e.g., porosity, permeability, deformation type) of active or exhumed faults, and measured plate velocities. A fluid-controlled fault model (Miller et al., 1999, 2002) captured some important features of the mechanics of faulting, including earthquake statistics and scaling relationships, complexity of the stress state, spontaneous generation of asperities, and stress drops in accordance with observations. These models were built for vertical strike-slip faults, and coupled the mechanical effects of fluid within a cellular fault zone with shear stress accumulation from constant plate motion applied at the downward continuation of the fault. This project is aimed at generalizing the model to 3 dimensions, and

improves on some of its physical bases. With this continued development, further understanding and implications of the earthquake model are explored.

Contents of the thesis

This work consists of five main parts. The main concepts of elasticity and rock mechanics that form the basis for the numerical models are described in Chapter 1. These concepts are then applied to a stress triggering model of the Izmit (1999, Turkey) earthquake. Limitations of the stress triggering models are discussed, and these issues are addressed in Chapter 2, which describes the 3-dimensional forward fault interaction model in detail. The model includes the mechanical effects of fluids, tectonic loading and stress transfer. A variety of results are described and discussed in terms of the earthquake process. Chapter 3 focuses on the hydraulics of fault zones, presenting a detailed analysis of the role of shear creep and ductile fault zone compaction as a mechanism to generate overpressures within faults. Chapter 4 combines the main features of the three previous models to investigate a regional model, namely the Big Bend in the San Andreas Fault in Central California. Conclusions and future perspectives are discussed in Chapter 5.

Chapter 1 has three main parts. The first is the theoretical basis for the modeling developed during this thesis. These include infinitesimal strain theory and the derivation of the analytical solutions giving the internal displacement field due to 1) a point source force in an infinite elastic medium, and 2) a finite dislocation in an elastic half-space. A short summary of rock mechanics concepts (i.e., stress-strain relationships, effective stress, Coulomb failure stress, and poroelasticity, etc.) are also discussed. The derivation of the optimal orientation for failure is given for a given principal stress tensor. Second, we describe and use the stress triggering approach as a first study of fault interaction on the example of the Izmit earthquake. Third, we show the limitations of semi-forward models and the motivation for a forward fluid-controlled model of fault interaction including crustal fluids, tectonics and stress transfer.

Chapter 2 presents simulation results of a 3-dimensional forward model of interacting faults (this Chapter was published in *J. Geophys. Res.* and is reproduced here). The model, including the physics of pore pressure changes and fluid flow within a seismic fault zone, generalizes that of Miller et al. (1996,1999) to a fully three-dimensional model where faults of any strike and geometry interact through an elastic matrix using the general solutions of Okada (1992). The model includes large-scale plate motion loading and increasing pore pressures from a mechanism for pore space reduction, undrained poroelastic effects, large coseismic hydraulic property changes, and porosity creation through dilatant slip. Results are presented of the long-term evolution (≈ 9300 years) of a generic case of a blind, dipping fault and a subvertical strike-slip fault in a transpressional tectonic environment. The model is discussed in terms of stress state evolution along both faults, development of pore pressure compartments, seismicity time lines and statistics, quasi-static rupture propagation including rake angle changes, local and regional stress buildup and rotations, static and dynamic fault interactions, and ΔCFS (changes in Coulomb Failure Stress) within the fault system. Shortcomings of the model are discussed, that include constraints

on fault zone hydraulics, developed further in Chapter 3, and on tectonic loading, investigated in Chapter 4.

Chapter 3 investigates fault zone hydraulics and a fault compaction model is developed and implemented into the forward model presented in Chapter 2. The modeled fault zone is derived from field and borehole observations of active crustal faults. It is shown that compaction of a ductile fault zone is a viable (and likely) mechanism for overpressuring faults, particularly if in-plane fault hydraulics are considered. We show that large pore pressure drops to hydro- or sub-hydrostatic levels after a seismic event shown in a 1-dimensional model (Sleep and Blanpied, 1992) do not occur when extended to 3-D.

Chapter 4 presents further model developments and a first step towards constructing regional models. Starting from the simple forward model of Chapter 2, we implement shear creep and ductile compaction, as well as in-plane interseismic fluid diffusion and out of plane leakage. In a second part, simulation results are shown for a regional model of a transpressional San Andreas Fault (SAF) in Central California. Tectonic loading is decomposed into basal shear drag parallel to the plate boundary and East-West compression approximated by a vertical dislocation surface applied at the far-field boundary. Taking into account the main result of Chapter 3, i.e., the rapid evolution toward an overpressured weak fault when ductile compaction acts on a fault zone, we choose to load the fault system to a system of strong faults before creep and ductile compaction are introduced on the fault. Model results include optimal tectonic regimes, stress orientations and Coulomb failure stress maps at depth. We also show the stress state and the slip on both faults, as well as seismicity timelines and frequency-magnitude statistics. We conclude by presenting the set of models developed during this PhD work as a framework for building regional models.

The conclusions and perspectives are developed in Chapter 5.

Seite Leer /
Blank leaf

Chapter 1

**Elasticity and stress transfer:
Theory and application to the Izmit
(Turkey 1999) earthquake**

1.1 Elasticity and dislocation theory

Earthquake ruptures correspond to slip on one or several planar surfaces. There are three basic ways of studying the rupture process of a spreading source (e.g., earthquake propagation): the dynamic simulation, the quasi-static simulation, and the kinematic description. The dynamic and quasi-static approaches consist of modeling rupture propagation from initial conditions and physical laws, with the difference that the quasi-static approach ignores inertial effects (wave propagation). The kinematic approach describes the rupture and its evolution using a limited number of parameters such as the fault geometry and the history of the rupture on each discretization point of the fault. The kinematic description does not rely on physical processes, instead, it is used to evaluate the size of the rupture area, the distribution of slip on the fault, the local duration of slip to constrain the dynamic approach.

This thesis was developed using a quasi-static approach, supported by the mostly elastic response of the crust to an earthquake. Except in the immediate vicinity of the seismic source, most of the ground motion is elastic; so the ground returns to its initial position after the transient motions have subsided. Vibration of this type involve small elastic deformations, or strains, in response to internal forces in the rock, or stresses (e.g., relative length changes of $\sim 10^{-6}$ over short periods of time, < 3600 s). The theory of elasticity provides the mathematical relationships between the stresses and strains in the medium for small strains. A major property of elastic media is the superposition theorem. The effect of two applied perturbations is the sum of the effects of each perturbation. As a direct consequence of this theorem, the stress build-up over a period of time due to plate motion can be calculated as the effect of one displacement. The magnitude of this displacement is the integral of plate velocity over this time period. For the same reason, the total deformation field in a fault system is the sum of the regional deformation field and the perturbations due to local seismicity.

The study of macroscopic phenomena in solids is made in the framework of continuum mechanics, in which matter is viewed as being continuously distributed in space. Mathematical functions for displacement, strain, or stress fields, with continuous spatial derivatives can then be defined. The relationship between applied forces and internal deformation in infinitesimal strain theory is largely empirically based and given by a constitutive law called Hooke's law. The deformation is a function of material properties (elastic moduli) of the body such as density, rigidity (resistance to shear), and incompressibility (resistance to change in volume). In this work, we employ a Lagrangian description of motions within the solid medium, in which the motion of a particular particle is followed as a function of time and space.

In the elastic quasi-static approach, faults are idealized by a displacement discontinuity (i.e., dislocation, i.e., relative motion of one side of the fault with respect to the other side) across a surface (i.e., dislocation plane). Seismic slip on a fault plane is modeled as a slip vector acting on a dislocation plane (Figure 1.1). Elastic dislocation theory proved a good approximation for brittle crustal faulting as evidenced by the successes in

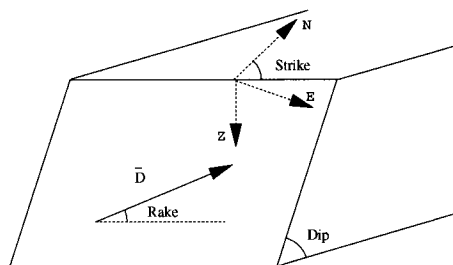


Figure 1.1: Standard definition of fault-plane and slip-vector orientation parameters.

modeling coseismic surface deformation from satellite interferometry (Massonnet et al., 1993, and see Figure 1.2). In this section, we describe internal deformations within the solid due to a point source in an infinite elastic medium and then to a finite dislocation in an elastic half-space. This is followed by a discussion of the Coulomb failure criterion, and application of stress triggering on the example of the $M_w = 7.4$ Izmit earthquake (August 1999, Turkey).

1.1.1 Elastostatics and dislocation theory in an infinite medium

The theoretical basis for the displacement (and strain) calculation in the numerical models developed during this work is the analytical solution of a rectangular dislocation in an elastic half-space. The basics of the theory is summarized here for completeness. We decompose the problem into three main steps. First we calculate the internal displacement field due to a single force in a homogeneous space. Then we adapt this formalism to the half-space. Finally, we present how to calculate the displacement due to a point-source dislocation and to a finite dislocation.

Consider a single point source force \vec{f} applied at a point of coordinates $\vec{\xi} = (\xi_1, \xi_2, \xi_3)$ in an elastic isotropic homogeneous infinite space. Static equilibrium is given by:

$$(\lambda + G)\vec{\nabla}(\vec{\nabla}\cdot\vec{u}) + G\nabla^2\vec{u} + \vec{f} = \vec{0} \quad (1.1)$$

where $\vec{\nabla}$ is the gradient vector, G is the rigidity (i.e., shear modulus), $\lambda = \lambda_{\text{Lamé}}$ is the second Lamé coefficient and $\vec{u} = \vec{u}(\vec{x})$ is the internal displacement field at a point \vec{x} due to the single force \vec{f} . Assuming that only f_1 is non-zero, equation (1.1) is equivalent to:

$$\begin{cases} (\lambda + G)\frac{\partial}{\partial x_1}(\vec{\nabla}\cdot\vec{u}) + G\nabla^2 u_1 + f_1\delta(\vec{x} - \vec{\xi}) = 0 & (a) \\ (\lambda + G)\frac{\partial}{\partial x_2}(\vec{\nabla}\cdot\vec{u}) + G\nabla^2 u_2 = 0 & (b) \\ (\lambda + G)\frac{\partial}{\partial x_3}(\vec{\nabla}\cdot\vec{u}) + G\nabla^2 u_3 = 0 & (c) \end{cases} \quad (1.2)$$

From Helmholtz's theorem, any vector field \vec{u} can be represented in terms of a vector potential $\vec{\psi}$ and a scalar potential ϕ by

$$\vec{u} = \vec{\nabla}\phi + \vec{\nabla} \times \vec{\psi} \quad (1.3)$$

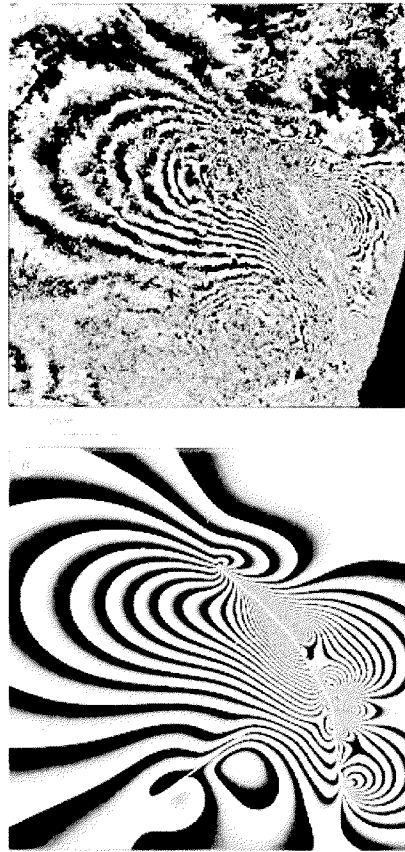


Figure 1.2: Interferogram showing deformation fringes for the Landers earthquake. One fringe corresponds to a displacement in the direction ground/satellite equals to one half of the wavelength of the radar. The patterns formed by interferogram fringes (top) and attributed to coseismic deformation were successfully modeled using planar dislocation sources (bottom) (from Massonnet et al., 1993).

where \times is the vector product (cross product), with the property that $\vec{\nabla} \times \vec{\psi}$ is divergence free (e.g., $\nabla \cdot (\vec{\nabla} \times \vec{\psi}) = 0$) and $\vec{\nabla} \phi$ is curl free (e.g., $\vec{\nabla} \times (\vec{\nabla} \phi) = 0$). Equation (1.2) can be rewritten in terms of these potentials as:

$$\begin{cases} (\lambda + 2G)\nabla^2 \frac{\partial \phi}{\partial x_1} + G\nabla^2 \left(\frac{\partial \psi_3}{\partial x_2} - \frac{\partial \psi_2}{\partial x_3} \right) + f_1 \delta(\vec{r}) = 0 \\ (\lambda + 2G)\nabla^2 \frac{\partial \phi}{\partial x_2} + G\nabla^2 \left(\frac{\partial \psi_1}{\partial x_3} - \frac{\partial \psi_3}{\partial x_1} \right) = 0 \\ (\lambda + 2G)\nabla^2 \frac{\partial \phi}{\partial x_3} + G\nabla^2 \left(\frac{\partial \psi_2}{\partial x_1} - \frac{\partial \psi_1}{\partial x_2} \right) = 0 \end{cases} \quad (1.4)$$

where $\vec{r} = \vec{x} - \vec{\xi}$. It is known that $V = 1/|\vec{r}|$ is a solution of $\nabla^2 V = -4\pi\delta(\vec{r})$, and $\nabla^2(\vec{r}) = 2/|\vec{r}|^3$. Hence, $\nabla^2 \nabla^2(\vec{r}) = -8\pi\delta(\vec{r})$. We want to get $\nabla^2 \nabla^2(\vec{r})$ to solve equation (1.4). We choose $\phi = C_a \frac{\partial r}{\partial x_1}$, $\psi_2 = C_b \frac{\partial r}{\partial x_3}$, and $\psi_3 = C_c \frac{\partial r}{\partial x_2}$, where C_a , C_b , and C_c are constants. Equation (1.2a) becomes:

$$(\lambda + 2G)C_a \nabla^2 \frac{\partial^2 r}{\partial x_1^2} + G\nabla^2 \left(C_c \frac{\partial^2 r}{\partial x_2^2} - C_b \frac{\partial^2 r}{\partial x_3^2} \right) + f_1 \delta(\vec{r}) = 0. \quad (1.5)$$

Assuming further that $(\lambda + G)C_a = GC_c = -GC_b$, and solving

$$\begin{cases} (\lambda + 2G)C_a \nabla^2 \left(\frac{\partial^2 r}{\partial x_1^2} + \frac{\partial^2 r}{\partial x_2^2} + \frac{\partial^2 r}{\partial x_3^2} \right) + f_1 \delta(\vec{r}) = 0 \\ \nabla^2 \nabla^2(\vec{r}) = -8\pi\delta(\vec{r}) \end{cases} \quad (1.6)$$

for C_a yields $(\lambda + G)C_a = \frac{f_1}{8\pi}$, and we have determined ϕ , ψ_2 , and ψ_3 , which are solutions of equation (1.2a):

$$\begin{cases} \phi = \frac{f_1}{8\pi(\lambda+2G)} \frac{\partial r}{\partial x_1} \\ \psi_2 = -\frac{f_1}{8\pi G} \frac{\partial r}{\partial x_3} \\ \psi_3 = -\frac{f_1}{8\pi G} \frac{\partial r}{\partial x_2} \end{cases} \quad (1.7)$$

The two other equations of the system are verified for $\psi_1 = 0$. The internal displacement field at a point \vec{x} in the infinite space due to the single force \vec{f} is given by substituting equation (1.7) in equation (1.3):

$$u_i^1 = \frac{f_1}{8\pi G} \left(\frac{2-\alpha}{R} \delta_{i1} + \alpha \frac{R_i R_1}{R^3} \right), \quad (1.8)$$

where the index 1 refers to the non-zero component of the force, $\alpha = \frac{\lambda+G}{\lambda+2G}$, and R is the distance between the source and the observation point (i.e., $R^2 = (x_1 - \xi_1)^2 + (x_2 - \xi_2)^2 + (x_3 - \xi_3)^2$).

In the general case of a force f_j , the displacement field is:

$$u_i^j = \frac{f_j}{8\pi G} \left(\frac{2-\alpha}{R} \delta_{ij} + \alpha \frac{R_i R_j}{R^3} \right), \quad (1.9)$$

u_i^j is called the Somigliana tensor (Steketee, 1958). For a Poisson solid, e.g., $\lambda \sim G$, $\alpha \sim 2/3$.

1.1.2 Elastic half-space

Analytical solutions giving displacements and displacement derivatives in an elastic half-space were derived (Okada, 1985, 1992) for point sources. The introduction of a free surface changes the boundary conditions of the elastostatics. The displacement can be written as the superposition of four terms:

$$u_i^j(x_1, x_2, x_3) = u_{iA}^j(x_1, x_2, -x_3) - u_{iA}^j(x_1, x_2, x_3) + u_{iB}^j(x_1, x_2, x_3) + x_3 u_{iC}^j(x_1, x_2, x_3) \quad (1.10)$$

The first term $u_{iA}^j(x_1, x_2, -x_3)$ is the Somigliana tensor (solution for the infinite medium, equation (1.9)). The second term corresponds to a contribution from an image source of the given point force placed at $(\xi_1, \xi_2, -\xi_3)$ in the infinite medium, although the polarity of the image source is switched from one component to another to eliminate the surface displacements when combined with the first term. The third term accounts for the surface displacement field due to a point force in a half-space (Okada, 1985). The fourth term is a depth-dependency.

$$\begin{cases} u_{iA}^j = \frac{f}{8\pi G} \left(\frac{2-\alpha}{R} \delta_{ij} + \alpha \frac{R_i R_j}{R^3} \right), \\ u_{iB}^j = \frac{f}{4\pi G} \left(\frac{\delta_{ij}}{R} + \frac{R_i R_j}{R^3} + \frac{1-\alpha}{\alpha} \left[\frac{\delta_{ij}}{R+R_3} + \frac{R_i \delta_{j3} - R_j \delta_{i3} (1-\delta_{j3})}{R(R+R_3)} - \frac{R_i R_j}{R(R+R_3)^2} (1-\delta_{i3})(1-\delta_{j3}) \right] \right), \\ u_{iC}^j = \frac{f}{4\pi G} (1-2\delta_{i3}) \left[(2-\alpha) \frac{R_i \delta_{j3} - R_j \delta_{i3}}{R^3} + \alpha \xi_3 \left[\frac{\delta_{ij}}{R^3} - 3 \frac{R_i R_j}{R^5} \right] \right] \end{cases} \quad (1.11)$$

where subscript *A* refers to infinite medium terms, subscript *B* refers to a surface deformation related term, and subscript *C* is a depth multiplied term.

From Steketee (1958), the displacement field due to a point-source dislocation $\Delta u_j(\xi_1, \xi_2, \xi_3)$ across a surface Σ in an isotropic medium is given by:

$$u_i = \frac{1}{f} \int \int_{\Sigma} \Delta u_j \left[\lambda \delta_{jk} \frac{\partial u_i^n}{\partial \xi_n} + G \left(\frac{\partial u_i^j}{\partial \xi_k} + \frac{\partial u_i^k}{\partial \xi_j} \right) \right] \nu_k d\Sigma, \quad (1.12)$$

where summation convention applies, and ν_k is the direction cosine of the normal to the surface element $d\Sigma$, i.e., $(0, -\sin\delta, \cos\delta)$ with the conventions of Figure 1.3. The derivatives $\frac{\partial u_i^j}{\partial \xi_k}$ (from which strains are determined) are obtained by differentiating equation(1.10). Okada (1992, equations 4 and 5) uses this equation to calculate the internal displacements due to a double couple (moment M_o) corresponding to strike-slip and dip-slip point sources.

For a rectangular dislocation, he integrates the previous equations over the area of the fault.

In the following, we use the full solutions derived by Okada (1992) for rectangular dislocations in an elastic Poisson solid ($\lambda = G$) half-space whenever displacement or deformation fields are calculated (except if specified otherwise).

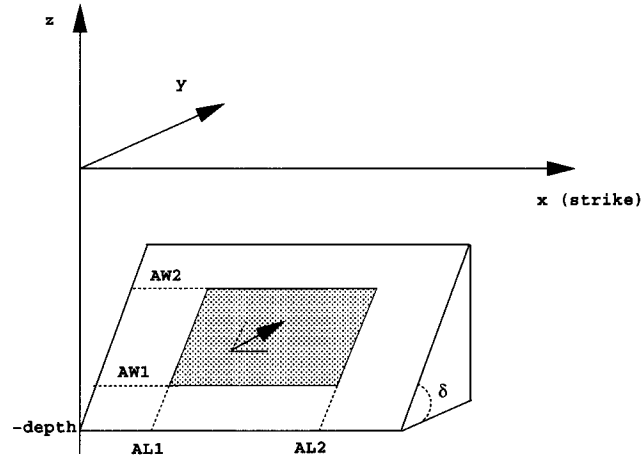


Figure 1.3: Representation of rectangular dislocation planes as used by Okada (1985, 1992). The surface $z=0$ is the free surface. For each dislocation rectangle (shaded area) of any dip angle δ , a unique constant slip vector of any rake angle can be defined (slip normal to the plane, e.g., opening, is also possible).

1.2 Rock mechanics and stress transfer

1.2.1 Introduction to rock mechanics

Once the displacement field is computed (Tables 6 to 9 in Okada, 1992), the strain ϵ_{ij} and stress σ_{ij} fields can be obtained at any given point in the half-space from:

$$\begin{cases} \epsilon_{ij} = \frac{1}{2} \left(\frac{\partial u_i}{\partial x_j} + \frac{\partial u_j}{\partial x_i} \right) \\ \sigma_{ij} = \lambda \epsilon_{kk} \delta_{ij} - 2G \epsilon_{ij} \end{cases}, \text{ Hooke's law,} \quad (1.13)$$

where i and j range from 1 to 3, u_i is the i th component of the displacement vector \vec{u} , x_j is x , y or z , and λ is the second Lamé constant and G is the rigidity modulus.

The mechanical behavior in rocks subjected to changes in either confining pressure or pore fluid pressure has commonly been cast in terms of the effective stress relationship (Terzaghi, 1923; Hubbert and Rubey, 1959), where the effective stress σ_{eff} is given by:

$$\sigma_{eff} = \sigma_n - P_f \quad (1.14)$$

where σ_n is the normal stress acting on a frictional surface, and P_f is the pore pressure. Although this relationship appears to be valid in many porous permeable rocks, a more general expression for the static case is: $\sigma_{eff} = \sigma_n - \alpha P_f$ (Nur and Byerlee, 1971), where α is found empirically and can range from 0 to 1.0 for fractured and intact rocks. Values of α less than 1 obtained for intact crystalline rocks have been ascribed to microfracture dilatancy in which the true internal pore pressures differ from the externally measured pore pressures. For experiments conducted on single fractures, Walsh (1981) showed that the value of α was 0.5-0.7. Morrow et al. (1994) showed that α is 1.0 for friction experiments

on montmorillonite/illite gouges in drained conditions whereas α is much less than 1.0 in undrained friction experiments with clay or sheet silicate gouges (Morrow et al., 1984). Evans et al. (1997) infer that α is higher for rocks with higher fracture density and larger degree of fracture interconnectivity (closer to a porous permeable rock that can transmit fluids and fluid pressures effectively). Although these deviations from equation (1.14) might be large depending on the geology and the processes of the fault zones, their study is beyond the scope of the present thesis, $\alpha = 1$ is assumed throughout.

Figure 1.4 shows the four main ways to bring a sample to failure in a classical bi-axial laboratory test. When a rock sample is loaded with a vertical maximum stress σ_1 and horizontal minimum stress σ_3 , a slip plane develops at an angle β to σ_3 . The shear (τ) and normal (σ_n) stresses can be defined on this plane using the Cauchy stress tensor or, more simply, the Mohr-circle representation. If the fault plane contains fluids at a pressure P_f , the effective stress σ_{eff} is defined as $\sigma_n - P_f$. The three numbered plots show four ways to reach the Coulomb failure criterion represented by the bold line of slope $\mu = \tan(\phi)$, where ϕ is the internal friction angle and μ is the friction coefficient:

$$|\tau| = c + \mu(\sigma - P_f) \quad (1.15)$$

The rock can be brought to failure by 1) increasing the maximum compressive stress σ_1 , 2) decreasing the minimum stress, or 3) increasing pore pressure. An alternative would be to decrease the friction coefficient μ , but this coefficient has been shown in general to be rock-type independent (Byerlee, 1978). In an isotropic homogeneous poroelastic model, the pore pressure changes are proportional to the mean stress. In that case, the failure criterion can be rewritten:

$$|\tau| = c + \mu'\sigma, \quad (1.16)$$

where $\mu' = (1 - B)\mu$ is the apparent friction coefficient and B is Skempton's coefficient.

1.2.2 Optimal orientation for failure

Calculation of the optimal orientation for failure for a given stress state is expressed with the principal components $\sigma_1 > \sigma_2 > \sigma_3$.

The normal and shear stresses acting on a plane with unit normal \vec{n} are $\sigma = (\sigma_{ij}n_j)\cdot\vec{n}$ and $\tau = \sigma_{ij}n_j - \sigma\vec{n}$, yielding

$$\begin{cases} \sigma_1 n_1^2 + \sigma_2 n_2^2 + \sigma_3 n_3^2 = \sigma \\ \sigma_1^2 n_1^2 + \sigma_2^2 n_2^2 + \sigma_3^2 n_3^2 = \sigma^2 + \tau^2 \\ n_1^2 + n_2^2 + n_3^2 = 1 \end{cases} \quad (1.17)$$

We solve for n_1 , n_2 and n_3 to determine the plane orientation for failure. The determinant (Vandermonde) of the system is $Det = (\sigma_1 - \sigma_2)(\sigma_2 - \sigma_3)(\sigma_3 - \sigma_1)$. If the three principal stresses are distinct, then the determinant is non-zero and the equations $n_i = constant$ define three families of circles in the Mohr diagram (Figure 1.4). The circle $n_2 = 0$ defines the locus of maximum shear stress. This circle goes through $(\sigma_3, 0)$ and $(\sigma_1, 0)$. Since the working coordinate system is the one of the principal stresses, $n_2 = 0$ means that the normal \vec{n} to the plane belongs to the plane (σ_1, σ_3) . Let ψ be the angle between \vec{n} and

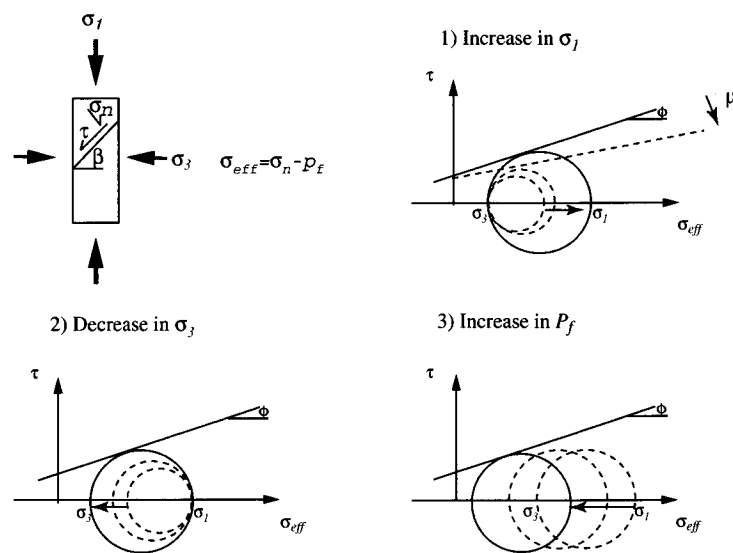


Figure 1.4: A typical bi-axial laboratory experiment. When a rock sample is stressed (vertical maximum stress σ_1 , horizontal minimum stress σ_3), then a rupture plane develops at an angle β to σ_3 . On this plane, shear τ and normal σ_n stress can be defined. If the fault gouge contains fluids at a pressure P_f , the effective stress σ_{eff} is defined as $\sigma_n - P_f$. The three numbered plots show three ways to reach the Coulomb failure criterion represented by the bold line of slope $\mu = \tan(\phi)$, where μ is the friction of the rock.

σ_1 . Then the equation of the circle is:

$$\begin{cases} \sigma = \frac{\sigma_1 + \sigma_3}{2} - \frac{\sigma_1 - \sigma_3}{2} \cos(2\psi) \\ \tau = \frac{\sigma_1 - \sigma_3}{2} \sin(2\psi) \end{cases} \quad (1.18)$$

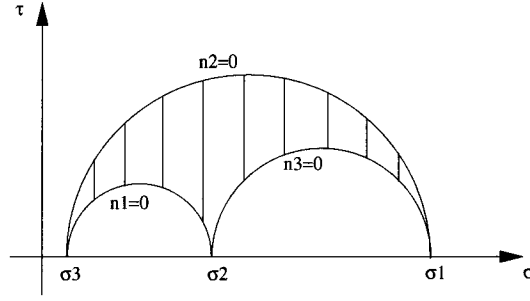


Figure 1.5: Mohr circles: $n_i = \text{constant}$ define three families of circles in Mohr space. The circle $n_2 = 0$ defines the locus of maximum shear stress and we will consider $n_2 = 0$ for optimally oriented planes.

The rupture criterion (equation 1.16) becomes:

$$\frac{\sigma_1 - \sigma_3}{2} |\sin(2\psi)| = c - \mu' \left(\frac{\sigma_1 + \sigma_3}{2} - \frac{\sigma_1 - \sigma_3}{2} \cos(2\psi) \right) \quad (1.19)$$

Differentiating with respect to ψ yields the optimal orientation for failure:

$$\psi = \frac{1}{2} \tan^{-1} \left(-\frac{1}{\mu'} \right) \quad (1.20)$$

As a result, σ_2 belongs to the optimal plane and the angle between \vec{n} and σ_1 is $\frac{1}{2} \tan^{-1} \left(-\frac{1}{\mu'} \right)$. For example, for a strike-slip regime, σ_2 vertical and $\mu' = 0.6$ lead to vertical optimal planes oriented $\psi = 30^\circ$ to σ_1 .

1.2.3 Change in Coulomb failure stress. Introduction to stress triggering

We can calculate shear and normal stress changes due to a nearby earthquake on planes optimally oriented for failure, and study the variations in the Coulomb failure stress. King et al. (1994) defined the change in Coulomb failure stress ($\Delta CFS = \Delta\tau - \mu\Delta\sigma_{eff}$ or $\Delta CFS = \Delta\tau - \mu'\Delta\sigma_n$) to examine the general problem of how one earthquake might trigger another (Figures 1.7, 1.8). While each event produces a net reduction of regional stress, events also result in stress increases. The argument is that with further tectonic loading, such sites of stress increase should be the expected location of future events. Therefore such events should be predictable from preceding ones. We will show results in terms of coseismic static stress transfer. These stress transfer studies require knowledge

about the orientation of the regional stress, the fault system geometry (main fault and known receiver faults), the slip distribution of the main shock, and the apparent friction coefficients. The output consists of maps of changes in stresses and mean strain on specified faults as well as on optimally oriented faults (Figure 1.6). However, other types of studies exist, namely the dynamic and the visco-elastic (post-seismic) stress transfer. The dynamic approach considers that the seismic waves excited by earthquakes produce dynamic Coulomb stress changes that, at distances more than about one source dimension from the fault, can be an order of magnitude larger than the static stress changes. This effect is transient (by opposition to the static change). The postseismic approach argues that postseismic stress relaxation of the lithosphere after one large event may increase the crustal stress up to the failure threshold on other faults. This effect on the interaction between events is likely to be important when long time intervals and large distances are considered. Although we recognize that the seismicity rate and distribution are probably influenced by the three above-mentioned effects, we will concentrate on static effects since this will be the basis for the forward modeling effort of the next sections of this thesis work.

The Coulomb stress change on a specified fault is independent of regional stress but

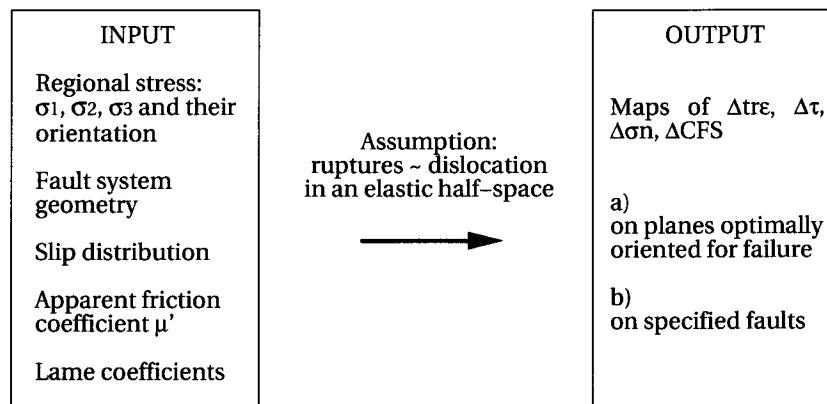


Figure 1.6: Investigating stress transfer: needed input and expected output

depends on the fault geometry, sense of slip, and the coefficient of friction. Faults most likely to slip are those optimally oriented for failure as a result of the prevailing regional stress field and the stress change caused by the main shock.

Figure 1.7 demonstrates ΔCFS in the context of the Mohr space presented in the previous section. Figure 1.8a shows strain and stress transfer on vertical optimally oriented planes (orientation shown on Figure 1.8b) due to a right-lateral uniform slip of 3 m on a vertical rectangular dislocation plane of 40 km length. The regional stress σ_{reg} is given by the horizontal maximum principal stress $\sigma_1 = 100\text{bars}$, oriented N125E. The value of apparent coefficient of friction μ' is 0.4 (e.g., corresponding to a friction of 0.8 and a Skempton's coefficient of 0.5). Large rotations of the optimal orientation are observed only at the tips of the main rupture, due to the uniform slip on the rectangular patch. To avoid singular values of stresses at the tips, elliptical slip distributions are commonly used (maximum at the center of the patch and decreasing to zero towards the edges of the patch). On Figure

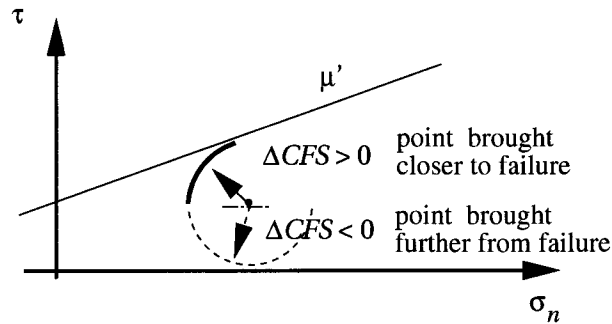


Figure 1.7: Coulomb failure stress changes ($\Delta CFS = \Delta\tau - \mu'\Delta\sigma_n$). Due to a nearby earthquake, normal and shear stress (and pore pressure by poroelasticity) can be perturbed at any location in the crust. We can interpret these changes in terms of variations in the proximity to failure. Positive values of ΔCFS mean that the point was brought closer to failure whereas negative values mean that it was taken further from the failure.

1.8a, the color scale saturates at -1 and +1 bar to show the maximum lateral extent of potentially significant changes: changes in Coulomb failure stress of up to ± 1 bar (± 0.1 MPa) extend as far as 20 km from the main fault.

1.3 Comment on regional stress

Knowledge of the in situ stress field and its spatial variations is essential for understanding contemporary geodynamic processes. For example, knowledge about σ_{reg} is needed to calculate the optimal orientation for failure, where the stress release/regional stress ratio determines whether rotations of optimal orientations should be expected due to the main earthquake.

Determining absolute values and orientation (tensor) of the regional stress is difficult. To determine the tectonic stress orientation, different types of stress indicators are used (as, for example, in the World Stress Map project Zoback, 1992). They are grouped into four categories: 1) earthquake focal mechanisms (63%), 2) well bore break-outs and drilling induced fractures (23%), 3) in-situ stress measurements (overcoring, hydraulic fracturing, etc. (9%), and 4) young geologic data from fault slip analysis and volcanic vent alignments (5%). Only the 3rd category gives absolute values of stresses. However, although broad compilations of stress-orientation data generally highlight regional tectonic stresses, deviations from the regional stress field may reveal locally anomalous stress regimes. The question has been raised whether these local stress anomalies reflect the activity of seismotectonic structures (Stewart et al., 2000).

When no information is known on the absolute value of the principal stresses, values are chosen arbitrarily as multiples of the stress drop of the main rupture, considering that σ_{reg} represents an upper bound to the maximum pre-earthquake shear stress (King et al., 1994). However, local stress anomalies at the edges of previous ruptures for example (or due to uplift, post-glacial rebound, etc.) could also affect the seismicity of the area in a

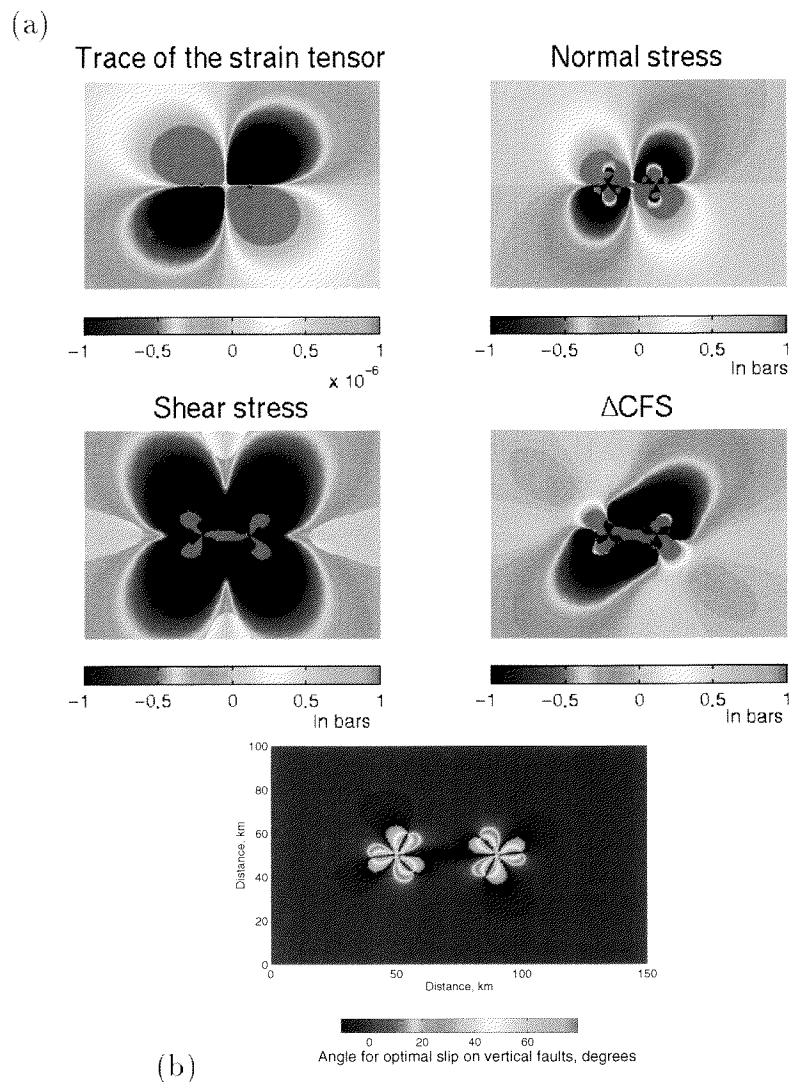


Figure 1.8: Simple stress transfer case: a right-lateral strike-slip displacement of 3 m on a rectangular vertical plane. (a) Strain and stress transfer. Strain changes are positive for dilatation and negative for compression, and normal stress changes are positive in extension and negative in compression (the color scale saturates at -1 and +1 bar to show the maximum lateral extend of potentially significant changes), (b) Optimal orientation for failure. The model parameters are the maximum principal stress $\sigma_1 = 100$ bars, oriented N125E, and the apparent friction coefficient $\mu' = 0.4$. The background blue color corresponds to the optimal orientation for failure in the presence of the regional stress only. We observe rotations up to 60° when the stress perturbation of the main event is added. Note: the slip is uniform on the rectangle, resulting in sharp singularities at the edges of the dislocation plane.

very heterogeneous way. Modeling the earthquake process has the potential to constrain regional stress magnitudes and direction because the full stress tensor is included in the calculations.

1.4 Application to the Izmit (1999, Turkey) M_w 7.4 earthquake

The M_w 7.4 earthquake that struck western Turkey on August 17, 1999 (also known as the Kocaeli, Turkey, earthquake) occurred on the east-west trending North Anatolian fault, one of the world's longest and best studied strike-slip faults. Turkey has a history of large earthquakes occurring in progressive adjacent earthquakes. Starting in 1939, the North Anatolian fault produced a sequence of major earthquakes, of which the 1999 event is the 11th with a magnitude greater than or equal to 6.7. Starting with the 1939 event in western Turkey, the earthquake locations have moved both eastward and westward (Figure 1.9). The westward migration was particularly active and ruptured 600 km of

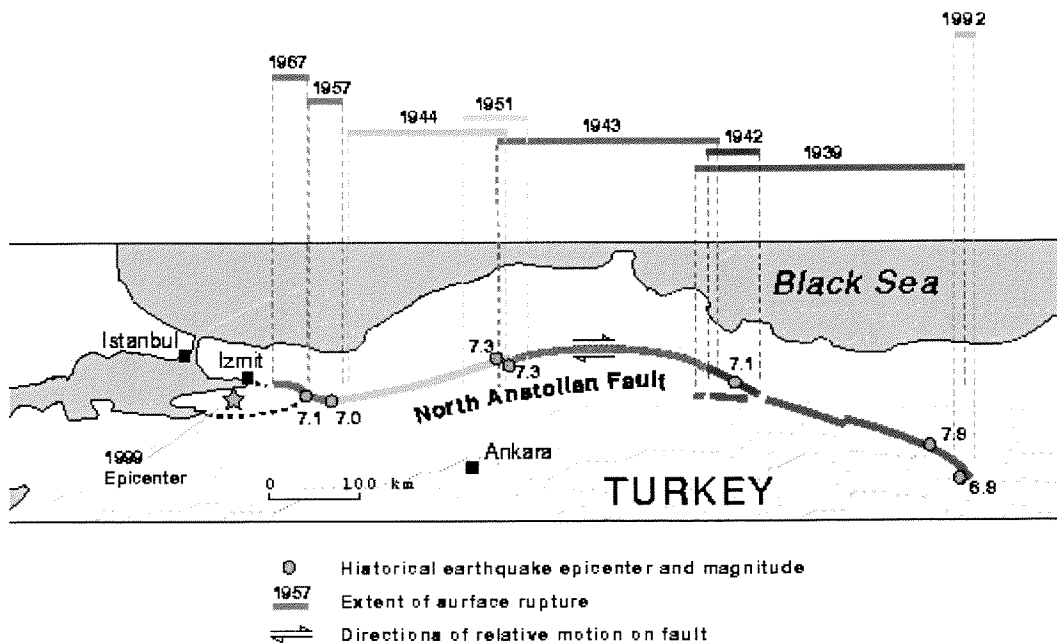


Figure 1.9: Historical seismicity of the North Anatolian fault and location of the August 17, 1999 Turkish earthquake (after Okumura et al., 1993).

contiguous fault between 1939 and 1944. This westward propagation of earthquakes then slowed and ruptured an additional adjacent 100 km of fault in events in 1957 and 1967, with separated activity further west during 1963 and 1964. The August 17, 1999 event fills in a 100 to 150 km long gap between the 1967 event and the 1963 and 1964 events (Stein et al., 1997). A simple ΔCFS calculation of the 1999 earthquake introduces stress transfer

	Strike (deg.)	Dip (deg.)	Length (km)	Depth extent (km)
Segment 1	264	85	52.5	0-22.4
Segment 2	274	85	67.5	0-22.4
Segment 3	247	85	30.0	0-22.4

Table 1.1: Geometry and dimensions of the model fault for the inversion of slip for the Izmit earthquake (Turkey, 1999). Three sub-vertical rectangular fault segments are used in the modeling (Delouis et al., 2000).

concepts that are included in the forward model described in Chapter 2. We show and discuss the complex patterns of volumetric strain changes, optimal orientation for failure and changes in Coulomb failure stress resulting from the detailed slip distribution of the Izmit earthquake obtained by Delouis et al. (2000).

1.4.1 Location and slip distribution of the Izmit (Turkey, 1999) earthquake

A data set is available for the Izmit Earthquake, including the broadband records from the global network, the near-fault strong motion records, the SAR interferometry (InSAR) data, and the observation of surface offsets. Slip inversions using seismological data only are likely to be affected by the trade-off between rupture timing and slip location (Coehe and Beroza, 1994). Since geodetic data provide an independent constraint on the space distribution of slip, Delouis et al. (2000) proposed a joint inversion of InSAR and tele-seismic data. They discretized the fault surface into 3 subvertical rectangular segments. The slip distribution is highly heterogeneous, with areas of large slip (up to 8 m) in the vicinity of the hypocenter, and other areas of as few as 25 cm of slip (Figure 1.10). The geometry and dimensions of the model fault are given in Table 1.1.

1.4.2 Changes in volumetric strain and in Coulomb failure stress

We used the slip distribution of Delouis et al. (2000) to calculate strain and stress changes on the surrounding vertical optimally oriented planes. The choice for vertical planes derives from the assumption of a homogeneous vertical σ_2 in the area surrounding the narrow right-lateral strike-slip North Anatolian Fault. However, stress perturbations due to the main shock could rotate the principal stress tensor. Having no information concerning the magnitudes of the principal stresses, we restrict the possible plane orientation to vertical.

Figure 1.9 shows the large compressional and dilatational lobes in the half-space surrounding the three segments shown on Figure 1.10 on a horizontal plane at 12 km depth. The white dots represent the first 224 aftershocks (provided by the GeoForschungsZentrum Potsdam) following the Izmit earthquake, and the black star shows the hypocenter of the Duzce earthquake which occurred three months later (November 1999). The color

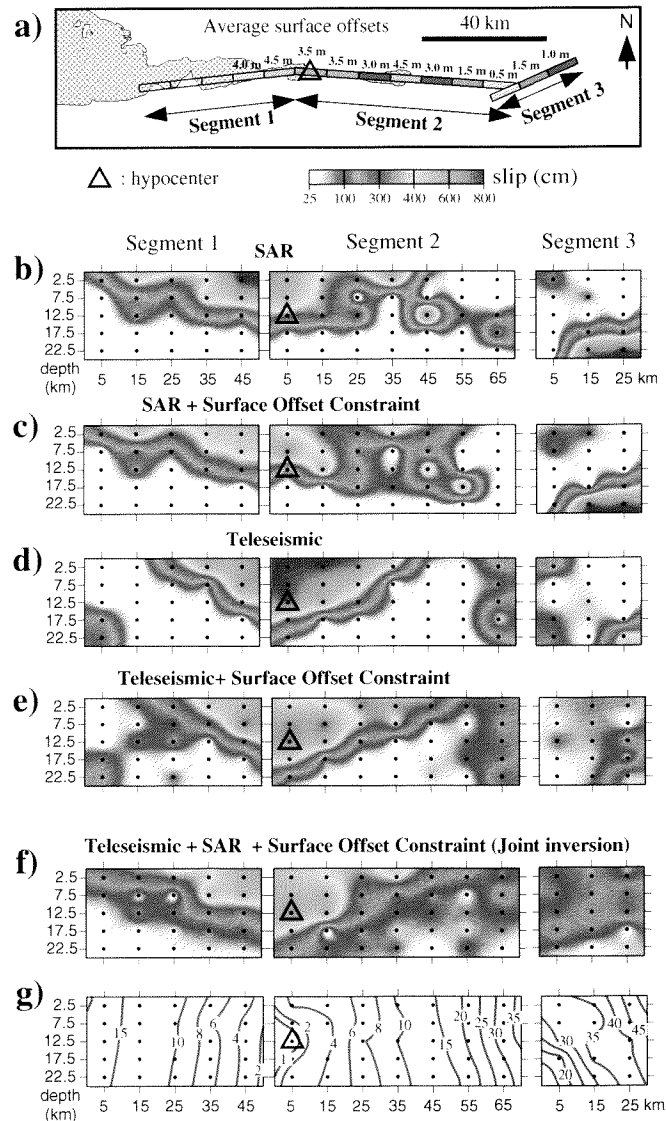


Figure 1.10: Location and slip distribution of the Izmit earthquake (from Delouis et al., 2000). (a) Map of surface rupture. The position of the epicenter (near the city of Izmit) is indicated with an open triangle and the colored lines displays the location and magnitude of the main surface breaks. The surface projection of the model fault used for the inversion (Table 1.1) is also shown. (b) to (f) Slip distributions obtained by Delouis et al. (2000) with different data sets (SAR, SAR+surface offset, teleseismic, and teleseismic+surface offset, from top to bottom) and for the joint inversion (slip distribution that we use in the stress transfer study below). (g) Time history of the rupture.

scale saturates at $\pm 5 \mu\text{strain}$. Figure 1.9 shows the superposition of the characteris-

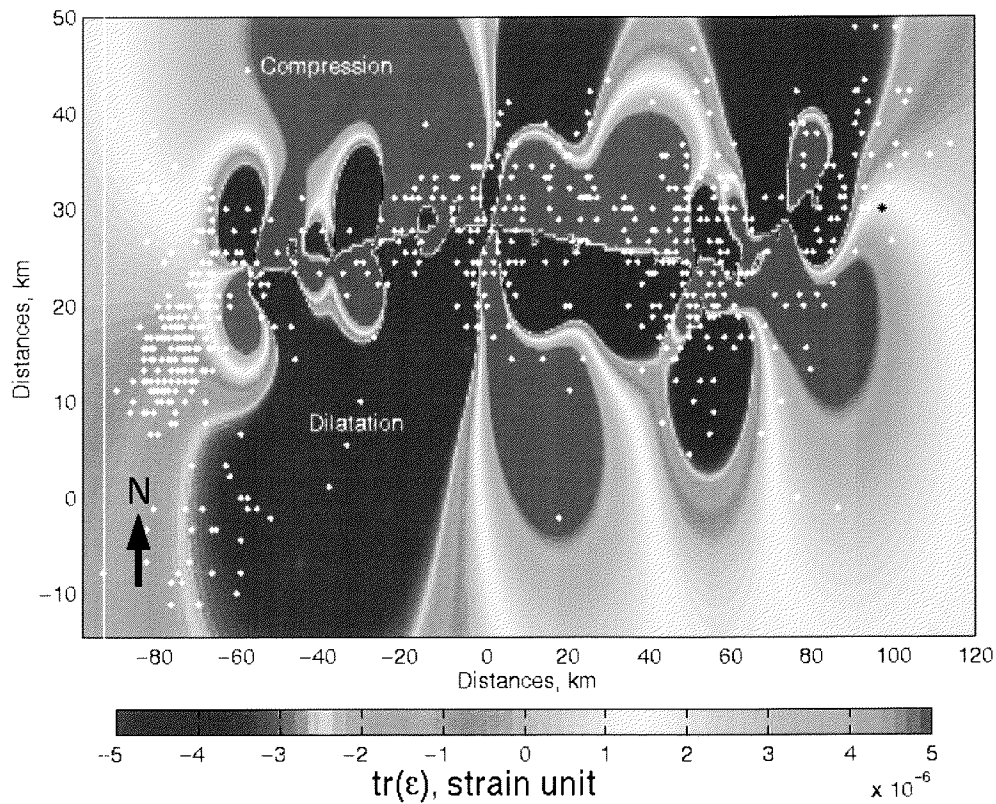


Figure 1.11: The Izmit earthquake (August 1999), volumetric strain variations calculated at 12 km depth. The distances along the x axis are given with respect to the hypocenter location. The white dots show the aftershock location and the black star shows the hypocenter of the $M_w = 7.2$ Duzce earthquake (November 1999)

tic compression and dilatation lobes for right-lateral strike-slip faulting corresponding to each unit of uniform slip on the main fault (Figure 1.10). Large lobes are observed for x between -50 and 20 km, corresponding to the region of highest slip on the main fault (junction between segment 1 and segment 2).

Most of the aftershocks occurred within less than one fault length from the main fault, where unknown details of fault geometry and slip influence stress changes. Except the cluster of aftershocks west of the fault ($x < -60\text{km}$), most of the aftershocks occur either in areas of compression or at the boundary between dilatation and compression lobes, i.e., in areas of high volumetric strain gradients (just like the hypocenter of the Duzce earthquake). A possible candidate for aftershock triggering is then fluid flow (Nur and Booker, 1972). Zankerka and Beroza (2001) studied the time-dependent rates of aftershock occurrence and found strong evidence for pore-fluid mediated triggering in the Landers aftershock sequences. In areas of large, postseismic dilatational strain, subsequent pore

pressure re-equilibration appears to trigger aftershocks creating an aftershock sequence that is locally protracted in time with respect to Omori's law (a $1/t$ decay in the number of aftershocks, where t is time after the main shock). They studied the 1992 Landers sequence within the dilational fault offset between the Johnson Valley and Homestead valley faults. After relocation of ~ 8000 aftershocks within the fault offset, they find that protracted seismicity within the jog occurs only on well defined subfaults, and that these aftershocks are triggered either through fluid infiltration into the jog or by postseismic compaction and porosity reduction along these subfaults. Such a study of time-dependent rates of aftershock occurrence should be carried out for the Izmit example as well, with relocated aftershocks, but is beyond the scope of the present work.

The computed optimal orientation for faulting on vertical faults is shown on Figure 1.12. The regional stress was chosen as $\sigma_1 = 100$ bars, oriented -35° to the East-West

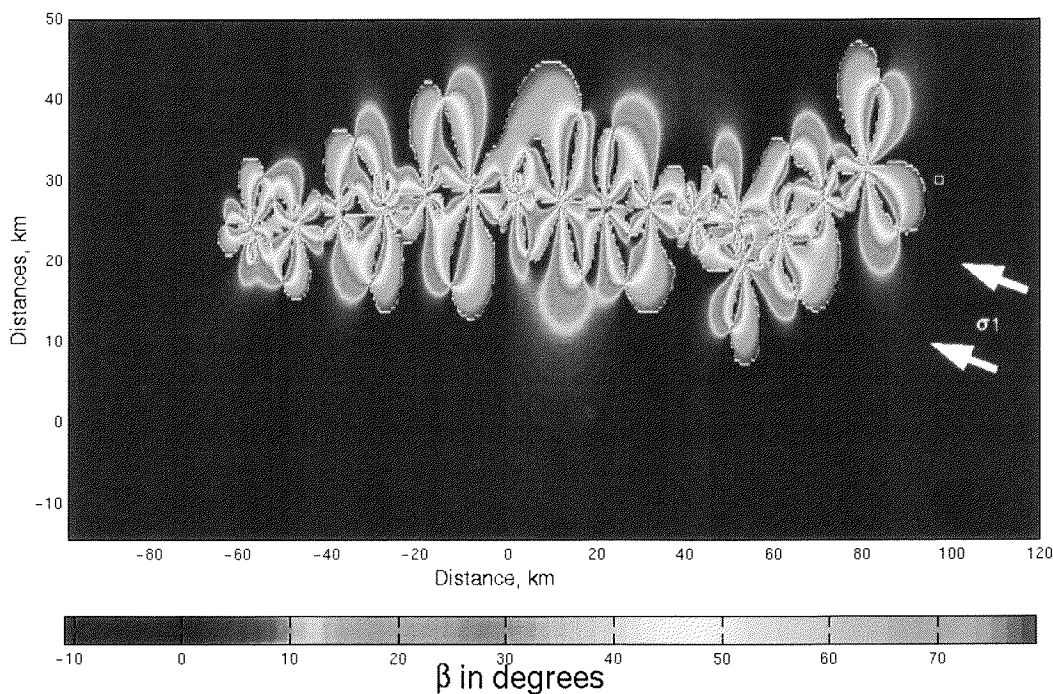


Figure 1.12: The Izmit earthquake (August 1999), optimal orientation for failure calculated at 12 km depth on vertical planes, with $\mu'=0.4$ and σ_1 oriented -35° to the East-West direction. The optimal orientations are essentially fixed by the regional stress except close to the fault ($\sim 10-15$ km) where the stress change caused by slip on the master fault is comparable to the regional stress.

direction as in Stein et al. (1997). The optimal orientations for failure (angle β with respect to σ_1), calculated at 12 km depth on vertical planes, are shown on Figure 1.12. Right-lateral planes were selected. They are essentially fixed by the regional stress, about East-West, except close to the main fault segments ($\sim 10-15$ km) where the stress change caused by slip on the master fault is comparable to the regional stress. In these areas,

the orientations can rotate up to 70° near the dislocation tips. The white square shows the Ducze hypocenter. It is located in an East-West optimal orientation area, consistent with the East-West main trend of the fault responsible for the Ducze earthquake.

On these optimal planes, shear stress and normal stress were calculated, leading to maps of changes in Coulomb failure stress (Figure 1.13). Again, the change in strike between the three fault segments as well as the non-uniformity of the slip distribution lead to the juxtaposition of characteristic lobes, forming a complex ΔCFS pattern, especially in the vicinity of the main rupture. Although a zoom out of the area would show a net reduction of Coulomb failure stress, the main event also resulted in Coulomb failure stress increases close to the main fault. Figures 1.13a and b show the map of Coulomb failure stress at 12 km depth calculated with $\mu'=0.2$ and $\mu'=0.4$, respectively, and the projection of the aftershock hypocenters on the plane $z = 12$ km depth. Although the optimal orientation changes between Figure 1.13a and Figure 1.13b and the shape of the lobes also slightly vary at distances greater than 15 km from the main fault segments, the patterns of the Coulomb failure stress changes are very similar. In both cases, a significant proportion of the aftershocks occurring near the main fault occur in areas that were brought closer to failure. However, a large number of aftershocks occur in areas that were brought further from failure. The size of the lobes near the main fault is very small (e.g., 5×5 km²). In addition, the ΔCFS patterns vary with depth and aftershock focal depth range from 1 to 30 km, with a mean value of 9 km (most of the foci are around 5 and around 15 km depth).

There are several ways of displaying stress transfer results. Other maps of ΔCFS were published for the Izmit earthquake (e.g., Parson et al., 2000) that show different patterns. A first reason for these differences is the choice of a slip distribution. The discretization of the fault plane (along strike and down-dip) and the smoothing of the slip (e.g., to get elliptical slip distributions) introduce significant differences in the ΔCFS patterns. In addition, our maps show results calculated on a slice of the half-space, at 12 km depth, but other authors (e.g., Parson et al., 2000) choose to show a map of the maximum ΔCFS values over the depth range considered. Therefore, maps of ΔCFS are not always comparable for a given earthquake and their interpretation is not always straight forward.

A study of relocated aftershocks with well-constrained hypocenters, superposed on the ΔCFS maps calculated at different depths would give more reliable results. The focal mechanism of these aftershocks should also be compared with the calculated optimal orientation for failure

1.5 Limits of the method

Where the regional stress is not known precisely, e.g., orientation of σ_1 only, and no absolute magnitude, as is the case for the North Anatolian Fault area, assumptions about the two other principal stresses have to be made. This reduces the generality of the optimal orientation calculation. In a full 3-dimensional case, the ratio of the vertical to horizontal stresses becomes important, since this determines whether strike-slip or dip-slip faulting occurs. For the example of Turkey, calculation was made for optimally oriented vertical

faults where σ_1 was assumed horizontal and much larger than the two other principal stresses (taken as 0).

In the simplified ΔCFS calculation, poroelastic effects are bundled to the friction coefficient by including Skempton's coefficient B . Skempton's coefficient depends on the distribution and orientation of cracks, the compressibility of the fluid and porous matrix, and on the saturation of the gouge (Scholz, 1990). Few values of Skempton's coefficient have been measured in fault zones (Talwani et al., 1999). In practice, B ranges from 0 to 1, and many modelers use 0.5 as a first guess. In most ΔCFS studies though, the parameter μ' was adjusted to achieve the best possible fit between the areas of increased CFS and the location of the aftershocks, making the quality of the location crucial to the study. In particular, when a detailed slip distribution for the main shock is used, it produces very small regions of positive or negative ΔCFS , with a size on the order of the error on the aftershock location (up to 5 km).

Moreover, this approach is based on two dominant assumptions, that μ' is a material constant with values ranging between 0 and 1, and that changes in pore fluid pressure induced by changes in stress are proportional to the normal stress change across the potential failure plane. However, Beeler et al. (2000) point out that in the general case of an isotropic homogeneous poroelastic model, the pore pressure changes are proportional to the mean stress, μ' is not a material constant, and it can take values between $\pm\infty$. Beeler et al. (2000) compare the two approaches in the case of reverse and strike-slip receiver faults and showed that using μ' could lead to significant errors in estimating stress changes and thus the induced seismic hazard.

The accuracy of the main fault geometry is crucial to the study since bends or jogs cause stress concentrations on different planes. These stress concentrations can potentially rotate the total stress tensor. The Duzce event occurred three months after the Izmit earthquake, on a fault dipping 60° , demonstrating the need to keep the 3 dimensions of the stress tensor in stress transfer studies.

The ΔCFS approach is inherent in the forward modeling approach for faults and fault systems described in the next chapters. The set of quasi-static 3-dimensional forward models keep stress transfer as a basic module, but also integrate large-scale tectonic loading (stress changes and pore pressure changes through poroelasticity), small-scale coseismic hydraulic property evolution, and interseismic compaction processes. This allows monitoring the time evolution of the stress state on and around a fault system and model seismicity and the consequent coseismic elastic surface deformation. In these models, μ' is no longer necessary because pore pressure is explicitly monitored and the regional stress in the model area can be calculated (at any depth at any location) as a result of tectonic loading and slip along faults.

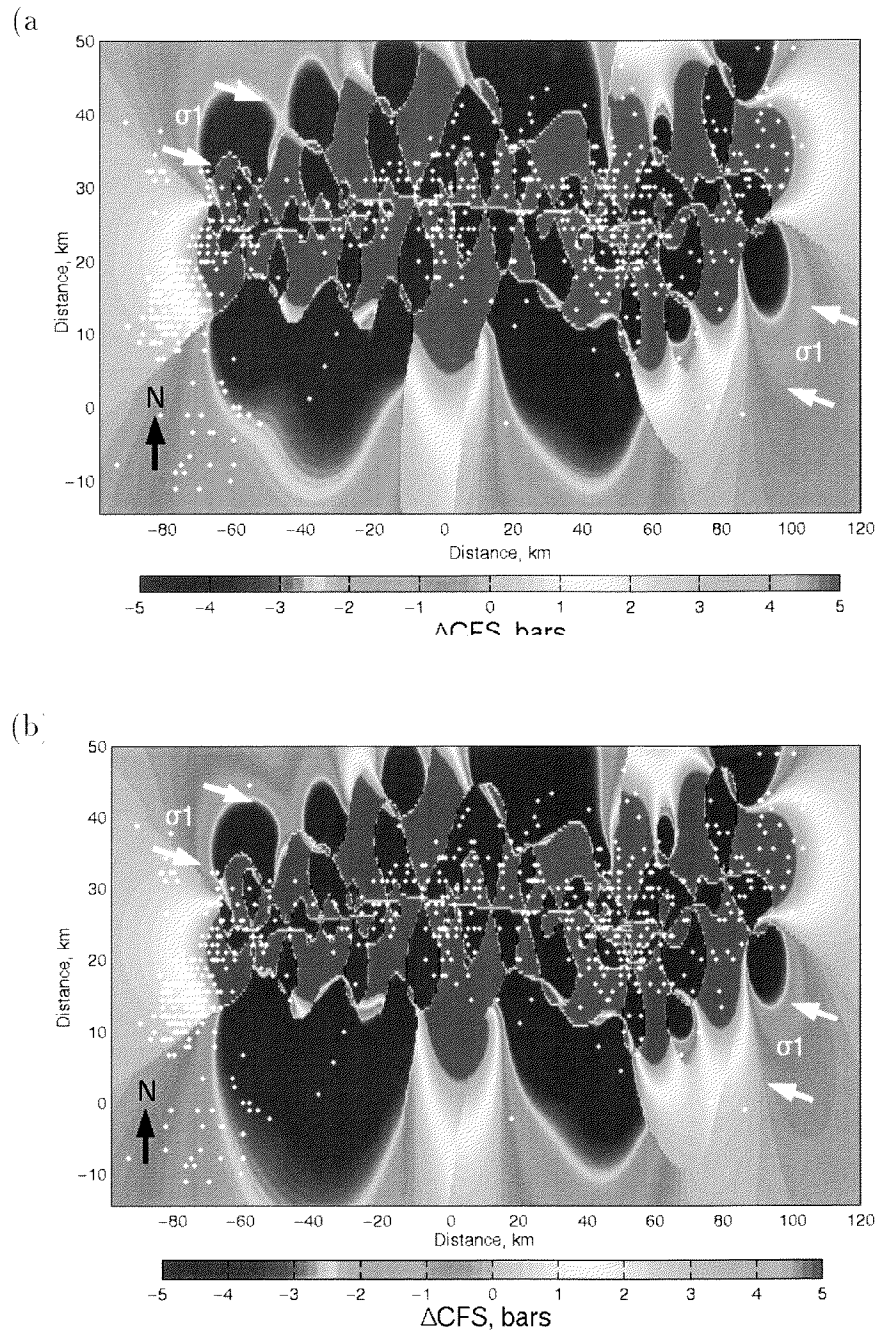


Figure 1.13: The Izmit earthquake, Coulomb failure stress changes calculated at 12 km depth on the planes defined on Figure 1.12. (a) ΔCFS with $\mu' = 0.2$, and (b) $\mu' = 0.4$. The white dots show the aftershock hypocenters. The variation in μ' does not affect the shape of the ΔCFS patterns significantly. At distances greater than 20 km, the earthquake brought the crust further from failure but the complex patterns near the fault show areas of increased CFS .

Seite Leer /
Blank leaf

Chapter 2

Forward model of earthquake generation on interacting faults including tectonics, fluids, and stress transfer

This Chapter was published in *Journal of Geophysical Research* (Fitzenz and Miller, 2001).

Abstract We present a forward model of interacting faults for systems of any geometry. The model generalizes that of Miller et al. (1996,1999) to a fully three-dimensional model where faults of any strike and geometry interact through an elastic matrix using the general solutions of Okada (1992). The model includes large-scale plate motion loading and increasing pore pressures from a source term, undrained poroelastic effects, large coseismic hydraulic property changes, and porosity creation through dilatant slip. To illustrate the basic behavior and utility of the model, results are presented of the long-term evolution (≈ 9300 years) for a generic case of a blind, dipping fault and a subvertical strike-slip fault in a transpressional environment. We show the stress state evolution along both faults, seismicity time lines, quasi-static rupture propagation including rake angle changes, local and regional stress buildup and rotations, static and dynamic fault interactions, and ΔCFS (changes in Coulomb Failure Stress) within the fault system. Large compartments of varying overpressure result on both faults from coseismic pore pressure changes and contribute to the complexity of the stress state. For the considered case, we find that the poroelastic effects on the receiver fault are about twice the change in the shear stress, providing a significant contribution to the ΔCFS . Regional stress rotations in response to the model seismicity indicate that further model developments must include dynamic generation of new faults in response to the evolving tectonic regime.

2.1 Introduction

The long-term behavior of complex fault systems is poorly understood because the community lacks a forward model that includes the dominant physics of the earthquake process. Current models of stress transfer (Stein et al., 1997; Perfettini et al., 1999; Harris and Day, 1999; Gombert et al., 2000), although useful, are limited because the slip history and an a priori apparent friction coefficient (accounting for pore pressure) must be prescribed upon a fault system to calculate stress transfer to other faults. This limitation precludes forward modeling of the long-term evolution of faults. Mechanistic and quantitative seismic hazard assessment requires an understanding of faults and fault interaction, but the paucity of paleoseismic data (Pantosti et al., 1993; Meghraoui et al., 2000) and the short duration of the instrumented seismology (about one century) limit the seismicity catalogs needed to describe the system.

In the recent decades, earthquake research focused on a number of approaches using a variety of data to understand the earthquake process. These include studies of the origin of seismic complexity (Bak and Tang, 1989; Ben-Zion and Rice, 1993; Rice, 1993; Miller et al., 1999) and theoretical and experimental developments on the physical processes involved in faulting, for example, friction (Dieterich, 1979; Blanpied et al., 1998; Scholz, 1998; Marone, 1998), rupture initiation (Dascalu et al., 2000; Voisin et al., 2000), and the importance of the fault geometry (Lockner and Byerlee, 1993). Numerous numerical earthquake models (see the review by Robinson and Benites, 1995) focus on different aspects of the earthquake process. These include stable versus unstable sliding (Segall and Rice, 1995), the effect of fluid migration (Yamashita, 1998) or pore creation due to slip on the seismicity (Yamashita, 1999), shear-enhanced compaction (Sleep and Blanpied, 1992, 1994), and models of fault behavior (Ben-Zion and Rice, 1993; Robinson and Benites,

1996; Rundle, 1988). These models are not three-dimensional, not fully forward (the first rupture is imposed), do not consider the interaction between stress and pore pressure (Hardebeck and Hauksson, 1999) or do not consider the “fault valve” aspect of fluid flow (which requires that permeability be treated as a dynamical property within fault zones).

Fluids are widely believed to play an important role in earthquakes and faulting, and a number of studies focused on mechanisms for generating and maintaining high pore pressures within fault zones. Overpressures can result from frictional heating (Spray, 1995), creep compaction (King et al., 1994; Streit and Cox, 2000; Sleep and Blanpied, 1992; Sleep, 1995), dehydration of hydrous minerals, or a direct fluid source from a ductile root (Rice, Academic, San Diego, Calif., 1992). Conceptual models that identify the role of fluids include isolated compartments (Byerlee, 1993), and the fault valve model that recognizes the dynamical aspect of fluid flow and tectonic loading (Sibson, 1993; Miller et al., 1996).

Each of these studies provide important insight into certain aspects of the earthquake process, but a model that combines these components into a forward and deterministic model has not been developed. The purpose of this paper is to synthesize some of these components into a general and forward model that includes the dominant processes believed to control earthquakes and to investigate the faulting properties and the evolution of complex fault systems. The approach is to model processes occurring at the small scale and to allow these processes to evolve and find their equilibrium state in the large-scale system within which they operate.

The two dominant mechanical processes that we consider are the state of stress in the system, and the pressure of the fluids. The model generalizes that of Miller et al. (1996, 1999, submitted manuscript, 2000), which was limited to vertical strike-slip faults, to consider fault systems of any geometry. The primary mechanics that we consider at this stage are elastic dislocation theory, undrained poroelasticity, large coseismic permeability changes within the fault zone, and a simple switch from static to dynamic friction.

We assume that elastic dislocation theory is a good approximation for brittle crustal faulting as evidenced by the successes in modeling coseismic deformation from satellite interferometry (Massonnet et al., 1993) and stress-triggering models (Stein et al., 1997). We further assume that pore pressures play an important role in the process (Hubbert and Rubey, 1959; Sibson, 1973; Rudnicki, John Wiley, New York, 1985; Sibson, 1992) in that knowing (or modeling) both the state of stress and the state of pore fluid pressure on a fault is necessary to understand earthquake mechanics in intraplate and interplate regions. Observations of rock samples taken in fault zones (Robert and Boullier, 1993; Chester et al., 1993) substantiate the important role of fluids. Fluid-assisted processes are shown to be significant in the highly strained fault cores, evidenced by pervasive syntectonic alteration of the host rock minerals to zeolites and clays and by folded, sheared, and attenuated crosscutting veins of laumontites, albites, quartz, and calcite (Chester et al., 1993). We also assume that mature fault zones are low-permeability, fluid-saturated zones that coseismically change to high-permeability fracture zones (e.g., the fault valve model). Finally, we assume a rigorous quasi-static model, ignoring for now time-dependent pro-

cesses of wave propagation and diffusion.

We explore model results from a generic blind dipping, strike-slip fault system to determine how this system evolves in time with stress interaction between the two faults. The model is adaptable to any fault system in any tectonic environment. Modifications and improvements to the models of Miller include, (1) monitoring the full stress tensor, (2) undrained poroelastic effects, (3) oblique loading from the base of the fault system, and (4) a separation of elastic stress transfer rupture propagation and pore pressure redistribution. We show (1) the stress state evolution and generation of pore pressure compartments, (2) seismicity time lines and frequency-size statistics, (3) slip and rake angle evolution during rupture, (4) slip distributions, (5) fault interaction during rupture, (6) principal stresses and orientation along a profile perpendicular to fault strike, and (7) Δ CFS (changes in Coulomb Failure Stress) due to a large event on the strike-slip fault and subsequent earthquakes on the strike-slip fault, on the dipping fault, and on optimally oriented faults. We consider the problem from a tectonic scale while keeping small-scale processes intact. We make significant approximations to simplify the physics, but we try to ensure that these approximations have substantial supporting evidence. We discuss the model assumptions in detail and the physical processes not currently considered. We also propose some directions for future research.

2.2 The Model

An arbitrary generic model that we chose to investigate is a coupled blind dipping-strike slip fault system (Figure 2.1) in a transpressional environment. The faults consist of a matrix of computational cells representing rectangular dislocations and discrete sealed fluid pressure compartments in a deforming elastic half-space. Central to our approach is coupling the analytical elastic deformation solutions of *Okada* [1985, 1992] to the coseismic permeability-change conceptual model of Miller et al. (1996). The permeability of these compartments is taken as zero in the interseismic periods and very large (e.g., allowing for an “instantaneous” pore pressure redistribution; see Miller and Nur, 2000, S. A. Miller (submitted manuscript, 2000), and equation (2.5)) when a rupture occurs. Plate motion is represented as a displacement through time on a dislocation plane located at the base of the seismogenic layer, infinite in all directions except along the plate boundary. Plate motion increases shear stress, normal stress, and pore pressure (through poroelasticity) along the fault planes, while pore pressures increase through poroelastic effects and assumed pore closure within the faults. When a cell reaches the Coulomb failure stress, we use *Okada*’s [1985, 1992] analytical solutions to calculate the stress changes on all other cells of the faults. For a given dislocation vector applied on a rectangular plane at depth, these equations [*Okada*, 1992, Tables 6 to 9] provide the displacement vector and the displacement derivatives in any location in the surrounding elastic half-space (Poisson solid). From the strain tensor we calculate the stress tensor using Hooke’s law and the resolved shear and normal stress along the prescribed fault planes. Slip is calculated through the stress drop at rupture. For a given cell we calculate the stress drop induced by a unit slip in the direction of the maximum shear stress, and we then invert the rate to obtain the slip magnitude that causes this stress drop (see also Robinson and Benites,

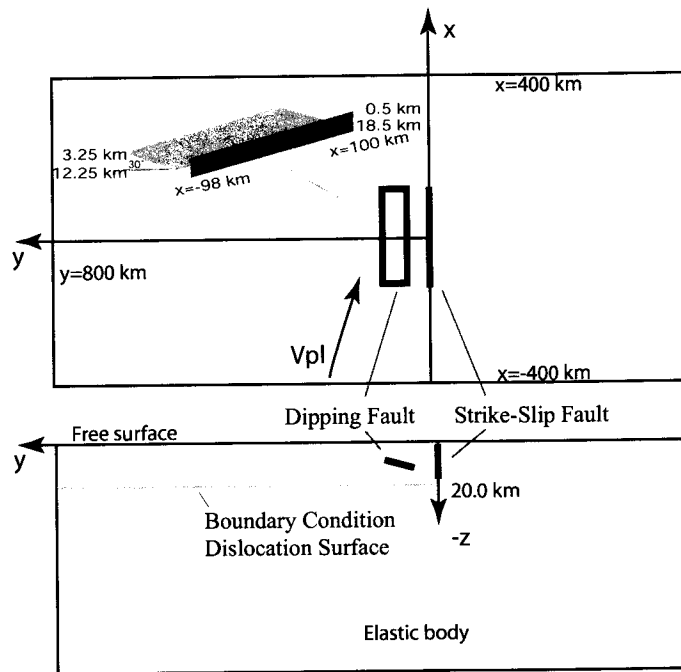


Figure 2.1: Model of a coupled blind-dipping, strike-slip fault system. The 3-D model is made of two faults discretized into computational cells, interacting through an elastic half-space, in a transpressional environment. Plate motion is imposed at the base of the seismogenic layer as a dislocation. The base is infinite in any direction, one edge being at the downward edge of the strike-slip fault.

1995). Note that this assumption relates only to the stress drop per subevent and not to the total (static) stress drop after a rupture (see Section 4). We include the following physical processes in this model: (1) quasi-static tectonic loading, (2) fluid-saturated faults, (3) fluid sources (either a direct fluid source or a pore space reduction mechanism), (4) elastic dislocation theory, (5) poroelasticity in undrained conditions, (6) small-scale coseismic changes in hydraulic properties, (7) porosity creation due to slip (Sleep, 1995), and (8) a switch from static to dynamic friction when a cell starts to slip (see discussion by Miller (submitted manuscript, 2000)). We monitor the full stress tensor and the static and coseismic fault interaction (throughout quasi-static rupture propagation). We assume heterogeneous fluid sources and a displacement boundary condition at the base of the model fault system (e.g., all tectonic loading is applied via basal drag from the underlying ductile lithosphere).

2.2.1 Choice of Initial Conditions and Processes

Model geometry

The model geometry is imposed, and we focus here on the example of a coupled blind dipping/strike-slip fault system in a transpressional environment. Such coupled systems are observed in nature, with varying distance between the strike-slip fault and the thrust fault, for instance, near the big bend in central California (e.g., San Andreas/Kettleman Hills, (Ekström et al., 1992)). The subvertical (dip of 85°) strike-slip fault acts as the plate boundary. The dipping fault is an intraplate fault dipping at 30° , buried from a depth of 3 km and extending to 12.25 km and parallel to the strike-slip fault. Both faults measure 200 km (from $x=-100$ to $+100$ km and $y > 0$) by 18.5 km (downdip), consisting of 3700 computational cells each. The minimum distance between the two faults is 10 km. The plate motion vector is dominantly subparallel but has a fault normal component (oriented 15° to the fault strike) and is applied uniformly on a horizontal plane lying at 20 km depth. The initial conditions are listed in Table 2.1. Shear stress is initially zero on the fault system at $t=0$, and the initial normal stress is assumed to be the lithostatic stress.

Pore pressure

It is generally accepted that the fractures are interconnected and the pore pressure gradient is hydrostatic at shallow depths, while excess pore pressures likely exist below ~ 3 km depth (see review by Quattrocchi, 1999). For computational convenience, we assume an initial uniform overpressure of $\lambda = P_f/\sigma_n = 0.7$ below 3 km depth for the strike-slip fault and a hydrostatic pressure gradient for the dipping fault. We impose a constant hydraulic head boundary condition on the first row of cells on each fault. Since the top of the strike-slip fault is near the surface (500 m), it implies that the pore pressure of all the regions of the fault temporarily connected to the first row becomes hydrostatic.

Pore pressures increase from a poroelastic effect approximated by

$$\Delta P_f|_{\text{no flow}} = B \times \frac{\text{tr}(\Delta\sigma)}{3}, \quad (2.1)$$

Initial model parameters	Range of values
Cell size	2000 m along strike by 500 m updip
Fault area	200 km along strike by 18.5 km updip
Plate velocity	35 mm yr ⁻¹ oriented 15° to the fault strike
Lame coefficients	$\lambda_{\text{lame}} = G = 30 \times 10^9$ Pa,
Time step	time required to initiate failure on exactly one cell
Compressibility $\beta = \beta_\phi + \beta_f$	10 ⁻³ MPa ⁻¹
Porosity ϕ	initial, 5%; maximum, 9%
Skempton coefficient B	0.6
Initial normal stress	lithostatic, $\rho_r g z$, $\rho_r = 2700$ kg m ⁻³
Initial shear stress	0
Initial pore pressure gradient	hydrostatic except for $-z > 3$ km depth on the strike-slip fault: 0.7* normal stress
Compaction	for $-z < 3$ km, $\dot{\phi} = 0$ for $-z > 3$ km, $0.8 \times 10^{-6} < \dot{\phi} < 0.5 \times 10^{-5}$ year ⁻¹
Fluid sources $\dot{\Gamma}$	none
Friction coefficients	static, $\mu_s = 0.6$; dynamic, $\mu_d = 0.5$
Dilatation coefficient ^a β_m/W	18x10 ³

Table 2.1: Model Parameters and Initial Conditions. ^a After *Sleep* [1995]

where P_f is the pore pressure, $\text{tr}(\Delta\sigma)$ is the trace of the tensor of stress changes (positive in compression), and B is Skempton's coefficient. Equation (2.1) is applied in undrained conditions (no flow) on sealed compartments of homogeneous pore pressure. B is a nondimensional parameter of poroelasticity related to the contrast between the compressibility of the fluids and the compressibility of the rock: $B = (K_u - K)/(\alpha \times K_u)$, where K_u is the effective modulus of a porous medium filled by a fluid of compressibility β_f , K is the effective modulus of a porous rock saturated by a fluid at constant pressure P_f (dependent only on the compressibility of the solid phase and porosity), and α is the coefficient in the law of effective stress ($\sigma_{\text{eff}} = \sigma_n - \alpha P_f$, $\alpha \sim 1$ (Nur and Byerlee, 1971)). Generally, $K_u > K$, since it is more difficult to deform a rock when fluids cannot flow. For a very porous medium (K small), B tends toward 1, and for a very compressible fluid ($K \sim K_u$), B tends toward 0. As pointed out by Scholz (1990), the geometry is also very important. *Scholz* [1990, p. 329] writes that for a change in uniaxial stress in a cracked solid where the cracks are perpendicular to the stress, B is ~ 1 , whereas for parallel cracks, B is almost 0. Using the undrained response of the Bad Creek Reservoir (South Carolina), *Talwani et al.* (1999) determined an in situ estimate value 0.66 for the Skempton's coefficient of a shallow shear zone in a gneiss massif. In their review of experimental observations, *Beeler et al.* (2000) report the range for B as 0.5-0.9 for granites, sandstones, and marbles. In this simulation, having no constraint on this parameter, we chose a value of 0.6.

Pore pressure can also change in the sealed compartments by reducing the available

pore space, or by a direct “fluid pressure source” via

$$\frac{\partial P_f}{\partial t} \Big|_{\text{no flow}} = \frac{\dot{\Gamma} - \dot{\phi}}{\phi(\beta_\phi + \beta_f)}, \quad (2.2)$$

where ϕ is the porosity, β_ϕ and β_f are the pore and fluid compressibility, $-\dot{\phi}$ is a rate of inelastic porosity reduction (e.g., from pressure solution, compaction) and $\dot{\Gamma}$ is a direct fluid source. Fluid sources are necessary to maintain overpressures because in the absence of a mechanism to increase pore pressure, diffusion would reduce pore pressures to hydrostatic over long timescales. In fault zones, substantial evidence suggests that pore pressures are in excess of hydrostatic, implying that a fluid source must exist (Quattrocchi, 1999; Byerlee, 1993). Many different mechanisms are possible for the fluid sources, most of which are unconstrained. Potential fluid sources include, among others, creep compaction (Sleep and Blanpied, 1994) and dehydration of hydrous minerals (namely, through frictional heating (Spray, 1995; Rice and Cleary, 1976)). No detailed mechanism for fault zone compaction or fault creep is explicitly considered. One such mechanism was proposed by Sleep and Blanpied (1994), who constructed a model (based on experimental observations) in which compaction is due to ductile shear creep between seismic events in the earthquake cycle. Such grain-scale creep results from deformation at grain-grain contact points due to deformation under stresses. The deformation process can be cracking, dissolution, crystal plasticity, etc. This mechanism is very efficient at elevating pore pressure even for very small amount of creep and is a viable mechanism for increasing pore pressure in fault zones. As in the present work, they assumed that fluids cannot escape the fault zone. Another compaction mechanism could be the mechanical compaction (rearrangement of grains) due to increased normal stress. This would require that grains be able to slide past each other, and conditions in which this would be possible (values of normal stress, initial porosity, grain size, friction) are to be investigated. Since fluid sources are unconstrained, we assume a random distribution (over a small range) of sources, either via a direct fluid source $\dot{\Gamma}$ or a plastic pore closure $\dot{\phi}$ (only $\dot{\phi}$ is considered in the present study). Although we recognize their importance, we do not include any depth or temperature dependence at this point. Any or all of the terms in (1) or (2) can be randomized, and any one of these would provide an initial heterogeneity. Without this heterogeneity the faults would initially break row by row, since the boundary conditions (size of the plate) are chosen to avoid lateral changes in the effect of tectonic loading. Other properties could also be arguably randomized (i.e., fault zone width or porosity) but are made uniform in this model. No other assumptions are imposed as initial conditions (e.g., overpressured patch, initial hypocenter).

Coulomb failure

The failure stress is the Coulomb failure stress that explicitly includes the pore pressure state. The initial static friction coefficient (μ_s) is taken constant and uniform over the fault planes and is assumed to be 0.6. When slip occurs, friction reduces to a dynamic value ($\mu_d = 0.5$) for the duration of that event. This switch approximates a slip-weakening model for friction and is discussed by Miller (submitted manuscript, 2000). After the event, friction is reset to the static value. An important aspect of friction that we currently

ignore is the increase in friction with time between two plates in stationary contact (e.g., a fault zone): $\mu \propto \log(t)$. This logarithmic time dependence has a physical basis in terms of yielding between points of contact (Scholz, 1990, pp.46-80) and is widely supported by experimental observations. We recognize the importance of this strengthening but do not include it here because it adds another level of iteration when determining the time step necessary to initiate one hypocenter (e.g., rigorously quasi-static). Incorporating a full rate-and-state constitutive friction law (see Dieterich, 1979, and review by Gomberg et al., 2000) is beyond the scope of the current study.

Ruptures propagate along the predefined fault planes, although Kame and Yamashita (1999) show that rapidly growing cracks have a natural tendency to spontaneously curve and have a large impact on the arresting mechanism of earthquake ruptures. Other evidence shows that a rupture can stop on a nonfavorably oriented preexisting fault and propagate farther by creating new optimally oriented cracks in the country rock (e.g., the Landers earthquake, Bouchon et al., 1998a). In future model developments, the constraint of rupture along predefined planes will be lifted by generating new failure planes in response to the stress state of the system.

Dilatant slip

Porosity production is modeled by frictional dilatancy and is assumed to be proportional to slip. In fault zone dilatancy models (see review by Scholz, 1990), dilatancy is assumed to occur within the fault zone as slip occurs during nucleation (due to joint dilatancy) in which the fault walls must move apart to accommodate slip (interlocking, riding up) or due to shear of granular material (breccia, gouge) within the fault zone. Porosity production follows the model of Sleep (1995):

$$\frac{\partial \phi}{\partial \delta} = \frac{\beta_m(\phi_m - \phi)\tau}{W\phi_m\sigma_n}, \quad (2.3)$$

where ϕ is the porosity created with slip δ , β_m is the fraction of energy that goes into the new crack creation, ϕ_m is the saturation porosity which limits the amount of crack porosity that can be generated, τ and σ_n are the shear and normal stress acting on the slipped cell, and W is the fault zone width. The values for β_m , ϕ_m , and W were taken from Sleep (1995). The porosity change is used to update the storage capacity ($\beta_\phi\phi$) of the cells just before the redistribution of pore pressure. Because porosity changes through dilatant slip, the rate at which pore pressures increase (equation (2.2)) for any cell also changes in time due to the porosity dependence of the pore pressure increase rate.

2.2.2 The numerical model

The flowchart of the model algorithm is shown in Figure 2.2. After setting the initial conditions the time step necessary to initiate failure of exactly one cell is calculated by solving (2.4) for each cell i and by choosing the minimum of the calculated time steps Δt_i . Δt_i is the exact time step needed to bring cell i (which stress state is known at time

t) to brittle failure:

$$\Delta t_i = -\frac{\mu_s \times [(\sigma_n)_i + (P_f)_i] + \tau_i}{\Delta \tau_i + \mu_s \times [(\Delta \sigma_n)_i + (\Delta P_f)_i]}, \quad (2.4)$$

where $(\Delta \sigma_n)_i$, $\Delta \tau_i$, and $(\Delta P_f)_i$ are increments of normal stress, shear stress, and pore pressure per time unit, respectively. $(\Delta P_f)_i$ includes both the poroelastic changes (equation (2.1)) and the effect of the source term (equation (2.2)).

The plate displacement is then calculated for this time interval, and the stresses and pore pressures are calculated for all cells of the fault system. For the cell that reached the Coulomb failure condition we calculate the amount of slip needed to decrease the shear stress by the assumed stress drop (25% of the prefailure stress in the simulation studied below, see discussion in section 2.3.3). The porosity created through this dilatant slip event is calculated with equation (2.3) (Sleep, 1995), the friction coefficient of the cell that failed is reduced to the dynamic friction value, and the cell hydraulically communicates with its nearest neighbors. The new stress state is then calculated on both faults. The changes in stresses and pore pressure from the failure of this cell (still in undrained conditions) can initiate failure of other cells, and the model is then cycled until all cells are below the failure condition.

Assuming that propagation of the rupture front is much faster than fluid flow, the elastic and undrained poroelastic stress changes equilibrate before pore pressures are equilibrated. This scenario is presumably more realistic than the model of Miller et al. (1999), who redistributed pore pressure simultaneously with the stress transfer.

Pore pressure redistribution among cells that failed is calculated by conserving fluid mass [Miller et al., 1999]:

$$\bar{P}_f = \frac{\sum_{i=1}^m (\phi\beta)_i (P_{f_i} - \rho g \Delta z)}{\sum_{i=1}^m (\phi\beta)_i} + \rho g \Delta z, \quad (2.5)$$

where ρ is the fluid density, \bar{P}_f is the equilibrium fluid pressure among the m affected cells, weighted by the storage capacity of each cell $(\phi\beta)_i$, and appended with a hydrostatic gradient with depth. The term Δz is measured from the depth of the slipped source cell, so a negative sign accompanies the shallower cells.

Pore pressure redistribution may induce additional failures, and if so, the algorithm returns to the “undrained rupture” loop just described. This sequence is then cycled until the system is in equilibrium. These (quasi-static) rupture loops ignore wave propagation but provide insight into the propagation of the ruptures and coseismic stress transfers. Before the next time step is calculated, permeability is reinitialized to zero (all cells are sealed) and the friction coefficient is reset to the static value. The redistribution of the stresses is made simultaneously in the case of multiple failures during the same sequence in the same time step.

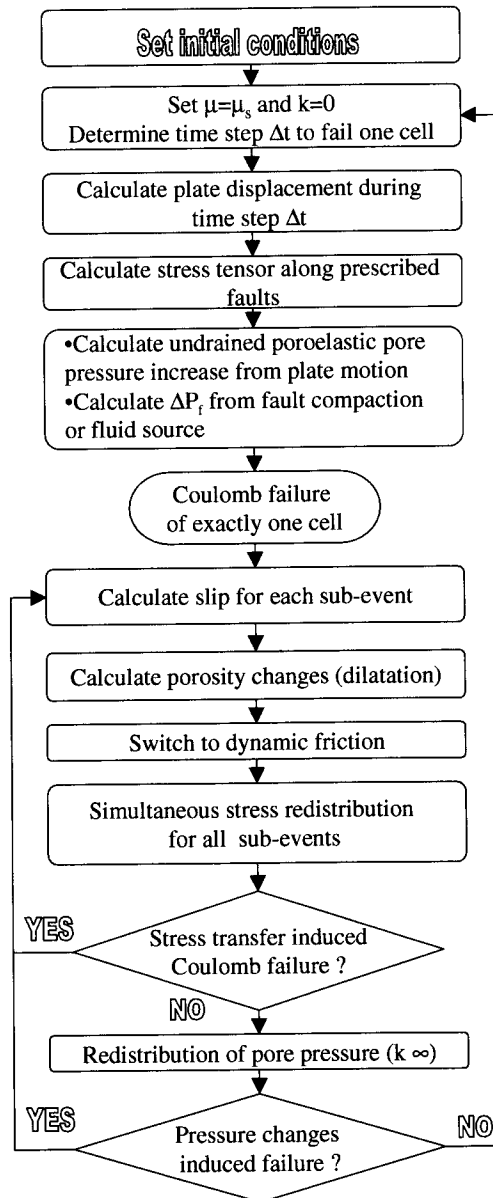


Figure 2.2: Flowchart of model algorithm. The model includes quasi-static tectonic loading, fluid-saturated faults, fluid sources, elastic dislocation theory, poroelasticity in undrained conditions, small-scale coseismic changes in hydraulic properties, frictional dilatation, and monitoring of full stress tensor. (See text for more details.)

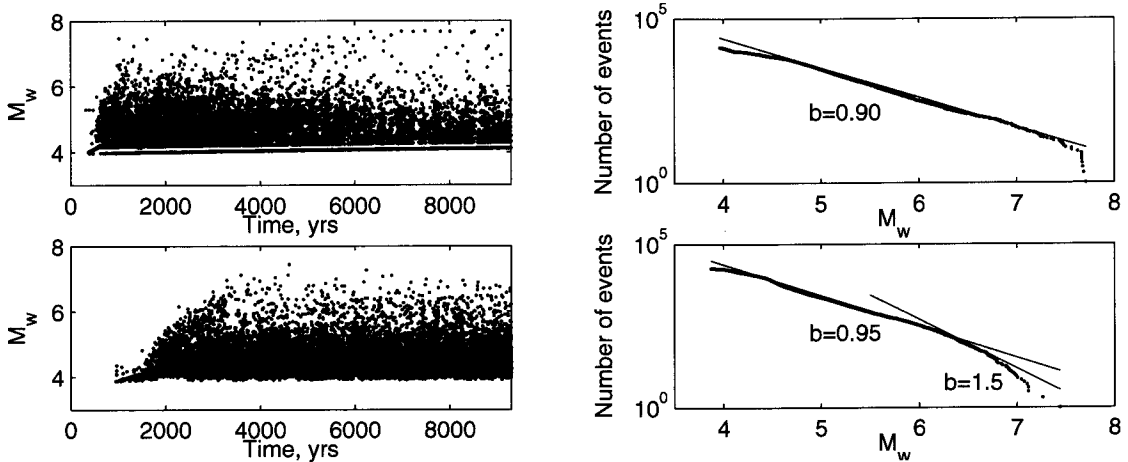


Figure 2.3: (left) Seismicity time line and (right) corresponding frequency-magnitude relationship for (top) the strike-slip fault and (bottom) the dipping fault. The minimum moment magnitude (M_w) is ~ 3.8 because of the size of the subfaults (or cells, i.e., 2 km along strike by 0.5 km along dip). M_w is calculated from the scalar seismic moment via equation (2.6). The maximum moment magnitude for the time window (~ 9300 years) studied is $M_w \sim 7.7$. The frequency-size statistics show that a wide range of event size are generated in this model with b -values ~ 1 for each fault.

2.3 Model Results

2.3.1 Seismicity Time Line and Frequency-Magnitude Statistics

The seismicity time lines are shown for the strike-slip fault and for the dipping fault in Figure 2.3. The minimum moment magnitude (M_w) is ~ 3.8 because of the size of the subfaults (or cells, i.e., 2 km along strike by 0.5 km along dip). M_w is calculated from the scalar seismic moment via

$$M_w = \frac{2}{3} \log_{10} M_O - 10.7, \quad (2.6)$$

where M_O (in dyn cm) is measured in the model. For example, 10 cm of slip on one cell corresponds to a moment magnitude of $M_w = 3.62$. The maximum moment magnitude for the time window (≈ 9300 years) studied is $M_w \sim 7.7$ representing failing of a patch on the order of 18 km in depth by 100 km.

Seismicity first appears on the plate boundary strike-slip fault because of a higher stress buildup rate. The boundary (see Figure 2.1) between the moving elastic layer ($y > 0$ and $z > -20$ km) dragged from the base and its elastic symmetric counterpart ($y < 0$ and $z > -20$ km), free of imposed motion and welded on top of the elastic half-space defined by $z < -20$ km, undergoes large stress concentrations that increase with depth. This affects mostly the strike-slip fault since the dipping fault is both shallower and farther from the plate boundary. Therefore no rupture occurs on the “intraplate” dipping fault during the first 949 years, during which high pore pressures are being buildup. Once

the effective stress is low enough (e.g., high pore pressures), the failure criterion can be reached even for low shear stresses, and the seismicity begins on the dipping fault (see also discussion below). The first large events ($M_w > 6.5$) occur after 990 years of loading on the strike-slip fault and after 3051 years on the dipping fault, about the time necessary to fail large portions of the initially unstressed fault.

The frequency-size statistics (Gutenberg-Richter (GR) empirical laws) show that a wide range of event size is generated in this model with b values of ~ 1 for each fault. This is consistent with other dislocation models that assume highly heterogeneous fault strengths (Robinson and Benites, 1995; Ben-Zion and Rice, 1995). The GR laws also exhibit a change in the slope to 1.5 about $M_w > 6.5$, consistent with theoretical predictions (Rundle, 1989). This change is related to a change in the dimensionality where small earthquakes can grow in both length and width (two dimensions), while large earthquakes have no bounds in rupture length but their downdip width is limited by the thickness of the seismogenic layer (Pacheco et al., 1992). In this model, heterogeneous fault strengths naturally arise through the complex stress paths followed in the $\tau - \sigma_{\text{eff}}$ stress state.

2.3.2 Fault Stress State Evolution

Figure 2.4 shows the evolution of the stress state on the strike-slip fault and on the dipping fault (see Table 2.1).

The stress state on both faults becomes complex because of the dynamical interaction between changes in stress and pore pressure. That is, when a large rupture occurs, dramatic pore pressure changes on the strike-slip fault lead to a compartmentalization of the fluid pressure distribution (see Figure 2.5a, left). These large compartments differ from the results of Miller et al. (1999) and are related both to the initial conditions in the first 3 km (hydrostatic pore pressure and no source term) and the manner in which pore pressure is redistributed. In the current model, pore pressures are redistributed only after stress transfer is equilibrated. For ruptures that propagate upward and laterally at shallow depths the final slipping patch includes numerous cells at hydrostatic pore pressure from the constant head boundary condition. Therefore, when pore pressure is redistributed, it can drop dramatically (e.g. from $\lambda > 0.8$ down to $\lambda \sim 0.5$, see Figure 2.5a, left). These large-scale pore pressure changes shift the corresponding points to the right in Mohr space (Figure 2.4). Conversely, the shear stress distribution does not develop such compartments (see Figure 2.5a, right). These zones of low pore pressure and shear stress subsequently act as “locked” parts of the fault because of the time needed to rebuild pore pressure and/or shear stresses to the failure condition. Pore pressure compartments also develop on the dipping fault but with a smaller range of pore pressure (see Figures 2.5c-2.5d).

On both faults, these compartments gradually increase in pressure with time from the assumed pore pressure increase rate and change abruptly when a rupture propagates within the fault system. Abrupt pore pressure change can occur through redistribution or due to the poroelastic effect. On the contrary, the stress state on the dipping fault is confined to a small region of stress space. High pore pressures limit the normal stress direction ($\lambda = P_f/\sigma_n$ in the range 0.70-0.95), and the shallow depth interval (from 3 to 12 km) limits the range of possible shear stress states. The difference in the behavior of

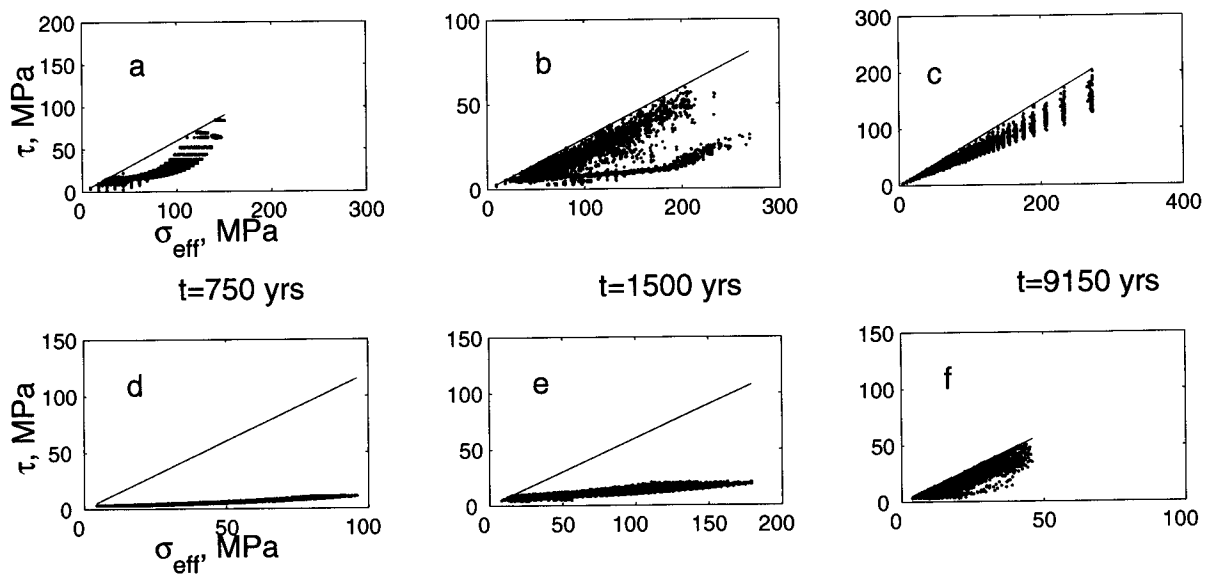


Figure 2.4: Time evolution of the stress state (a-c) on the strike-slip fault and (d-f) on the dipping fault. The dipping fault is highly overpressured (the range in σ_{eff} is small). The stress state tends to fill the space available between the static friction and the line defined by the stress drop until a large rupture occurs and relieves the fault by dramatically reducing pore pressure.

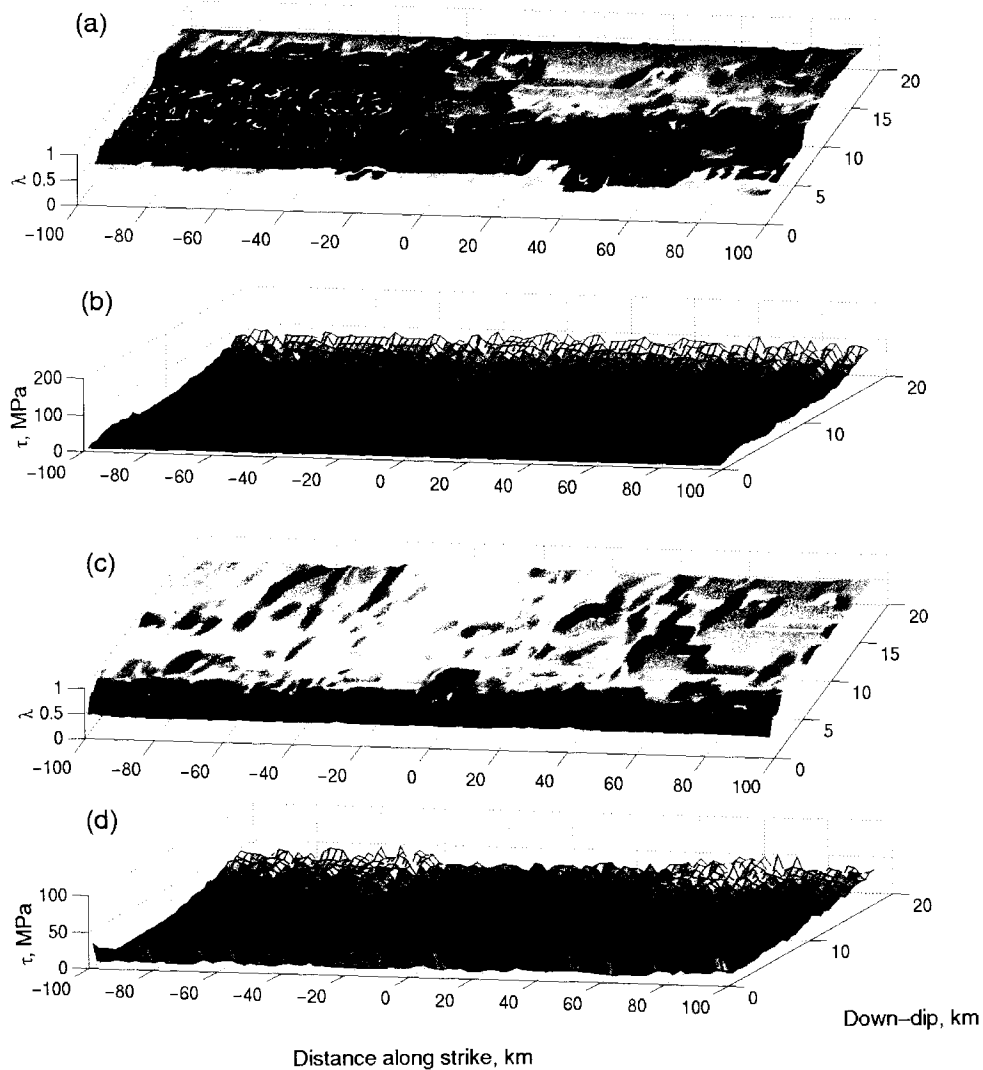


Figure 2.5: (a) Pore pressure compartments on the strike-slip fault at $t=1500$ years. The vertical axis is $\lambda = P_f/\sigma_n$. Its values range from 0.4 (e.g., at the top of the fault, referring to a hydrostatic pore pressure gradient) to values close to 0.9 (highly overpressured compartments). We note that the heterogeneity imposed in the pore pressure increase rate acts as noise superposed on significant heterogeneities due to slip and subsequent pore space creation and pore pressure redistribution. (b) Shear stress distribution on the strike-slip fault at the same time. (c) Pore pressure compartments on the dipping fault at $t=5400$ years. (d) Corresponding shear stress distribution.

the two faults is illustrated by the time evolution of their average shear stress, effective stress, and pore pressure (Figure 2.6). Each abrupt change in slope corresponds to a model earthquake. We notice the rather short onset of rupture on the strike-slip fault (bold lines) and how large events can reduce the mean shear stress but also, and to a larger extent, the mean pore pressure. Stress builds slowly on the dipping fault and no earthquakes happen before the fault is highly overpressured. After 6000 years, both faults have reached a dynamic equilibrium (e.g., pseudo-steady state). The strike-slip fault, though initially overpressured, has evolved to a strong fault (approximately hydrostatic fluid pressures and high shear stress), whereas the dipping fault has become weak. This occurs because of the connection of the strike-slip fault to the hydrostatic surface, while the (buried) dipping fault increases in pore pressure during the slow buildup of shear stresses and never hydraulically communicates with the surface. Although this particular system evolved in this manner, it should not be generalized that all shallow dipping faults are overpressured.

2.3.3 Slip Vectors During Rupture

When the stress state on a fault has organized to a point where stress transfer and poroelastic effects can sustain a propagating rupture, slip on one cell can cascade through this stress state and generate large events. Here we investigate a $M_w = 7.20$ event spontaneously generated on the subvertical strike-slip fault at around 5500 years to illustrate some of the properties of these large events. We explore the propagation of slip, the evolution of the rake angle, and the stress interaction between the two faults. Figure 2.7 shows the quasi-static propagation of slip for one rupture. The gray scale shows the cumulative slip and the arrows show the slip vector (rake angle) during the event. The updip component is shown with a vertical exaggeration of 10 since the slip vectors on the strike-slip fault are predominantly strike slip. The rupture initiates, propagates upwards throughout the whole fault width, reaches the top of the fault (Figure 2.7a) and then starts propagating laterally (Figure 2.7b). The final slip and rake angle distribution is shown on Figure 2.7f. The final slip distribution of this event shows a heterogeneous slip distribution, with a maximum slip of 7.32 m. The maximum lateral extension of the rupture is 50 km, and the maximum width is the width of the fault plane (18 km). Though the rupture initiated at $x = -82$ km, coseismic stress transfer was enough to make the rupture front jump over 20 km (see Figure 2.7b) and propagate to 50 km along strike.

We observe changes in the rake angle during rupture propagation, a common seismological observation (e.g., Bouchon et al., 1998b). Changes in the rake angle have been investigated as a potential tool for initial stress determination from ground motion records inversion (Spudich, 1992). Guatteri and Spudich (1998) give three possible factors that may lead to rake changes: (1) a low initial stress level (allowing an almost complete stress drop); (2) spatial variations in the direction of initial stress, and (3) slip in the direction of the current shear stress and not in the direction of initial shear stress during the propagation of the rupture. The two first conditions can be related. That is, low initial shear stress could result from a nearly fault-normal compression. In that case, small variations in the geometry and orientation of the fault (changes in dip angle as well as changes in strike) can lead to large variations in the direction of initial stress. In our model, the shear

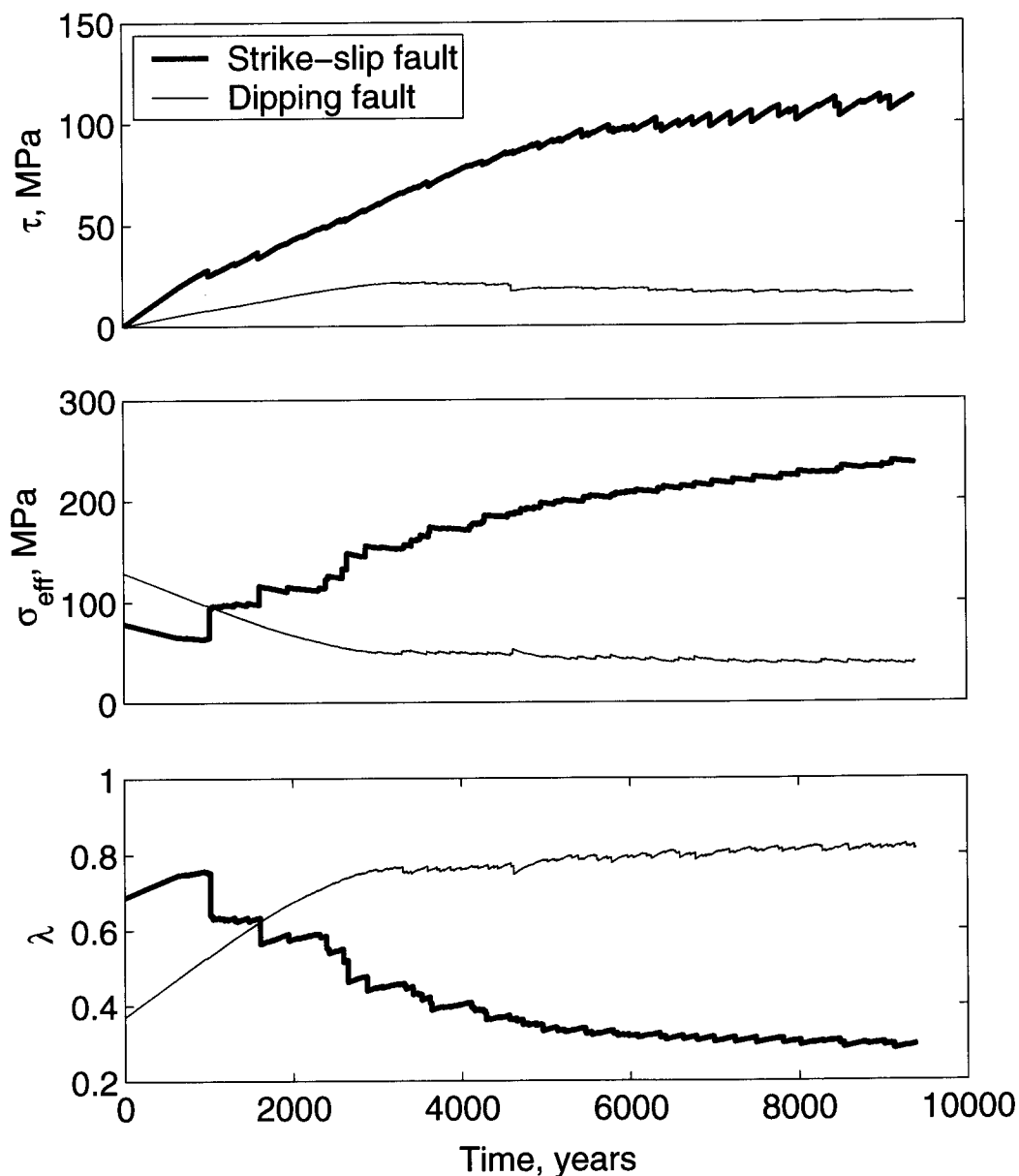


Figure 2.6: Average properties of the faults versus time. (top) Mean shear stress, (middle) Mean effective stress, (bottom) Mean pore pressure. Each abrupt change in slope corresponds to a model earthquake. We notice the rather short onset of rupture on the strike-slip fault (bold lines) and how large events can reduce the mean shear stress but also, and to a larger extent, the mean pore pressure. Stress builds slowly on the dipping fault, and no earthquakes happen before the fault is highly overpressured. After 6000 years, both faults have reached a dynamic equilibrium (pseudo-steady state).

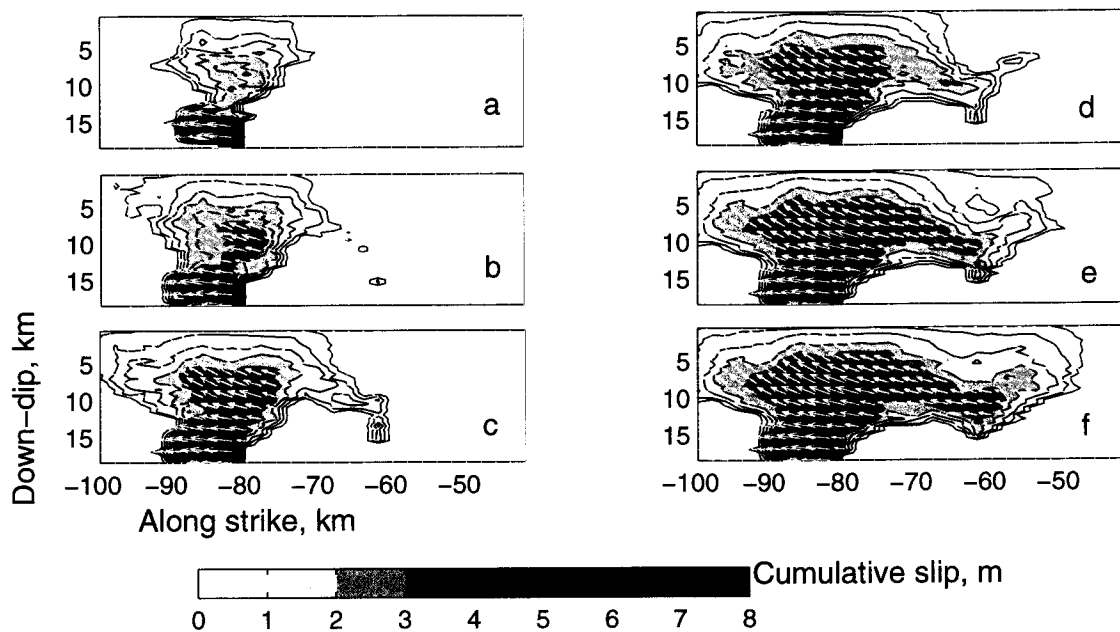


Figure 2.7: The propagation (a through f) of a large rupture ($M_w = 7.2$) occurring at $t=5541.78$ years on the strike-slip fault. The gray scale shows the cumulative slip, and the arrows show the change in the rake angle during the event (the updip component is shown with a vertical exaggeration of 10). Although the rupture initiates at $x=-82$ km, the rupture front “jumps” to $x=-60$ km and keeps on propagating. We can notice changes in the rake angle with rupture propagation. Note that the aspect ratio is not preserved.

stress distribution is initially heterogeneous (see Figure 2.5, right) due to the previous slip history only and keeps evolving as the rupture propagates. Note that slip is forced to be in the direction of the current shear stress. We observe rake changes during the (quasi-static) propagation of an event on the (planar) strike-slip fault (Figure 2.7), in a mostly strike-slip regime with a small fault-normal component. We also observe a heterogeneous distribution of the static (final) rake. The average static stress drop is 11 MPa relative to the stress state at the initiation of the event (the maximum stress drop is on the order of 70 MPa but is reached only for two cells; see more details in section 3.4). This range of values is consistent with the ones obtained for the 1995 Kobe earthquake, for which *Bouchon et al.* [1998b] obtained 10 MPa and for the 1992 Landers earthquake, for which *Bouchon et al.* [1998a] obtained a maximum static stress drop of 20 MPa. The rake angle varies between 180° and 165° , with the maximum rake angle rotation at the edges of the upper half of the patch that slipped (*Spudich's* [1992] review mentions rotations from $\pm 15^\circ$ to $\pm 50^\circ$). Finally, at the time this rupture initiates, the part of the fault that breaks may be considered weak ($\lambda \sim 0.45$), compared to the surrounding cells ($\lambda \sim 0.35$, e.g., reduced pore pressure from previous ruptures).

2.3.4 Fault Interaction: Separating the Effects of Shear Stress and Pore Pressure

Plate 1 shows the evolution of pore pressure (first column) and shear stress (second column) on the strike-slip fault (left) and on the dipping fault (right) during the same $M_w = 7.20$ event on the strike-slip fault described in section 2.3.3. Each subplot corresponds to cumulative changes of either pore pressure or shear stress (cumulative stress drop distributions) with respect to their state when the event initiated (not absolute values). Since the propagation is calculated in a quasi-static manner, we show snapshots of the pore pressure and shear stress state at different steps in the computer calculation for $t=5541.78$ years, and not at different “times.” There were 194 cycles through the “rupture propagation” loop. The frames show row by row respectively the first, the twentieth, the sixtieth, the hundredth, the 193rd and the 194th (and last) iteration. Changes in pore pressure are due both to poroelasticity (and hence to the stress transfer during the rupture propagation) and to the redistribution of pore pressure itself.

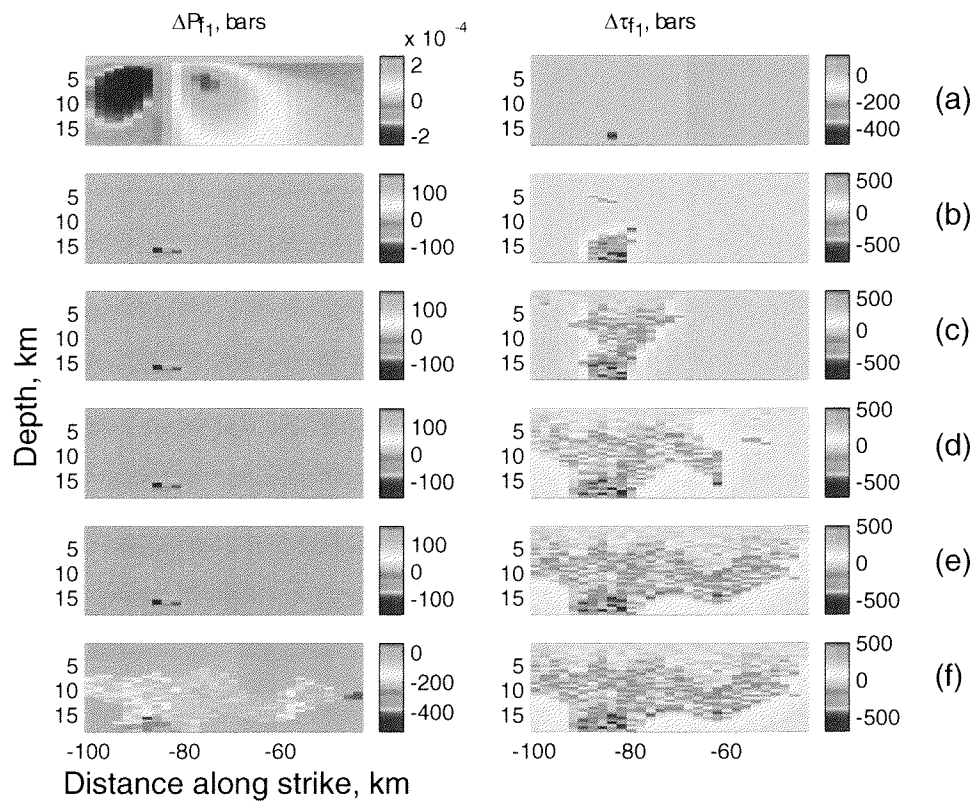


Figure 2.8: Plate 1(a to f): Fault interaction. Pore pressure changes (first and third columns) and shear stress changes (second and fourth columns) on the strike-slip fault during the $M_w = 7.2$ event on the strike-slip fault. Changes in pore pressure are due both to poroelasticity (and hence to stress transfer during the rupture propagation) and to the redistribution of pore pressure itself. Changes in shear stress are due to the assumed stress drop and to the redistribution of stresses. Note different color bars for P_f for the two faults.

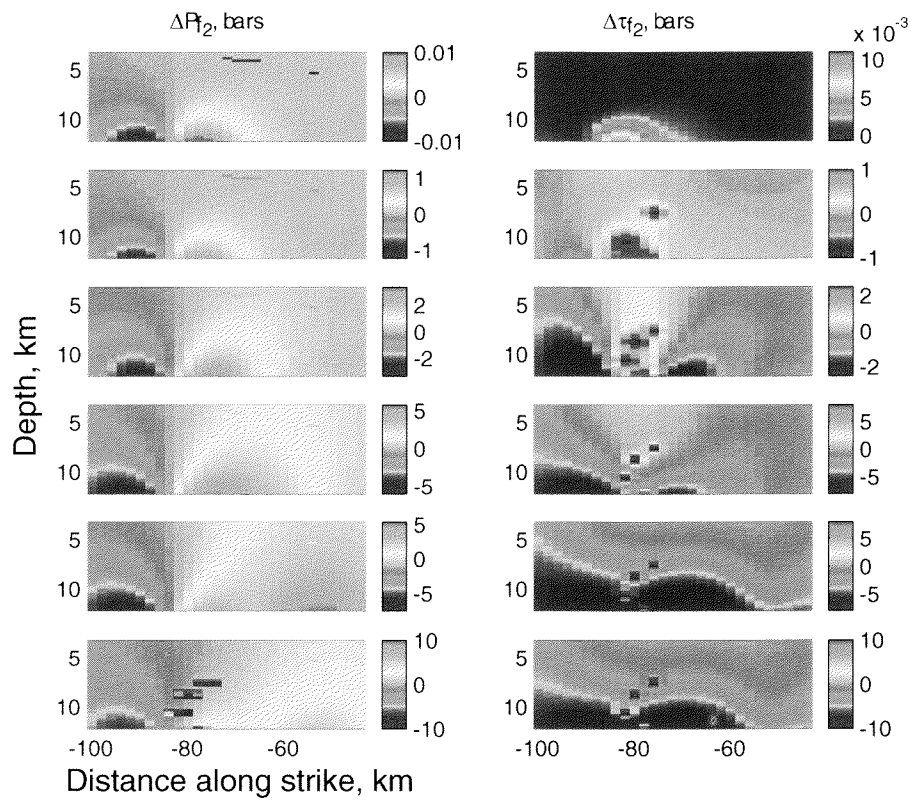


Figure 2.9: Plate 1(a to f): Fault interaction. Pore pressure changes (first and third columns) and shear stress changes (second and fourth columns) on the dipping fault (respectively) during the $M_w = 7.2$ event on the strike-slip fault. Changes in pore pressure are due both to poroelasticity (and hence to stress transfer during the rupture propagation) and to the redistribution of pore pressure itself. Changes in shear stress are due to the assumed stress drop and to the redistribution of stresses. Note different color bars for P_f for the two faults.

On Plate 1a (top) we see that within the first cycle, only one cell failed on the strike-slip fault (second column). The stress drop on this cell (-40 MPa) loads (through stress transfer) the other cells in the fault system. The first frame shows the poroelastic effect on the strike-slip fault due to the stress redistribution after this failure. ΔP_{f_1} is very small ($\pm 2 \times 10^{-5}$ MPa) compared to the same effect on the dipping fault shown on the third column ($\Delta P_{f_2} = \pm 2 \times 10^{-3}$ MPa). We also notice a small increase in shear stress (fourth column, $\Delta \tau_{f_1} = \pm 2 \times 10^{-5}$ MPa) 1 order of magnitude smaller than the change in pore pressure. Both changes on the dipping fault are located in the part of the fault closest to the strike-slip fault (≈ 10 km) and are maximum at 12.25 km depth, centered on $x \approx -82$ km, like the strike-slip initial failure.

Plate 1b shows the state on the two faults after 20 iterations. The first frame shows the redistribution of pore pressure to the neighboring cells of the first failed cell. This plot is in full scale. The magnitude of the fluid pressure changes due to the opening of the seals is much larger than the poroelastic effect and mask it. As pointed out in section 2.2.2, this redistribution was enough to initiate failure in some of the surrounding cells and the code cycles again in the stress transfer loop (second frame). The third frame shows the increase of the poroelastic effect ($\Delta P_{f_2} = \pm 0.1$ MPa) and the fourth frame shows the shear stress changes both from stress transfer from the strike-slip fault and from the two triggered failures on the dipping fault itself. Because the order of magnitude of the local stress transfer is much greater than the one of the interfault transfer, we chose to use a saturated scale on all the subplots of the right most column (except the first row). The absolute values of $\Delta \tau_{f_2}$ are in the range ± 2 MPa. The next three rows (Plates 1c, 1d and 1e) show the propagation of the strike-slip rupture and the newly triggered failures on the dipping fault. Plate 1f, corresponding to the last cycle, shows the final redistribution of stresses and pore pressure on both faults. In order to show the final poroelastic effect on the pore pressure state of the dipping fault, again, we used a saturated scale. The absolute values of ΔP_{f_2} are in the range ± 1 MPa.

Poroelasticity has a larger effect on the dipping fault than on the strike-slip fault itself (see changes in the color bar), and on both faults, pore pressure redistribution is much more efficient than poroelasticity in changing the effective normal stress. Changes in shear stress are due to the assumed stress drop and to the redistribution of stresses. Notice in Plate 1, third and fourth columns, that some small failures are triggered on the dipping fault by the one propagating on the strike-slip fault in regions of increased pore pressure and increased shear stress but not in regions of increased shear stress and decreased pore pressure. As these cells fail, the magnitude of pore pressure change is about double than for shear stress at any cycle (1-0.5 for the twentieth cycle, 2-1 for the sixtieth, 5-3 for the hundredth, ...). The faults therefore interact, and in this example, a large event on the strike-slip fault triggered a $M_w = 5.00$ event on the dipping fault. Also notice that a large part of the dipping fault nearest the part of the strike-slip fault that ruptured is brought further from failure at the end of the event.

Table 2.2 demonstrates the efficiency of fault interaction: the coseismic triggering of seismicity on one fault due to the propagation of a rupture on the other fault. The time, the moment magnitude of the triggering event, and the moment magnitude of the triggered event on the receiver fault are given. We chose to show only the coupled triggering-triggered events including at least one event of moment magnitude M_w greater than 6.9.

Time (years)	Triggering Event	Triggered Event
2137.7	M1= 7.00	M2= 4.60
2873.7	M1= 7.10	M2= 4.75
3300.1	M2= 7.00	M1= 5.00
3622.8	M1= 7.10	M2= 5.10
3639.9	M1= 7.35	M2= 4.70
3870.4	M2= 7.00	M1= 4.35
4148.0	M1= 7.10	M2= 4.90
4252.5	M1= 6.95	M2= 5.35
4286.1	M1= 7.30	M2= 6.00
4560.6	M1= 7.11	M2= 5.15
(4585.5)	M1= 5.10	M2= 7.10)
4618.0	M2= 7.45	M1= 5.75
4718.1	M1= 7.00	M2= 4.50
4939.7	M1= 7.00	M2= 4.80
5129.2	M1= 7.10	M2= 5.10
5225.3	M1= 7.10	M2= 4.50
5541.8	M1= 7.20	M2= 5.00
5601.1	M2= 7.00	M1= 4.05
5788.8	M1= 7.50	M2= 5.00
5801.4	M1= 6.90	M2= 4.90
5843.4	M1= 7.40	M2= 6.00
5908.0	M1= 7.00	M2= 4.30
5972.6	M1= 7.25	M2= 5.50
6012.8	M1= 7.05	M2= 5.10
6082.7	M1= 7.50	M2= 5.05
6190.9	M2= 6.90	M1= 4.10
6411.9	M1= 7.50	M2= 5.00
6613.9	M1= 7.10	M2= 4.90
6621.6	M1= 7.40	M2= 5.05
6773.6	M2= 7.10	M1= 5.00
6988.1	M1= 7.70	M2= 4.70
7929.7	M1= 7.20	M2= 4.60
8172.1	M1= 7.00	M2= 4.65
8476.8	M1= 7.60	M2= 4.20
8528.7	M1= 7.70	M2= 4.35
8786.4	M1= 7.15	M2= 4.30
8828.3	M1= 7.20	M2= 4.05

Table 2.2: Coseismic stress triggering between the two faults. M1 and M2 refer to the moment magnitude (M_w) of strike-slip fault and dipping fault events, respectively, and are calculated from the scalar seismic moment M_0 via equation (2.6). The triggering event is always the larger of the two, except at $t=4585.5$ years, see row in parentheses.

In all the cases but one the triggering events are large events ($6.9 < M_w < 7.8$) and the magnitude of the triggered events range from 4.03 to 5.97. The exception (in parentheses in Table 2.2) occurs at $t=4585.5$ years, when a $M_w = 5$ strike-slip event triggered a $M_w = 7.11$ on the dipping fault. Within the 9300 years of simulation, 63 earthquakes show $M_w > 6.9$ on the strike-slip fault. Only 30 of them trigger another earthquake coseismically. The proportion is the same for the dipping fault: 16 events with $M_w > 6.9$ among which only 7 related to an event on the strike-slip fault during the same time step. In principle, then, the strike-slip event could trigger a large event on the dipping fault (or vice versa) if the critical stress state on the receiver fault is sufficiently organized to support a spontaneous rupture. In this simulation the largest triggered event is a $M_w = 5.97$, except a $M_w = 5.07$ event that started on the strike-slip fault triggered coseismically a $M_w = 7.11$ on the dipping fault ($t=4585$ years), see Table 2.2.

2.3.5 Total Local Stress Direct Calculation

The orientation and magnitude of the principal components of regional stress tensor are essential for understanding the physics of faulting, for evaluating the role of crustal fluids in the rupture process, and for seismic hazard assessment through the calculation of the optimal orientation of fault planes and expected tectonic regimes (e.g., Δ CFS Nalbant et al., 1998; Stein et al., 1997). However, as pointed out by Zoback (1992) and Scholz (2000), reliable direct in situ stress measurements (Zoback and Healy, 1992; Townend and Zoback, 2000) or evaluation (e.g., by inversion of focal mechanisms Hardebeck and Hauks-son, 1999) are not straightforward. The regional stress is defined as a far-field tectonic load with respect to faults of interest. Accurate measurements are difficult because they should be made far from active faults to avoid fault-induced perturbations and also far from folds to avoid local perturbations of the regional stress. Because our model monitors the complete stress tensor in the whole fault system (on and off fault), we can calculate the principal stresses along any profile, at any depth, and for different times. We can therefore quantify stress partitioning (e.g., different tectonic regimes near the thrust fault compared to close to the strike-slip fault) and the rotation of the maximum horizontal stress near the plate boundary and study its relation with the seismic slip recorded at that time during the simulation. In this preliminary study the “local” stress tensor was calculated on a horizontal grid at 8.5 km depth and at $t=9300$ years. The area that we investigate has the length of the faults and a width (y axis) about twice the depth of the dislocation plane on which the basal plate motion is applied. The strain tensor is computed as the superposition of displacements from plate motion and the cumulative slip displacement on the two faults in the geographical reference frame. We can determine the corresponding stress tensor through Hooke’s law and then distribute the lithostatic stress calculated at the given depth to the isotropic part of the tensor. We then calculate the eigenvalues and eigenvectors of the stress field. In the absence of slippage on the faults, at a given depth, the stress orientation shows a small gradual change from about -48° near the plate boundary to a constant value about -55° for $y \geq 35$ km (a distance from the plate boundary twice as large as the depth of the basal dislocation plane). This angle reflects the small normal component of the plate velocity vector (almost pure shear configuration, plus a small compressive component). The ratio $R = (\sigma_2 - \sigma_3)/(\sigma_1 - \sigma_3)$ is

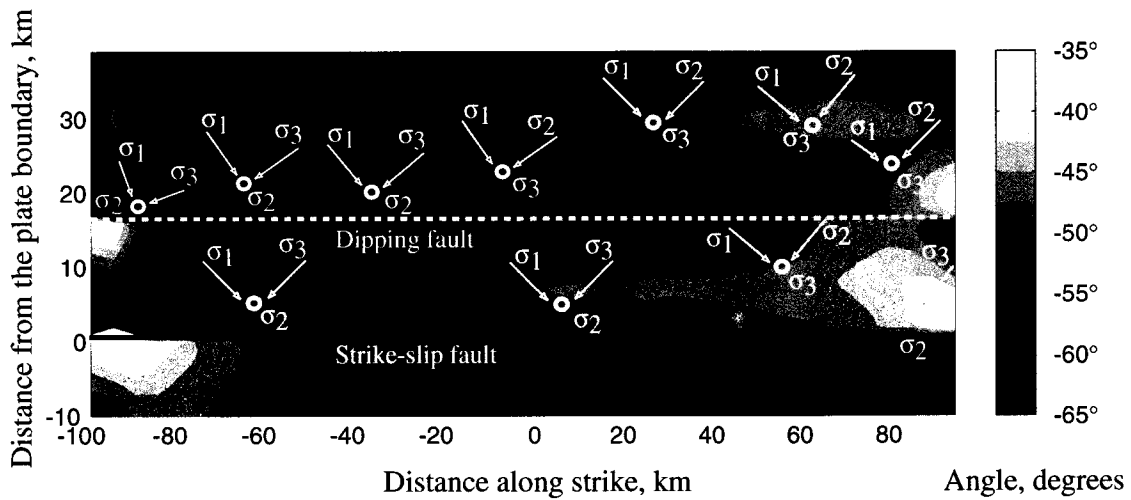


Figure 2.10: Local stress. Principal components are on a horizontal plane at 8.5 km depth for $t=9300$ years. The gray scale shows the angle of σ_1 with respect to the strike of the faults. The arrows show the directions of the principal stresses. Note that σ_2 is mostly vertical but that σ_3 can also be the vertical stress, denoting a transpressional regime.

~ 0.5 , and σ_2 is vertical, corresponding to a strike-slip regime, with an optimal orientation for slip of about -18° .

Figure 2.8 shows the angle between the horizontal component of the maximum principal stress σ_1 and the strike of the faults, calculated after 9300 years of simulation, and including the cumulative fault slip. The directions of the three principal stresses are represented at several locations with arrows for the horizontal stresses and circles for the vertical ones. The orientation of σ_1 varies between -65° (locally -70°) and -35° . The two extreme values are confined to small areas, whereas in most of the region the angle is in the range $[-45^\circ, -58^\circ]$. Other noticeable features include two regions where σ_3 is vertical, leading to a compressive plus strike-slip optimal tectonic regime. One of these zones extends roughly between -20 and 100 km along x and 25 and 35 km along y , and the other one, much smaller, lies at $x \geq 40$ km and $10 \leq y \leq 15$ km. They are just below and just above the dipping fault, respectively, in an x interval corresponding to the last large earthquake on the dipping fault. Just to illustrate how much an earthquake can rotate the surrounding stress field, we consider two examples. The $M_w = 7.2$ strike-slip event that was studied in the other sections induced rotations of σ_1 of $\pm 3^\circ$, whereas an earthquake of the same magnitude on the dipping fault ($t=6246$ years) induced rotations of $\pm 5^\circ$, for both cases, mostly in a region $y = \pm 5$ km from the intersection of the fault with the horizontal plane.

Notice that our chosen fault system was not optimally oriented, so large slip deficit accumulated as long times were needed for the initial failure on the both faults (especially the dipping fault). The seismicity on the dipping fault could start only when the pore pressure was high enough to considerably reduce the Coulomb failure stress. By calculating R and knowing which principal stress is vertical, maps of the optimal tectonic regimes

as well as a map of the corresponding planes (dip and strike) optimally oriented for failure in the country rock can be obtained. This result points to the necessity of generating new faults in response to the evolving stress field, and this is currently being developed.

2.3.6 Map and Cross Sections of Δ CFS and Comparison with Seismicity Distribution

Major simplifications of current stress transfer models are the assumptions (1) that the total slip from an earthquake can be averaged across a dislocation surface, and (2) the pore pressure state is homogeneous and its effect on the effective stress can be described through an apparent friction coefficient (μ'). The average slip is then used to calculate Δ CFS at a particular depth along faults of a prescribed orientation, typically vertical strike-slip faults. This simplification restricts the evaluation of along-strike changes in Δ CFS because the complex slip at depth is smoothed out. An alternative approach is to use seismic and geodetic techniques to evaluate more complex slip distributions, which can then be used as input to a stress transfer code. This approach is useful but requires extensive studies of a particular earthquake in a specified region, does not consider heterogeneous pore pressure distributions, and must always be “after the fact.” The approach pursued here is to build a forward model that captures the dominant physics of the earthquake process, and then to use the model to evaluate spontaneous ruptures from a variety of fault geometries to systematically investigate the Δ CFS phenomenon, both on prescribed faults where pore pressure and stresses are monitored and on optimally oriented faults. In the latter case, the regional stress (orientation and magnitude of the principal stresses) is calculated directly from plate motion and the slip history of the fault system. We used the slip distribution in Figure 2.7 as input to a simple stress transfer code and show Δ CFS resolved on vertical optimally oriented faults as well as on the two prescribed faults of our model.

In the former case, we consider a simplified regional stress with σ_1 much larger than the two other components, with the magnitude and direction determined by the model at that time: 200 MPa, oriented -40deg to the plate boundary. The stress difference ($(\sigma_1 - \sigma_3)/2$) is between 50 and 100 MPa. These high values are, of course, unrealistic and demonstrate why future models must allow for the creation of new faults in response to the regional stress field. The apparent friction coefficient μ' is chosen as 0.5. The calculation was performed for a depth of 8.5 km, and the intersection of the horizontal plane with the faults lies at $y=0.7$ km for the strike-slip and at $y=15.5$ km for the dipping fault. For the case of vertical planes, the optimal orientation (see lines on Plate 2) spans a small range of angles, from [-10.2,-6.3] degrees to the strike of the faults within ± 5 km from the strike-slip fault to [-8.7,-8.2] (the “far-field” value, due only to the regional stress for $\mu' = 0.5$ is 8.3). These rotations are small because the calculated regional stress is much larger than the stress perturbation due to the earthquake (see Plate 1 and discussion by King et al., 1994). As discussed in section 3.5, this high regional stress (a usual value in CFS studies is 100 bars) is due to the high strain energy stored in the country rock near the boundary, a direct consequence of both the choice of a uniform plate motion vector all over the basal dislocation (~ 40 km) and the orientation (nonoptimal) of the prescribed faults. On the optimally oriented vertical planes, Δ CFS was calculated and

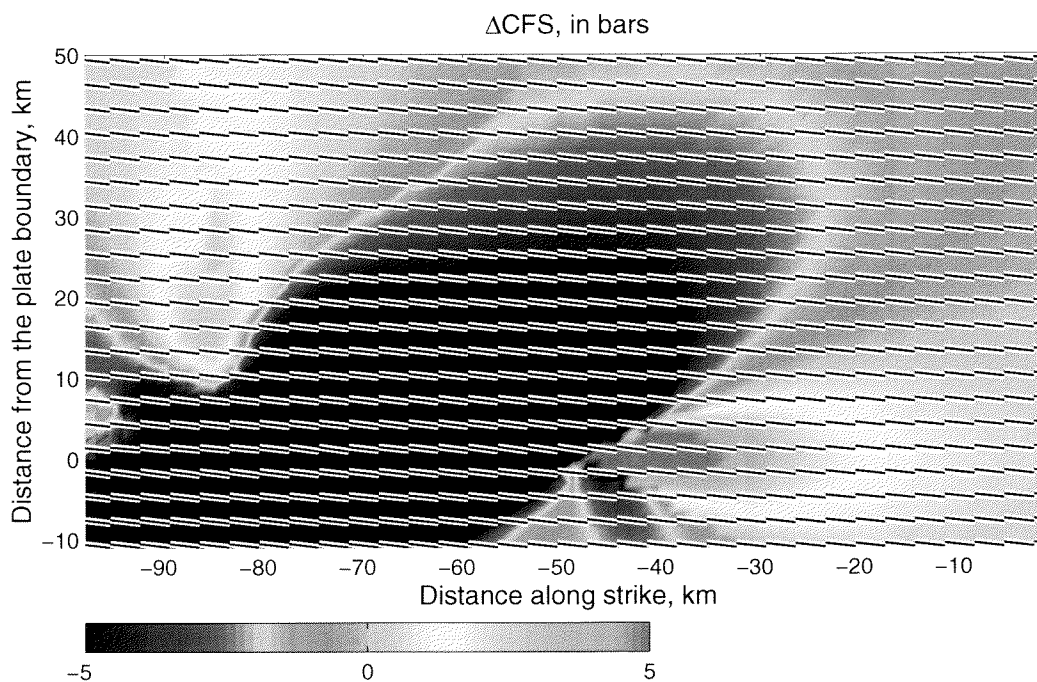
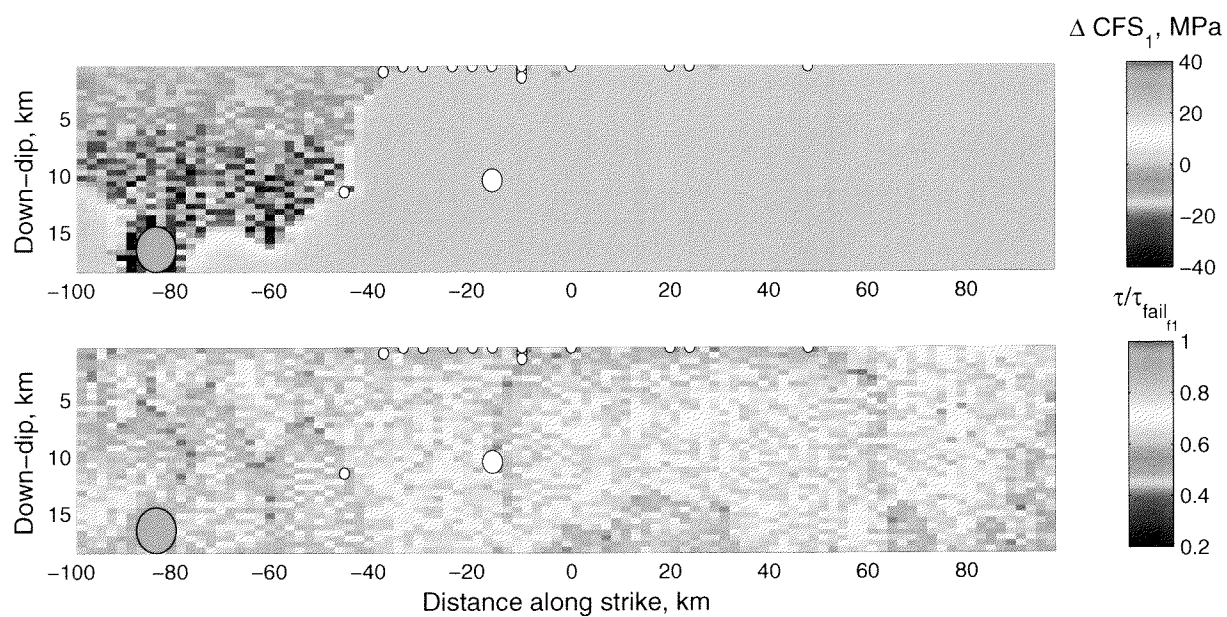


Figure 2.11: Plate 2. Static changes in Coulomb failure stress on optimally oriented vertical planes at 8.5 km depth after the same $M_w = 7.2$ event on the strike-slip fault: map view, with $\mu' = 0.5$, $\sigma_1 = 200$ MPa, oriented -50° to the strike of the faults

Plate 2 shows a large stress-released area, as well as two small areas that were brought closer to the failure. This pattern corresponds to that expected for right-lateral strike-slip events (King et al., 1994). Plate 3 shows the superposition of the change in coulomb failure stress with subsequent seismicity (next 20 years) on fault 1 (Plate 3a, top) and on fault 2 (Plate 3b, top), as well as the initial proximity to failure on the two faults at $t=5541.78$ years (Plates 3a and 3b, bottom). For these faults, ΔCFS was calculated using model results of shear stress, normal stress, and pore pressure, with a static friction coefficient of 0.6. On the strike-slip fault we note that all 15 events (magnitudes from 4.06 to 5.09) occurred in areas that were brought closer to failure (ΔCFS from +1 bar to +100 bars), which is consistent with the static stress transfer approach. No events initiated in the zone of high positive ΔCFS between $x=-40$ and -20 km because the stress state on the strike-slip fault prior to the rupture was far from the Coulomb failure stress ($\tau/\tau_{\text{fail}} < 0.8$). This corresponds to the stress drop due to a previous event, see Plate 3b. On the dipping fault the distribution of the 43 hypocenters does not look related to the ΔCFS pattern but to the areas that were already close to the failure before the triggering event. However, no earthquake occurred in the area of largest decrease in CFS, even if this area was very close to failure (Plate 3b, bottom, $\tau/\tau_{\text{fail}} \geq 0.8$) prior to the triggering event. In this case, the stress transfer from the first event induced a delay. Although the positive values of ΔCFS are rather small (commonly ≤ 1 bar), the number of earthquakes generated within the 20 years following the event is greater on the dipping fault than on

(a)



(b)

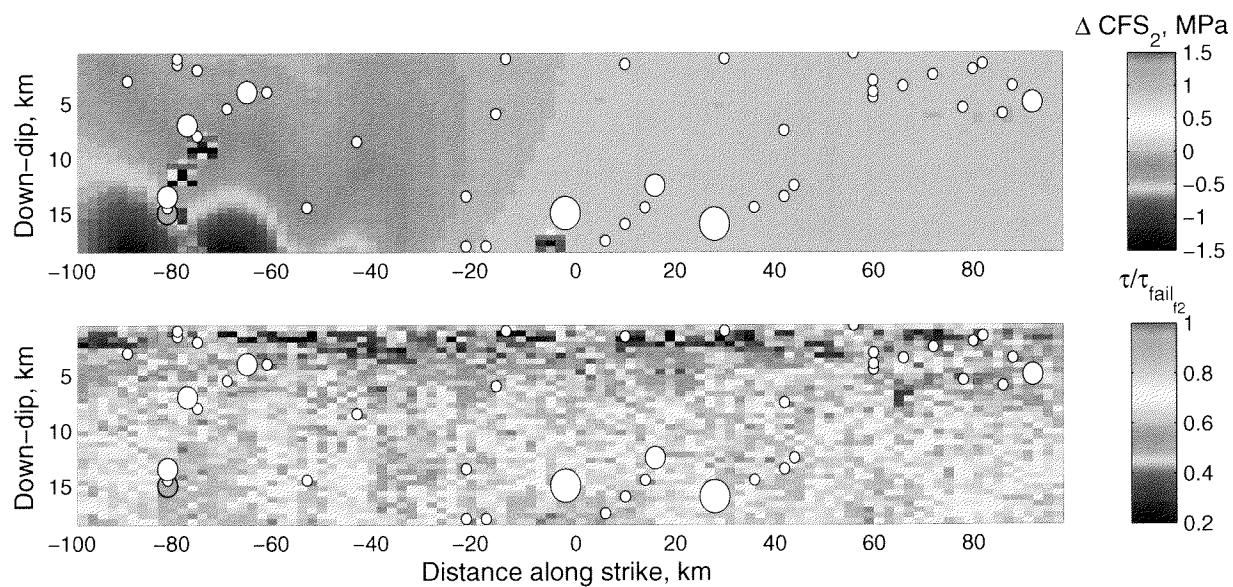


Figure 2.12: Plate 3. Static changes in Coulomb failure stress and initial proximity to failure (τ/τ_{fail}) (a) on the strike-slip fault, and (b) on the dipping fault, with hypocenter distribution for the next 20 years of simulated seismicity.

the strike-slip fault. This is related to the difference in the stress state on the two faults at the initiation of the rupture at $t=5541.78$ years.

A direct comparison of the match between Δ CFS maps or cross sections and seismicity is now possible, allowing for a detailed investigation of the importance of a precise regional stress tensor and of an actual pore pressure distribution by opposition to an assumed apparent friction coefficient. The existence (or not) of a threshold value (i.e., above which an increase in CFS will promote seismicity whatever initial stress state is on the faults (Ziv and Rubin, 2000)) can also be investigated.

2.4 Discussion and Conclusions

2.4.1 Key Features of the Model

We have constructed a simple forward three-dimensional fault interaction model, driven by plate motion and pore pressure that includes dislocation theory, poroelasticity in undrained conditions, mechanisms for pore space reduction, small-scale coseismic changes in hydraulic properties, and frictional dilatation. We monitor the full stress tensor in any location in the elastic half-space and pore pressure on both faults. Reasonable assumptions are made about the initial heterogeneity. Cells which have a comparatively high pore pressure increase rate prove to be more often hypocenters. However, there is no direct link between this rate and the size of the events; that is, even if failures initiate more often in these cells, they propagate only if the surrounding cells are critically stressed. Preliminary results of this fully forward model show a complex evolutionary stress state in our fault system as well as a nonperiodic seismicity catalog that follows the GR law. Ruptures exhibit complex slip distributions, and the rake angle changes dynamically during the propagation of a rupture. Interaction between the faults is observed from coseismic shear stress changes as well as pore pressure changes on the dipping fault during large ruptures on the strike-slip fault. The result is small triggered events on the dipping fault. A simple static stress transfer model shows a good correlation between zones of positive change in Coulomb failure stress and subsequent hypocenter distribution, also showing the importance of the initial stress distribution on the induced seismicity.

2.4.2 Advantages of the Model

The model provides a general framework to study the behavior of large-scale transpressional and transtensional systems (such as the San Andreas fault; the North Anatolia fault, and the Dead Sea Transform). It can be used to study the stress state evolution to determine the relative contribution of plate motion loading and pore pressure changes, and spatiotemporal rotations of the principal axes of the “regional” stress tensor that combines plate motion, slip along faults, and the overburden.

The model can also be used as a tool to study conditions for rake angle changes during rupture on a fault. A thorough analysis of the influence of the fault geometry (e.g., local changes in dip angle), of the initial stress distribution, and of the regional stress (e.g., changes in the amount of normal stress) can be carried out.

The model can be used to study multiple fault interaction to determine some controlling factors. We show the competing poroelastic effect and shear stress transfer (Plate 1, third and fourth columns) can trigger events only in zones of increase in shear stress and increase in pore pressure. The poroelastic increase in P_f is also larger than the change in shear stress by a factor of 2 in this example (when failures happen on the receiver fault). However, a study of the entire synthetic catalog is needed to discriminate between these two phenomena.

It is also interesting to note that pore pressures sometimes exceed the minimum principal stress at shallow depth during the pore pressure redistribution phase. This could induce some hydrofracture-related damage in, and normal to, the fault zone providing another complexity to the hydraulics of the system.

2.4.3 Limitations of the Model

The model can be used to investigate a wide range of phenomena. However, some important processes have not been addressed and need to be considered. First, diffusion processes are ignored. Using a simple one-dimensional diffusion equation (equation (2.7)):

$$\frac{\partial P_f}{\partial t} = \frac{k}{\eta\beta} \frac{\partial^2 P_f}{\partial x^2}, \quad (2.7)$$

where k is the permeability, η is the viscosity and β is the total compressibility, we find that if k_{rupture} is of the order of 10^{-15} m^2 (for a viscosity about $1.9 \times 10^{-4} \text{ Pa s}$ and a maximum pressure gradient from lithostatic to hydrostatic), the time necessary to equilibrate fluid pressure over a cell size (km-scale) is of the order of, or less, than the average time step (days). Since fluid pressures are redistributed at the end of an event, the error due to the permeability switch is not significant. For larger events, pore pressures are redistributed each time stress equilibrium is reached, but this redistribution may induce a subsequent propagation of the event. In this case, pore pressures should not be redistributed instantaneously, especially over large patches. A more realistic model should include pore pressure diffusion and not redistribution.

Second, frictional heating and the subsequent increase in pore pressure probably play an important role in fault zones and will be introduced into the model. Lachenbruch and Sass (1980), Mase and Smith (1985) and Spray (1995) show that temperatures can reach 1000 degC during high-speed slip experiments performed on Westerly granite. Such large temperature changes can expand pore fluids, can initiate melting and dehydration reactions, and can provide a mechanism for afterslip. Presumably, the frictional heating is not generated uniformly over the fault surface but is more likely to be localized at asperity contacts, which may provide an additional source of complexity along the faults. An interseismic temperature depth profile should also be introduced because of the influence of temperature on the kinetics of geochemical reactions and hence on the fluid content (Quattrocchi, 1999). The latter modification might also be efficiently coupled to a more realistic $\dot{\Gamma}$ in the source term. A full study of heat transfer in a saturated porous medium should take into account the rate of conductive heat transport, the rate of convective transport, the rate of heating due to the reversible work done on the fluid, the rate of frictional heating, and the rate of internal heat storage for the solid-fluid composite (Mase

and Smith, 1985). This can be solved numerically but introduces many unconstrained parameters. Our general model framework can be used to investigate these processes but it is beyond the scope of the current work.

Third, all events in the model are “seismic”, meaning that we implicitly assume unstable sliding at the onset of failure. Segall and Rice (1995) showed that high pore pressures affect the stability of sliding, and such a criterion should be considered in future models. This stability criterion (Segall and Rice, 1995) depends on the elastic properties of the surrounding country rock and on the pore pressures in the fault zone. Sliding stability affects the rate of stress accumulation on the faults, and at a microscopic scale, it induces compaction as already discussed (Sleep and Blanpied, 1994). Finally, a uniform plate motion, even near the plate boundary, is a rough approximation that leads to high depth-dependent stress concentrations near the boundary.

2.4.4 Conclusion and Future Perspectives

This simple coupled system (i.e., a dipping fault and a subvertical strike-slip fault, in a transpressional environment) was chosen as a starting point because there are such examples in nature and because it was a way to investigate a fully three-dimensional fault system, including fault interaction, stress triggering and local stress field time evolution. This a priori choice of geometry allowed us to draw several conclusions. The most important is that it is essential for any forward model to include the dynamic generation of new faults in response to the evolving stress field, e.g., the initial nonoptimal orientation of the faults leads to a high strain energy in the system, an overpressured dipping fault, a high slip deficit and high maximum principal stresses in the surrounding country rock. The nonoptimal orientation of our system thus limits the generalization we can make. Nevertheless, we were able to show seismicity statistics in conformity with both theoretical and data-based results, realistic rupture propagation patterns, including changes in the rake angle, as well as the critical influence of fault zone fluids on the triggering of earthquakes from one fault to the other, via poroelastic effects (see section 2.3.4 as well as the self-organization of the stress state of the faults Miller et al., 1999). Future work will include two main aspects: the model development toward the evolution of fault systems following the evolution of the principal stresses (dynamical fault generation), and a closer analysis of the “source terms” (fluid sources, compaction, damages, hydrofractures). Our long-term aim is to point to measurable properties (e.g., pore pressures, hydrofractures, seismicity catalogs of the area) in or around (e.g., stress orientation, surface strain, triggering) fault zones, which may allow inferences on the stress state of a given fault system.

Acknowledgements The authors thank Mike Blanpied and Keith Evans for insightful discussions and Igor Zacharov for his help in the optimization of the computer code. Constructive reviews of the manuscript by T. Yamashita, Mike Blanpied, and Michel Bouchon are gratefully acknowledged. This research was supported by the Swiss National Fund, program

2100-054121.98/1.

Seite Leer /
Blank leaf

Chapter 3

Fault compaction and overpressured faults: Results from a 3D model of a ductile fault zone.

This Chapter is a paper that was submitted to Geophysical Journal International, 2002.

The deformation of fault zones is observed to be a time-dependent phenomenon, that depends both on shear stress and effective confining stress, and on temperature, strain-rate, fluid content, etc. Sleep and Blanpied (1992) review evidence of slow creep during interseismic periods by pressure solution fibers, preferred crystallographic orientations and mineral reactions, while high strain rate fractures, frictional melts and explosion breccia indicate earthquake failure.

Microstructures obtained from high strain, rotary shear experiments on experimental faults containing brine-saturated mixtures of halite and kaolinite (simulated gouge) strongly resemble natural mylonites (Bos et al., 2000). This suggests that deformation of the gouge involved sliding along kaolinite-rich foliation planes, accommodated by pressure solution and dilatation/cataclasis, the relative amounts of which varied with sliding velocity. If similar behavior occurs in natural phyllosilicate-rich fault zones, such zones are expected to be significantly weaker than predicted by traditional brittle-ductile strength envelopes. Overpressured fluid pockets contained within the fault are purported another source of weakening and can cause fault creep (Faulkner and Rutter, 2001). Different rheologies could account for such time-dependent processes. The 1-dimensional shear creep and ductile compaction model of Sleep and Blanpied (1992) is extended to 3 dimensions, and the behavior of a vertical strike-slip fault is analysed in detail. Fault properties are explored and a model of a visco-elastic fault zone is incorporated into the model described in Chapter 2. The objective is to better constrain pore pressure increase mechanisms and fault zone hydraulics.

Abstract

A model of a ductile fault zone is incorporated into a forward 3-D earthquake model to better constrain fault zone hydraulics. The conceptual framework of the model fault zone was chosen such that two distinct parts are recognized. The fault core, characterized by a relatively low permeability, is composed of a coseismic fault surface embedded in a visco-elastic volume that can creep and compact. The fault core is surrounded by, and mostly sealed from, a high permeability damaged zone. The model fault properties correspond explicitly to those of the coseismic fault core. Porosity and pore pressure evolve to account for the viscous compaction of the fault core, while stresses evolve in response to the applied tectonic loading and to shear creep of the fault itself. A small diffusive leakage is allowed out of the fault zone. Coseismically, porosity is created to account for frictional dilatancy. We show in the case of a 3-D fault model with no in-plane flow that unless the fluid compressibility depends on pore pressure (and temperature), pore pressures do not drop to hydrostatic levels after a seismic rupture, leading to an overpressured weak fault. Since pore pressure plays a key role in the fault behavior, we investigate coseismic hydraulic property changes. In the full 3-D model, pore pressures vary instantaneously by poroelastic effect during the propagation of the rupture. Once the stress state stabilizes, pore pressures are incrementally redistributed in the failed patch. We show that the significant effect of pressure-dependent fluid compressibility in the no in-plane flow case then becomes a secondary effect when the other spatial dimensions are considered because in-plane flow with a near-lithostatically pressured neighborhood equilibrates at a pressure much higher than hydrostatic levels, forming persistent high pressure fluid compartments. These results suggest that significant leakage perpendicular to the fault strike (in case of a young fault), or cracks hydraulically linking the fault core to the damaged zone (for a mature fault) are probable mechanisms for keeping the faults strong and play a significant role in modulating fault pore pressures. Therefore fault-normal hydraulic properties of fault zones should be a future focus of field and numerical experiments.

3.1 Introduction

The critical role of fluids in the behavior of the fault systems requires that the fault zone hydraulics be realistically modeled. The objective of this work is to incorporate field- and laboratory-based observations (e.g., architecture, rheology, etc) into a physics-based 3-dimensional forward earthquake generation model (Fitzenz and Miller, 2001, referred to here as FM01).

Sibson (1992) was the first to advocate complex interactions between stress cycling, the creation and destruction of permeability, and fluid-flow; assuming the rapid re-sealing of the earthquake-related fault permeability increase. Blanpied et al. (1992) developed the idea of rapid sealing with shear-induced compaction (and subsequent pore pressure increase) as an instability mechanism for earthquakes, while Rice (1992) proposed the existence of deep fluid sources to maintain high pore pressures in fault zones.

Following these conceptual models that account for the influence of fluids in faulting, numerous laboratory investigations focussed on the behavior of simulated fault gouge.

Studies of the effects of slip, slip rate, and shear heating on the friction of granite (Blanpied et al., 1998) showed an influence of fluids on fault stability at high strain rates (e.g., the competition between velocity strengthening and velocity weakening due to thermal pressurization of a poorly drained pore fluid). Zhang et al. (2001) tested the anisotropic alignment of clay shape fabrics as a candidate for focusing fluid flow along fault zones and for maintaining high pore pressures in clay rich rocks. Adding to the debate, they show that fabric anisotropy alone is not enough to cause focused fluid flow along natural fault zones.

Studies on core samples and downhole measurements from drilling through the Nojima fault (Japan) one year after the Kobe earthquake (1995) yielded new insight in the fault zone structure and hydraulic processes and time-scales (Tanaka et al., 2001, e.g., Open-File Report 00-29). Pre and co- seismic magnetotelluric surveys in the North Anatolian Fault system (Izmit earthquake, 1999) allowed inferences on the link between fluid content and fault strength (Honkura et al., 2000). A strong zone in the hypocentral area of the Izmit (1999, Turkey) earthquake is characterized by a high resistivity zone. New theoretical developments derived from field observations (San Gabriel Fault) provided insight into the kinetics of crack-sealing, intergranular pressure solution, and compaction around active faults (Renard et al., 2000; Gratier et al., in press). The kinetics of crack sealing is shown to mainly control the fluid pressure and fluid flux changes on the faults. Zones of high pressures are predicted, due to fluid inflow from depth.

Modeling efforts that investigated the different aspects of the involvement of fluids in faulting include Sleep and Blanpied (1992, 1994) and Sleep (1995). They proposed a 1-D fault model mostly sealed from the country rock in which pore pressures follow the seismic cycle. In their model, overpressures are generated via ductile creep during interseismic periods and drop to hydro- or sub-hydrostatic levels after a rupture. Segall and Rice (1995) developed a model for dilatancy and compaction in the framework of a rate- and state-dependent friction law and a spring slider model and showed that pore pressure plays a major role in stick-slip instability. Miller et al. (1996) proposed a 2-D fault model for an elastic half-space including large-scale tectonic loading and using a cellular automaton scheme for the monitoring of pore pressures. Henderson and Maillot (1997) presented a 2-D model of the fluid flow within a tabular fault zone and the competing effects of diffusivity and compaction rate on the seismic cycle. Models of the dynamic triggering (Harris and Day, 1999); static stress triggering (Stein et al., 1997), postseismic deformation (Pollitz et al., 2001), and forward fault interaction models (Robinson and Benites, 1995, 1996) typically ignore fluid processes other than poroelasticity. Earthquake simulations include asperity models (Ben-Zion and Rice, 1993), or synthetic rupture history models (Ward, 1997). The role of fluids in swarm generation has been investigated by Yamashita (1999), and a forward model driven by crustal fluids was developed by Miller et al. (1999) and generalized to 3-D interacting faults by Fitzenz and Miller (2001, FM01). They show how pore pressures influence complexity of the seismic process and the earthquake cycle, but are limited in their analysis by lack of constraints on the hydraulic properties in the framework of a forward 3-D model.

In this study, we investigate a forward model of a ductile tabular fault zone embedded in an elastic half-space. The model combines 3-D large-scale tectonic loading and stress transfer with a detailed handling of the hydraulics of a ductile fault zone. The stress state of the model is complex, with at least four degrees of freedom in stress space. These include the normal stress and shear stress increase due to tectonic loading, shear stress decrease due to shear creep slip, and pore pressure increase due to ductile compaction. Pore pressure changes via poroelastic effects add an additional change in the stress state. The new fault zone conceptual model is chosen after field and borehole observations of active crustal faults. After deriving the system of equations necessary to include a thin viscous layer in the 3-D elastic half-space, we extend the shear creep and ductile compaction model of Sleep and Blanpied (1992, referred to here as SB92) to 3-dimensions. We show that the pressure-dependency of the fluid compressibility plays a key role in the pore pressure drop to hydro- or sub-hydrostatic levels after a seismic event shown in SB92. When extended to 3-D, with more realistic loading and fault zone hydraulics, results show that a mostly overpressured fault below 6 km depth organizes into compartments of varying pore pressures, complex stress states and seismic and creep slip patterns. We discuss implications of the SB92 model in 3-dimensions, the creep slip distribution, the development of overpressures and the role of the pressure dependency of the compressibility as a regulator of model pore pressures. Alternatives such as flow in the direction perpendicular to the fault strike are also discussed.

3.2 Conceptual model of fault zone hydraulics

The conceptual fault zone structure and architecture that we aim to simulate (Figure 3.1) is a simplification of the structure of the Nojima fault inferred from core observations (Tanaka et al., 2001). The fault is characterized by two distinct zones; a relatively low permeability fault core consisting of a coseismic fault surface embedded in a zone composed of breccia and/or cataclasite, or gouge and a high permeability damaged zone surrounding the core. Rawling et al. (2001) review permeability data for contrasting types of fault-zones and show, in the case of a granitic protolith, permeability ratios of 10^3 and 10^{-3} , for the damage zone and the fault core, respectively, with respect to the intact rock. Chester et al. (1993) proposed episodic self-sealing of the fault-bounding rocks as one factor allowing for the generation and maintenance of elevated fluid pressures for studied segments of the San Andreas fault. For a quasi-impermeable narrow seal between the fault core and the surrounding rocks, a small diffusive leakage out of the fault zone during interseismic periods is expected.

Field evidence shows negligible reorientation of planar structures predating the brittle faulting episode except very near or within the fault core (Chester et al., 1993). This suggests that only a negligible component of the total slip on the fault was accommodated by simple shear in the damage zone and that most coseismic displacement occurs along the fault core. In addition, the damaged zone must not necessarily be symmetric with respect to the slipping plane. That is, the damage zone can exist either on both sides (as shown on Figure 3.1) or on only one side of the fault core.

Time-dependent processes such as shear creep and ductile compaction can occur during

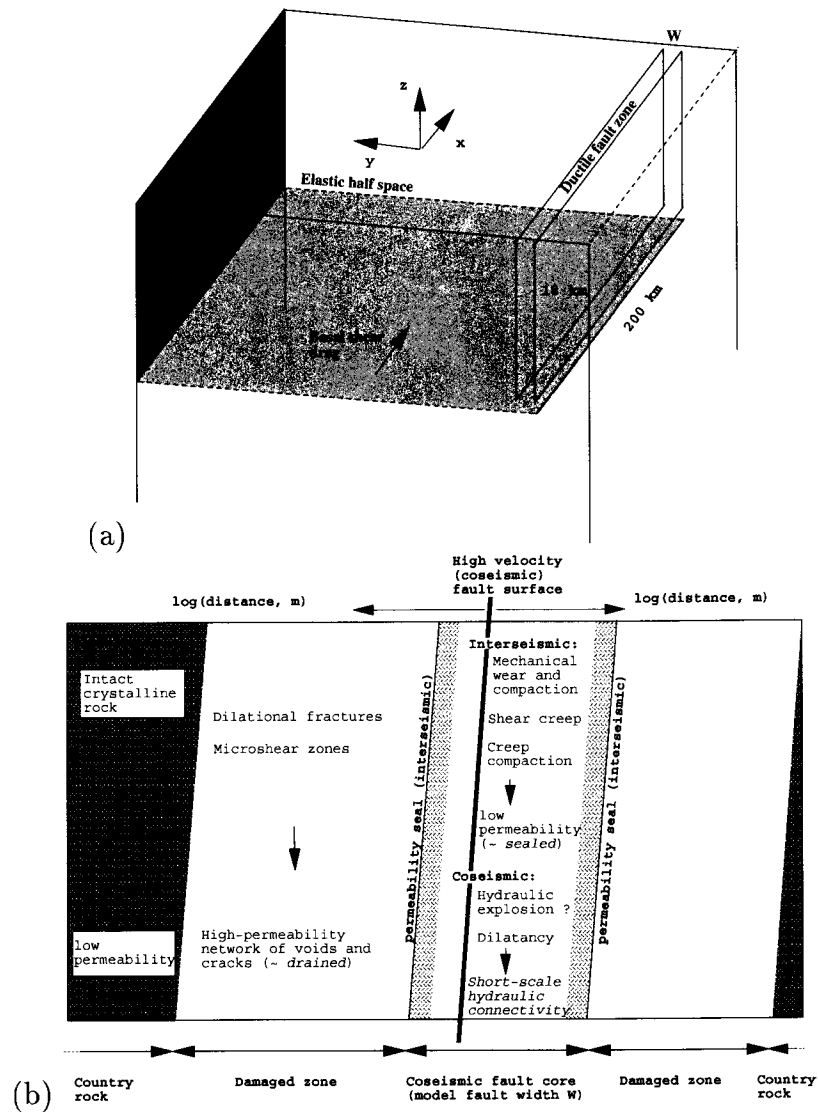


Figure 3.1: Model fault. (a) Model geometry, tectonic loading and boundary conditions. We consider the case of a vertical finite fault model consisting of a sealed tabular ductile body of width W embedded in an elastic country rock (half-space). The tectonic loading is performed via both a basal shear drag (30 mm yr^{-1} at 20 km depth) and a far field compression (3 mm yr^{-1}). We impose a constant hydraulic head condition at the top of the fault. (b) Structure of the model fault zone (adapted after Tanaka et al., 2001). Slip occurs on very narrow fault surfaces embedded in a zone of width W that increases with the total slip. This zone has a low permeability, roughly between 10^{-20} and 10^{-18} m^2 during interseismic periods and up to 10^{-15} m^2 coseismically. The (drained) damaged zone is not part of the model fault zone. A small leakage is allowed out of the fault core.

interseismic periods even on mostly seismic faults (Chester et al., 1993). Sleep and Blanpied (1992) demonstrated that shear creep mildly reduces shear stress, whereas ductile compaction can significantly increase pore pressure in the fault zone (and decrease the frictional strength). As seismic slip initiates and propagates along the fault plane, part of the elastic energy release is used for porosity creation (e.g., frictional dilatancy, Marone et al., 1990). Whether these new cracks and pores are rapidly filled with fluids is still unknown. However, seismic slip can hydraulically connect parts of the fault previously sealed from each other, thus initiating flow.

Stress transfer occurs at wave speeds while flow occurs within diffusive time-scales. Therefore, pore pressures can start equilibrating only after the fault is stable with respect to its stress state and the rupture propagation itself is considered undrained. Undrained poroelastic effects within the cells are passed on to pore pressures without delay. The width of the fault zone increases with total seismic slip (Scholz, 1990; Yamashita, 1999) because of the crack formation (and possibly hydraulic fracturing Tanaka et al., 2001). We consider that the top of the fault is hydraulically connected to the surface and therefore has a constant hydraulic head. This can result in water outflow when the rupture reaches the surface (e.g., pore pressure redistribution).

3.3 The numerical model

As in the original model (FM01), faults of any strike and geometry can be considered. However, we concentrate in this study on the case of a vertical strike-slip fault to be able to compare the results with the 1D case of Sleep and Blanpied (1992). The model fault consists of a matrix of computational cells (subfaults) representing rectangular dislocations and discrete sealed fluid pressure compartments in a deforming elastic half-space. Tectonic loading increases shear stress, normal stress, and pore pressure (through poroelasticity) along the fault planes, while pore pressures increase through poroelastic effects and compaction within the faults. This results in four degrees of freedom in the Mohr diagram (Figure 3.2), and we can therefore expect a complex stress state and seismic behavior. When a cell reaches the Coulomb failure stress, we use Okada's (1985, 1992) analytical solutions to calculate slip on this cell and the stress changes on all other cells of the faults. The fluid-related processes are accounted for via undrained poroelasticity, a source term, frictional dilatancy, and a toggle switch in permeability allowing an instantaneous equilibration of pore pressures over the entire slipped area at the end of a seismic event (see Fitzenz and Miller, 2001, for more details). Differences with FM01 include an explicit calculation of the compaction rate, a total slip-dependent fault zone width, and an incremental pore pressure redistribution. These are presented in the next sections. The new pore pressure state after equilibration can change the Coulomb failure stress and trigger slip on other cells during the same event. Tectonic loading is decomposed into basal shear drag parallel to the plate boundary with a 30 mm yr^{-1} plate velocity, and a ridge push, or gravity push (e.g., of Sierra Nevada mountains on the San Andreas fault system) compression approximated by a vertical dislocation surface applied at the far-field boundary resulting in fault-normal compression rates in the model space of 3 mm.yr^{-1} (Argus and Gordon, 1991, proposed 2 mm yr^{-1} (-1 to $+5 \text{ mm yr}^{-1}$) from interferometry surveys).

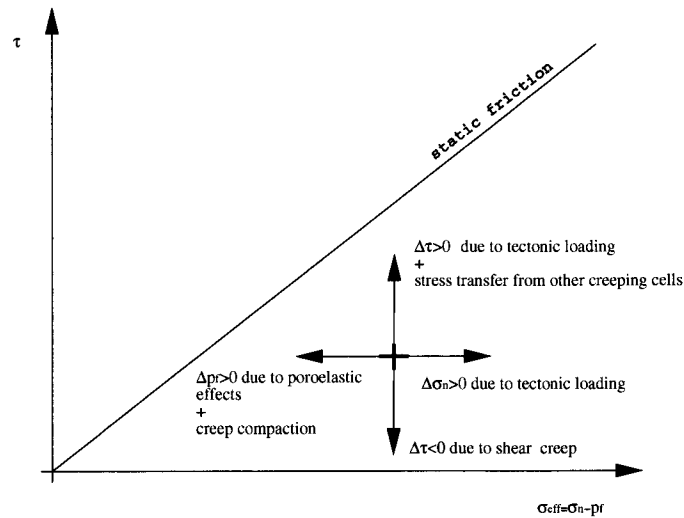


Figure 3.2: Degrees of freedom in the Mohr-space to consider when calculating the exact time step to the next failure of a cell in the model fault system. During interseismic periods, shear stress decreases on a cell due to shear creep and increases from both tectonic loading and stress transfer from other creeping cells, whereas the effective stress increases from normal stress increase and decreases due to pore pressure increase (from poroelastic effects and creep compaction).

3.3.1 A viscoelastic fault core: shear creep and compaction rate

The properties of the subfaults (e.g., porosity, compressibility, Skempton's coefficient, friction coefficient, pore pressure) are now explicitly defined as those of the coseismic fault core. We assume that slip occurs on very narrow fault surfaces embedded in a highly deformed zone of width W . Chester et al. (1993) observed on exhumed faults of the San Andreas fault system that both the total fault zone thickness, and the fault core thickness scale with displacement. Following Yamashita (1998), the fault core widens with the total accumulated slip at any given location \mathbf{x} on the fault by:

$$W(\mathbf{x}) = \zeta \sum_m D_m(\mathbf{x}) + W_o, \quad \zeta \in [0.001, 0.1], \quad (3.1)$$

where W_o is the initial width, D_m is the total seismic slip of the subfault during event m and is summed for all the past seismic (brittle) events at a given time. The parameter ζ is interpreted as a wear rate. When slip and thickness data are collected for faults in crystalline rocks (Scholz, 1990), the cloud of points lies between lines of $\zeta = 0.001$ and $\zeta = 0.1$, and we chose $\zeta = 0.05$.

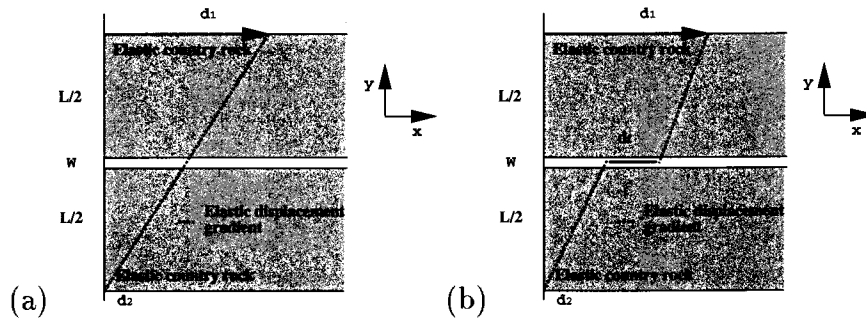


Figure 3.3: Geometry and boundary conditions (map view) between the tabular sealed ductile fault zone of width W and the country rock. L is the effective width of the region which deforms elastically. The displacements imposed at the boundaries are d_1 and d_2 in the general case discussed in section 3.3.1. (a) case where no slip occurs in the fault zone; (b) case where a displacement d_f has occurred on the fault.

Applying a 1D formalism in a 3D case

Following the model of Sleep and Blanpied (1992), we consider a viscoelastic fault core of width W and down-dip extension within the seismogenic layer embedded in an elastic half-space. The introduction of a thin viscous layer requires the rewriting of the set of equations for modeling creep slip and pore pressure increase rates. Consider a tabular viscous fault core, infinite along strike (x -axis) and in depth (z -axis), of width W (y -axis) embedded in an elastic country rock (Figure 3.3). A shear displacement is applied along x on the elastic body over an effective width L . Static equilibrium requires continuity of both shear stress and normal stress across the fault core. Therefore, the shear stress at the interface between the country rock and the fault core is given by $\sigma_{xy} = G \frac{\partial u_x}{\partial y}$. This is equivalent to $\sigma_{xy} = G \frac{d_1 - d_2 - d_f}{L}$, where G is the rigidity of the country rock, d_1 and d_2 are the displacements imposed on both sides of the elastic body, and d_f is the creep displacement along the fault.

The creeping rate along the fault for a linear viscous medium of shear viscosity η is $\dot{d}_f = \int_W \frac{\sigma_{xy}}{\eta} dy$, where W is the fault zone width and \dot{d}_f is the slip rate along the fault. Thus,

$$\dot{d}_f = G \frac{d_1 - d_2 - d_f}{L} \int_W \frac{dy}{\eta} \quad (3.2)$$

The relationship between the total effective stress and the compaction rate for a ductile fault core is:

$$K \frac{D\phi}{Dt} = P_f - P_T, \quad (3.3)$$

where ϕ is the porosity of the fault core, P_f is the pore pressure, P_T is the total applied stress and D/Dt is the material derivative ($\frac{D}{Dt} = \frac{\partial}{\partial t} + \mathbf{v}_s \cdot \nabla$). K is the bulk viscosity (with units Pa s) (Sleep and Blanpied, 1992) and relates deformation to deformation rate (Barnes et al., 1993, page 169) (see calculation in section 3.3.1).

The conservation equations for the solid and the liquid are:

$$\begin{cases} \frac{\partial \rho_f \phi}{\partial t} + \nabla \cdot (\phi \rho_f v_f) = 0 \\ \frac{\partial \rho_s (1-\phi)}{\partial t} + \nabla \cdot ((1-\phi) \rho_s v_s) = 0 \end{cases} \quad (3.4)$$

where ρ_f , v_f , and ρ_s , v_s are the densities and the velocities of the fluid and the solid, respectively. Assuming an incompressible solid matrix (e.g., ρ_s is constant), and by adding equation (3.4):

$$\begin{cases} \nabla \cdot (\phi v_f + (1-\phi) v_s) + \frac{\phi}{\rho_f} \frac{\partial \rho_f}{\partial t} = 0 \\ -\frac{\partial \phi}{\partial t} + \nabla \cdot ((1-\phi) v_s) = 0 \end{cases} \quad (3.5)$$

Darcy's law is given by:

$$\phi(v_f - v_s) = -\frac{k}{\mu_f}(\nabla P_f - \rho_f g), \quad (3.6)$$

with k permeability within the fault core and μ_f fluid viscosity. Introducing the compressibility of the fluid $\beta_f = \frac{1}{\rho_f} \frac{\partial \rho_f}{\partial P}$ and the material derivative, we get the conservation equations:

$$\begin{cases} \nabla \cdot \left(\frac{k}{\mu_f} (\nabla P_f - \rho_f g) \right) + \phi \beta_f \frac{\partial P_f}{\partial t} = \nabla \cdot (v_s) & (a) \\ \frac{1}{1-\phi} \frac{d\phi}{dt} = \nabla \cdot (v_s) & (b) \end{cases} \quad (3.7)$$

The four unknowns are the total stress, the pore pressure, the porosity and the creep displacement. Equation (3.3) gives the compaction rate, equations (3.7)a and b give the pore pressure increase rate, and equation (3.2) gives the creep displacement. An additional constraint is provided by the total stress in the fault zone:

$$P_T = \phi P_f + (1-\phi) P_s \quad (3.8)$$

If we assume that the porosity in faults formed in crystalline rocks is small, then $P_T \sim P_s$, where $P_s = tr(\sigma)/3$ is the mean stress in the solid. σ_{yy} is known from continuity but σ_{xx} and σ_{zz} are not known. Qualitatively, the temporal changes of $\sigma_{xx} - \sigma_{yy}$ (or $\sigma_{zz} - \sigma_{yy}$) depend on the creeping velocity and should relax back to an initial value if the creeping stops at a rate that depends on both the rigidity of the elastic body and the viscosity of the fault core. If we assume that $\sigma_{xx} = \sigma_{zz}$ and defining $\Delta\sigma = \sigma_{xx} - \sigma_{yy}$, a heuristic model for viscous (e.g., elliptical) inclusions in an elastic half-space would give an equation of the form 3.9 (Y.Y. Podladchikov, personal communication):

$$\frac{d\Delta\sigma}{dt} = C_1 G \frac{\dot{d}_f}{L} - C_2 \frac{G}{\eta} \Delta\sigma, \quad (3.9)$$

where C_1 and C_2 are constants depending both on the geometry of the inclusion and on the contrast in elastic modulus and viscosity between the inclusion and the half-space. An interesting follow-on study would be to investigate the total stress field in the ductile core, but is beyond the scope of the current study.

Making the following assumptions, we can use the formalism developed by Sleep and Blanpied (1992): a) ϕ is small so that $P_T \sim P_s$ and $1 - \phi \sim 1$ in equation 3.7b, b) $\dot{d}_f = G \frac{D}{L} \frac{W}{\eta}$, where D is the elastic displacement stored in the country rock, c) all the diagonal elements of the stress tensor are equal to the stress normal to the fault with $P_s = \sigma_n + 2/3 \Delta\sigma = \sigma_n$, and d) the fluid is redistributed instantaneously within the fault zone in response to compaction (e.g., pore pressures within the cells are in equilibrium). This last point means that the first term of equation 3.7a describing fluid flow is zero. Numerically, this condition asks for high resolution studies. Ignoring the details of the velocity distribution within the fault zone, the ductile behavior of the fault core during interseismic periods is described by:

$$\begin{cases} \tau = DG/L & (a) \\ V = \dot{d}_f = \frac{\tau W}{\eta} & (b) \\ \frac{d\phi}{dt} = \frac{1}{K} \times (P_f - \sigma_n) & (c) \\ \frac{\partial P_f}{\partial t} = \frac{1}{\beta_f \phi} \frac{d\phi}{dt} & (d) \end{cases} \quad (3.10)$$

where τ is the shear stress, G is the elastic modulus, η is the shear viscosity, W the fault core width, ϕ its porosity, K is the bulk viscosity, P_f pore pressure and σ_n normal stress within the fault core, and V the shear creep velocity, i.e., the velocity of one wall of the fault zone with respect to the other wall. For the 3D case discussed below (section 3), the shear stress is determined by the solutions of Okada (for a half-space) instead of equation (3.10)a. We allow for a small leakage out of the fault zone towards the country rock (via the damage zone high permeability) using a correction term to be added to the rate of pore pressure change in equation (3.10)d:

$$\frac{\partial P_f}{\partial t} \text{ diff} = - \frac{P_f - P_h}{t_h} \quad (3.11)$$

where P_h is the hydrostatic pore pressure in the surrounding rocks and t_h is the leak time (Sleep and Blanpied, 1992). A simple calculation shows that the ratio between pore pressure increase rates due to compaction and pore pressure decrease rates due to leakage vary between 2 and 25, for high pore pressures or nearly hydrostatic pore pressures, respectively. The calculation was made at 14 km depth, with $P_{f1} = 250$ MPa, $P_{f2} = 150$ MPa, $\sigma_n = 400$ MPa, $P_h = 137$ MPa, $\phi = 7.4\%$ and $\eta_i = 2.510^{19}$ Pa s (810¹¹ Pa yr), see equation (3.14)).

Porosity structure and viscosity coefficients

The porosity of the fault core is made of a wide range of pore shapes, usually represented schematically as the superposition of (micro- and macro-) cracks and equidimensional pores, and referred to as a double porosity model. Taking into account these two end-member cases (cracks and spherical pores) in a comprehensive way would require a detailed knowledge of the distribution of these cracks and pores (e.g., position, orientation, aperture or aspect ratio). We simplify the problem by re-writing some of the equations derived by Sleep (1995), and Sleep and Blanpied (1992, 1994) concerning creep compaction and frictional dilatancy. As pointed out in SB92, cracks and equidimensional pores behave

differently during creep. Sleep and Blanpied (1994) therefore introduce a compaction rate equation for cracks in a medium where pores may also be present, and one for spherical pores in a medium where cracks may also be present (Sleep and Blanpied, 1994, equations 7a and 7b). We advocate that most of the porosity changes relevant to our model are related to cracks (or to sub-grain-scale pores that compact as cracks). Therefore we only consider cracks and adapt their equation 7a (written with our notations in equation 3.12) to our total porosity model:

$$\frac{\partial f_c}{\partial t} = -(\sigma_n - P_f) \left[\frac{2\alpha_c f_c}{\eta_i} \right] \left[\frac{9 + 4\alpha_c f_c + 4f_p}{27 + 36\alpha_c f_c + 36f_p} \right], \quad (3.12)$$

where f_c refers to the crack porosity, α_c is the crack aspect ratio, f_p is the pore porosity, and η_i is the intrinsic viscosity of the grains. The intrinsic viscosity of the grains is a common parameter needed to derive both the shear and the bulk viscosity as motivated by grain-scale physics. At this scale, the nature of the applied stresses (e.g., shear or confining stresses) is not relevant in that both stresses induce a deformation rate. However, cracks close almost instantaneously at depth, whereas pores compact much slower, and the porosity is not 0 when all the cracks are closed but is equal to the “spherical” pore porosity. We introduce a residual porosity ϕ_{\min} to account for this behavior. We also adapt the compaction equation so that the rate reduces rapidly to zero as the porosity approaches this minimum porosity (slow compaction rate for equidimensional pores). We finally assume that 1) the porosity ranges between ϕ_{\min} and a saturation porosity ϕ_{\max} (see next section), and 2) the product of the crack porosity and the crack aspect ratio, present in the viscosity calculation, is equal to 1 for a highly fractured material. The shear viscosity η to be used in equations (3.10)b is:

$$\eta = \frac{9\eta_i}{13 + 4\phi}, \quad (3.13)$$

and the bulk viscosity K (to be used in equations (3.10c) is given by

$$\frac{1}{K} = \frac{2}{\eta_i} \left[\frac{13 + 4\phi}{63 + 36\phi} \right] \left[\frac{\phi - \phi_{\min}}{\phi_{\max} - \phi_{\min}} \right]^a, \quad (3.14)$$

The last bracketed term corresponds to the correction term that is close to 1 when the porosity is large, and decreases the compaction rate to zero when the cracks are closed. The exponent a controls how fast the compaction rate will decrease when ϕ decreases; the lower the exponent, the faster the decrease. Table 3.1 lists the numerical values chosen for all the model parameters. Although motivation for this model is derived from sub-vertical strike-slip faults, Labaume and Moretti (2001) show that both the fault zone structure and the processes are also found in thrust fault zones. Therefore, our model could be expanded to more complex fault system geometries.

A 3-D case of fault zone without in-plane flow

The first simulation attempts to reproduce the results of Sleep and Blanpied (1992) in a 3-D case. We present results for a 3D vertical fault zone discretized into sealed subfaults (no

Table 3.1: Model Parameters and Initial Conditions. ^a After Sleep and Blanpied [1994],
^b After Sleep [1995]

Initial Model Parameters	Range of Values
Cell size	2000 m along strike by 500 m up-dip
Fault area	200 km along strike by 18.5 km up-dip
Initial width	10 cm
Basal shear	30 mm yr ⁻¹ parallel to the plate boundary
Far field compression	3 mm yr ⁻¹ perpendicular to the plate boundary
Lame coefficients	$\lambda_{\text{lame}} = G = 30 \times 10^9$ Pa,
Time step	time required to initiate failure on exactly one cell
Compressibility $\beta = \beta_\phi + \beta_f$	10^{-3} MPa ⁻¹
Initial porosity ϕ	random between 2 and 7%
Saturation porosity ϕ_{max}	linear with depth between 7% (top) and 3% (bottom)
Residual porosity ϕ_{min}	2%
Skempton coefficient B	random between 0.4 and 0.8
Initial normal stress σ_n	lithostatic, $\rho_r g z$, $\rho_r = 2700$ kg m ⁻³
Initial shear stress	$0.3 \times \sigma_n$
Initial pore pressure gradient	hydrostatic
Compaction	for $-z < 3$ km, $\dot{\phi} = 0$ for $-z > 3$ km, creep compaction ^a
Viscosity ^b η_i	2.78×10^{11} Pa yr
Bulk viscosity exponent	0.1
Fluid sources $\dot{\Gamma}$	none
Friction coefficients	static, $\mu_s = 0.6$; dynamic, $\mu_d = 0.5$
Dilatation coefficient ^b r_m	18×10^{-3}

in-plane flow), loaded as described in equation (3.10)a. Except for the fluid compressibility (we assume constant compressibility, see Table 3.1) the model parameters are those of SB92 for their Model 1 (see tables 1 and 2, Sleep and Blanpied, 1992). The width W is taken as 1 m, and does not increase with total slip. Figure 3.4 shows model results for a cell at 14 km depth for a 500 year simulation where a steady-state is reached. This figure is to be compared to Figure 2 of SB92. The beginning of the simulation, from $t=0$ to about 60 years (e.g., time of the first event) shows a rapid pore pressure increase above hydrostatic, a slow shear stress increase via tectonic loading (top) and a rapid porosity reduction. No significant creep slip has occurred. At the time of the first rupture where the average slip is about 1.5 m, porosity increases from 7.96 % to 8.91% by frictional dilatancy. This increase is comparable to the increase of 1.3% shown in SB92, but the effect on pore pressure is very different. In the case of constant compressibility, fluid mass conservation yields $P_{new} = \frac{\phi_{old}}{\phi_{new}} \times P_{old}$, where subscripts *old* and *new* refer to pre- and post-seismic values, respectively. Figure 3.4 shows that pore pressure decreases from about 250 MPa to about 230 MPa, while in SB92 pore pressure drops from 267 MPa down to sub-hydrostatic levels 54 MPa. The difference in behavior rests with the pressure-dependent compressibility. While we agree that pressure-dependent compressibility has an important effect on the post-seismic pore pressure state, we will argue (and show below) that if the 2nd and 3rd dimensions of the fault zone are considered, pressure-dependent β_f plays a secondary role on the actual equilibrated pore pressure. If the compressibility is kept constant, the subfault evolves to a weak (low shear stress), overpressured fault, with a creep slip/seismic slip ratio of about 3%. Consequently, seismic slip occurs every 8.3 years on average, with much shorter recurrence times than in SB92 (130 yr). The recurrence time is reduced markedly for two reasons. The first one is the already mentioned smaller drop in pore pressure after an event (keeping the frictional strength at a low level). The second one is stress transfer from the surrounding subfaults and is seen on the shear stress curve as sudden small increases (steps). This brings the shear stress to the failure stress faster than with tectonic loading alone. Therefore, both the compressibility of the fluid and stress transfer have a significant effect on the resulting behavior of the visco-elastic fault zone.

3.4 3D model

We introduce the ductile fault zone described previously into a 3-D model of faulting. The fault zone model is coupled to the forward fault interaction model of Fitzenz and Miller (2001). During interseismic periods large-scale tectonic loading increases stresses on the fault and fault compaction increases pore pressures in each sealed subfault. Seismic slip increases porosity (frictional dilatancy) and breaks the impermeable seals between subfaults, allowing pore pressures redistribution between the slipped patch and the neighboring subfaults. Boundary conditions on the model include a basal shear drag and a far field compression to simulate a transpressional environment. Basal drag is represented by a rectangular dislocation at the base of the model fault moving at constant velocity, and fault normal compression is simulated via an opening mode vertical dislocation. Since pore pressures increase rapidly through ductile compaction, it is very important to consider hydraulic property evolution. Small scale incremental pore pressure redistribution

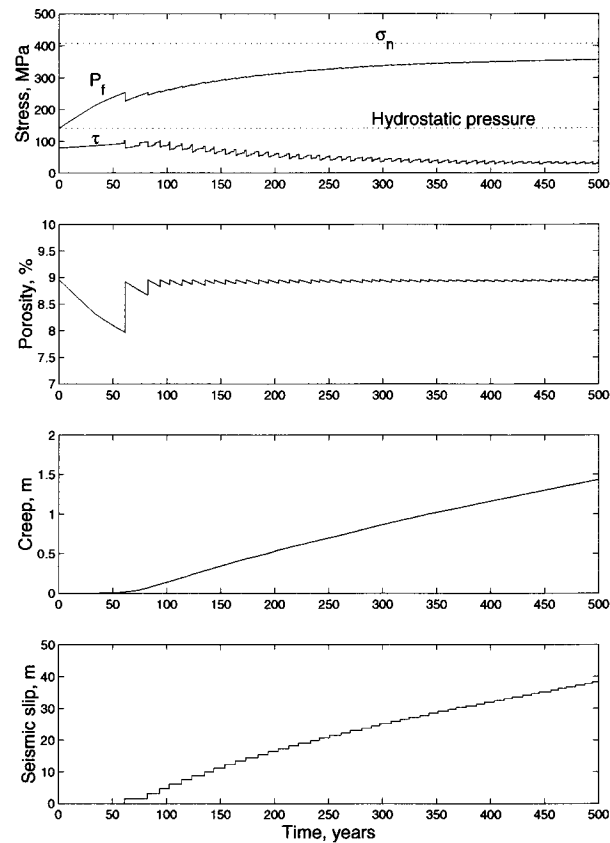


Figure 3.4: A 3-D case of ductile fault zone without in-plane flow: model results for a cell at 14 km depth for a 500 year simulation (constant fluid compressibility). From top to bottom: Stress state. The two solid lines show the time evolution of shear stress and pore pressure whereas the two dotted lines show the hydrostatic and the lithostatic pressure at 14 km depth. Porosity evolution. Creep slip. Seismic slip. Results show first a period of quiescence from $t=0$ to about 60 years. Shear stress increases due to tectonic loading, pore pressure increases due to compaction (from 9% to 8% porosity), and no slip has occurred yet. At the time of the first rupture where the average slip is about 1.5 m, porosity increases from 7.96 % to 8.91% by frictional dilatancy and pore pressure decreases from about 250 MPa to about 230 MPa, still above hydrostatic. The small drop in pore pressure after an event keeps the frictional strength at a low level, leading to a weak fault, with high pore pressure, short seismic cycles (about 8 years) and low shear stress. The sudden positive steps in shear stress show stress transfer from other cells.

(see below) avoids great fluid outflows when the ruptures reach the top of the fault. Other changes were made to add features specific for ductile fault zones.

3.4.1 Interseismic hydraulic property changes

Ductile compaction and leakage out of the fault zone are handled as described in the previous sections. The total interseismic pore pressure change rate is:

$$\frac{\partial P_f}{\partial t} = -\frac{(P_f - \sigma_n)}{\beta_f \phi} \frac{2}{\eta_i} \left[\frac{13 + 4\phi}{63 + 36\phi} \right] \left[\frac{\phi - \phi_{\min}}{\phi_{\max} - \phi_{\min}} \right]^a - \frac{P_f - P_h}{t_h} \quad (3.15)$$

3.4.2 Coseismic hydraulic property changes

Frictional dilatancy.

Seismic slip increases porosity, but whether this frictional dilatancy is a drained or an undrained process is still unclear. For simplicity, we consider that pore pressure actively affects crack propagation in that it lowers the effective stress at the tip of the propagating crack. Hence, although fluids do not fill the new porosity instantaneously, we consider that pore pressure aids the propagation of the cracks responsible for the increase in porosity. Therefore, the energy per fault area (G_p) required to create porosity will depend on the effective stress and not on the normal stress only. That is, $G_p = (\sigma_n - P_f)W\Delta\phi$ (see Sleep, 1995, for similar approach). On the other hand, the energy released via seismic slip (elastic strain release per fault area) is expressed as $G_F = \frac{1}{2}(\tau_{\text{old}}D_{\text{old}} - \tau_{\text{new}}D_{\text{new}})$, where D_{old} and D_{new} are recoverable displacements just before and just after the rupture, and τ_{old} and τ_{new} are shear tractions for the same two states (Sleep and Blanpied, 1994). If we assume that only a small fraction r_m of the seismic energy is available for crack creation (as suggested by Marone et al., 1990), then $\Delta\phi \equiv \frac{r_m}{2(\sigma_n - P_f)W}[\tau_{\text{old}}D_{\text{old}} - \tau_{\text{new}}D_{\text{new}}]$. Differentiating with respect to D_{new} , we get:

$$\frac{\partial \phi}{\partial D} \equiv -\frac{r_m \tau}{2(\sigma_n - P_f)W}, \quad (3.16)$$

which gives the porosity creation per unit slip. However, as Marone et al. (1990) pointed out, the porosity can not increase via frictional dilatancy beyond a saturation value ϕ_{\max} . We introduce a correction term such that:

$$\frac{\partial \phi}{\partial D} \equiv -\frac{r_m \tau}{2(\sigma_n - P_f)W} \left[\frac{\phi_{\max} - \phi}{\phi_{\max}} \right], \quad (3.17)$$

where the term in brackets keeps the proportionality between pore creation rate and faulting energy at low porosity but saturates to ϕ_{\max} . Two additional comments are needed. First, because we use the total porosity and not the crack porosity in equation 3.17, we have to introduce a linear depth-dependency in ϕ_{\max} that reflects that the high confining stress would not enable the persistence of crack porosity at depth. The maximum porosities range between 7% at shallow depth (.5 km) and 3% at greater depth (18 km). The lower bound (3%) corresponds to a maximum of 1% of crack porosity and

2% of pore porosity. Secondly, since we explicitly monitor $\tau/(\sigma_n - P_f)$, this term can not be simply replaced by a friction coefficient.

Permeability evolution during slip.

As mentioned previously, each cell (or subfault) is initially hydraulically disconnected from in-plane cells. Seismic slip can break the in-plane seals. In terms of permeability, this is equivalent to saying that the in-plane permeability of the slipped cells switches from less than 10^{-18} m^2 to about 10^{-15} m^2 over the time step following the event. We consider that at the beginning of the next time step, all subfaults are sealed again. The rate of sealing is a complex problem addressed elsewhere (Gratier et al., in press) but in this simple model, we assume that fault sealing is a rapid process. An additional pore pressure regulation process is a slow diffusive leakage in the direction perpendicular to the fault strike out of the fault core during interseismic periods (Sleep and Blanpied, 1992). Little is known about the co-seismic connection to the damage zone, but the effect is likely very significant and should be investigated in future studies (Henderson and Maillot, 1997; Gratier et al., in press).

Pore pressure changes

The main issue when dealing with the effects of fluids in fault zones is to evaluate the time-scales relevant for each process. Stress transfer occurs at acoustic velocities (on the order of km s^{-1}), while fluid flow is controlled by diffusion. Therefore, in the model, we allow undrained poroelastic effects in response to the changing stress during rupture propagation, which can affect the frictional strength during rupture.

For a diffusion time of less than 3 months (on the order of the time steps) and a permeability of 10^{-15} m^2 (a reasonable co-seismic permeability estimate), the diffusion length is about 2.5 km (Townend and Zoback, 2000). Since our cells are $2.0 \text{ km} \times 0.5 \text{ km}$, we therefore allow the pore pressure of a slipped cell to equilibrate with its nearest neighbors within a time step as a proxy for in-plane diffusion (see size of the cells in Table 3.1). The equilibrium fluid pressure \bar{P}_f among the m affected cells is calculated via:

$$\bar{P}_f = \frac{\sum_{i=1}^m [(\phi\beta W)_i (P_{f_i} - \rho g \Delta z)]}{\sum_{i=1}^m (\phi\beta W)_i} + \rho g \Delta z, \quad (3.18)$$

where ρ is the fluid density. Pore and fluid compressibilities are mixed into a single parameter $\beta = \beta_f + \beta_\phi$. This equation is different from that of Fitzenz and Miller (2001) because the width of the fault core is neither constant in time (total slip dependency) nor homogeneous in space along the fault. The relative storage capacity of each cell is now explicitly $(\phi\beta W(\mathbf{x}))_i$. Conceptually, flux normal to the fault could be much higher than in-plane flow because of the much larger cross-sectional area, but is not included in the current study. Pore pressure changes are calculated as slip propagates, as described in Miller et al (1999), but this does not feed back on the frictional strength of the fault during the propagation of the event. These changes are monitored but stored and brought back once the stress equilibrium is reached. We assume that by the end of the event, the new cracks created by frictional dilatancy are filled, and we take these porosity changes

into account when we calculate the increments of pore pressure redistribution.

When the system reaches equilibrium with respect to its stress state, pore pressures are updated for all the changes listed above and the cells are checked again for frictional failure. In case pore pressure happens to be higher than the minimum principal stress σ_3 at the seal between the fault core and the country rock (e.g., taken as 92% of the normal stress for the systems investigated so far), we allow hydrofractures to open, draining excess fluid from the overpressured fault core to the drained damaged zone (Scholz, 1992). This consists in a drop in pore pressure to just below σ_3 , without stress changes, and this pressure drop is assumed instantaneous.

3.4.3 New calculation of time steps

In keeping with our rigorously quasi-static model, the calculation of the time-step necessary to fail exactly one cell needs to be determined. To determine the time step, we need to consider the stress path to failure during the interseismic period. Each cell approaches the failure condition by a path determined by the shear stress change rate $\frac{\partial \tau}{\partial t}$, the normal stress change rate $\frac{\partial \sigma_n}{\partial t}$, and the pore pressure change rate $\frac{\partial P_f}{\partial t}$ (Figure 3.2). The first two depend on the tectonic loading and to the shear creep, and are dependent on the fault orientation. Pore pressure changes result from both poroelastic effects and viscous compaction.

The introduction of shear creep requires the calculation of a creep velocity for each sub-fault in the system. Shear creep is a function of shear stress, porosity and width (equation 3.10b), and the subsequent stress transfer from each creeping subfault to all subfaults in the model fault system. This makes the time step calculation non-linear and could rapidly become computationally awkward and difficult to manage for large faults or for complicated fault systems. Therefore, for simplicity, we consider only the pure strike-slip creep slip. For this case, and for planar faults, we consider that shear creep induces no changes in normal stress. We found that the changes of viscosity with time in the calculation of the shear creep displacement were negligible (i.e., the small effect of the porosity reduction on the viscosity, equation 3.13) so that we linearized the calculation of shear stress changes due to shear creep. To calculate the shear stress changes due to shear creep, the stiffness coefficients are calculated using the analytical solutions of Okada (1992), and the creep displacement is obtained from the integration of equation 3.10b with respect to time t . On first order, we get a time to failure for each subfault i :

$$\Delta t_i = \frac{-[\tau_i - \mu_s(\sigma_{n_i} - p_{f_i})]_{init}}{[sk\tau_i - \mu_s(sk\sigma_{n_i} - skp_{f_i} - p_{f_{rate_i}})] + \sum_{j=1}^n K_{ij} \frac{W_j}{\eta_j} \tau_j}, \quad (3.19)$$

where $sk\tau_i$, $sk\sigma_{n_i}$ and skp_{f_i} refer to increase rates in shear stress, normal stress and pore pressures, respectively, due to tectonic loading (and poroelastic effects). $p_{f_{rate_i}}$ includes both the pore pressure increase rate due to ductile compaction and the decrease due to leakage out of the fault plane (equation 3.15), and μ_s is the static friction coefficient. The time step is the minimum of these Δt_i

3.4.4 Results of the full 3D model and interpretation

Figure 3.1a shows the geometry investigated. To condition the model, we allow 900 years of tectonic loading (e.g., a stress build-up phase without any seismic or aseismic slip), before creep slip and compaction are initiated on the fault. We monitor the stress and pore pressure state, the seismicity, creep slip, the porosity and the width of the fault zone for each subfault.

Slip on the fault: total seismic slip and total creep slip distributions

Figures 3.5 and 3.6 show the state of the fault at $t=1020$ years. This time corresponds to a seismic activity of 1500 events, of magnitude ranging from 3.9 to 6.5 (with a slope of the frequency-magnitude relationship about 0.9), and a creep slip of about 5 cm on average at depth. Each individual seismic rupture shows the strong spatial heterogeneity that was also characteristic in the purely elastic model (Fitzenz and Miller, 2001). The cumulative seismic slip distribution is therefore also heterogeneous (Figure 3.5a) and the total seismic slip ranges between 1 and 5.5 m. The depth-variability of slip is a consequence of the depth-dependent shear stress loading, and slip is non-uniform along strike from the complexity of the stress state on the fault. For an initial fault width of $W_0=10$ cm, the width distribution reflects the total slip distribution, with a maximum width of 32 cm. Equation 3.10b shows the dependency of the shear creep velocity on fault width. However, it also depends on shear stress. Figure 3.5 (b) shows the cumulative creep slip distribution, also for $t=1020$ years. The small scale of the heterogeneity of the distribution, as well as the overall increase with depth reflects more the variations in the shear stress distribution (Figure 3.6(a)) than that of the width of the fault core. In this simulation, the intrinsic shear viscosity is $2.5 \times 10^{19} \text{ Pa s}$ ($8 \times 10^{11} \text{ Pa yr}$) and the creep slip is very small, corresponding to a creep-seismic slip ratio of maximum 0.8 %. It is of the same order as the ratio obtained by Sleep and Blanpied (1992) for their first simulation. With an intrinsic viscosity of $3.15 \times 10^{19} \text{ Pa s}$ ($1 \times 10^{12} \text{ Pa yr}$) and a width of $W=1$ m, they obtained a ratio of 0.2% at 14 km depth. Even though the parameters are not the same, the width to viscosity ratios that govern the creep velocity are comparable. In terms of slip behavior, the two models (1D and 3D) are shown to be comparable and mostly seismic.

Pore pressure compartments

The simulation begins with hydrostatic pore pressures throughout the fault plane, and the boundary condition specifies that the fault is mostly sealed except at the top where a constant hydraulic head is applied. This results in a loss of fluids when seismic ruptures reach the surface. The high initial effective stress from the hydrostatic initial condition results in a high ductile compaction rate (equation 3.10c); the only source of pore pressure increase in the model.

Figure 3.6 (b) shows the evolved pore pressure to normal stress ratio ($\lambda = P_f/\sigma_n$) distribution on the fault plane after 1020 years. It has two main features. First, it shows small compartments (of area mostly from 2 to 9 subfaults, so about 6 km along strike by 3 km in depth) compared to the distributions obtained by Fitzenz and Miller (2001) for

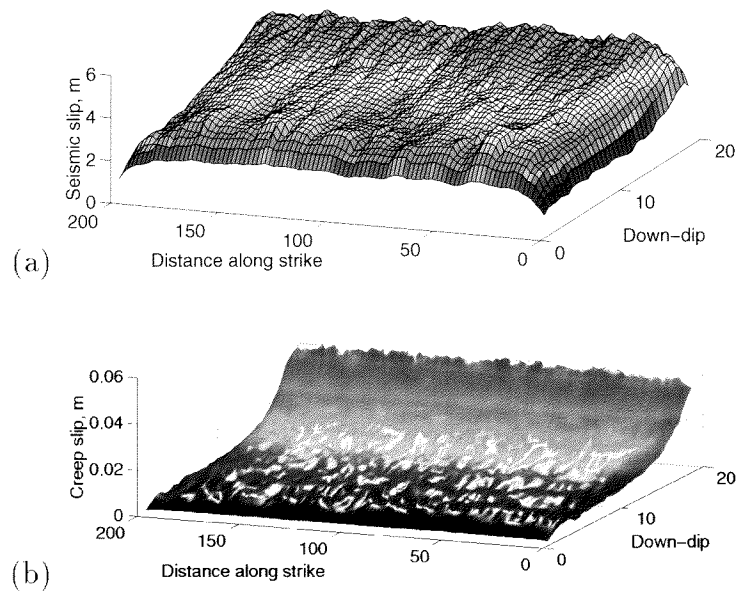


Figure 3.5: Total displacement on the fault at $t=1020$ years. (a) Seismic slip: it ranges from 1 to 5.5 m, with the maximum values reached below 10 km depth. As in FM01, each time slip is evaluated on a cell, it is calculated to induce a drop of 25% of the current shear stress. It is therefore expected to get more slip at depth where the shear stress is the largest (e.g., tectonic loading). The total slip distribution corresponds to about 1500 events with magnitudes ranging from 3.9 to 6.5 and a slope of the frequency-magnitude relationship about 0.9. (b) Creep slip: the small scale of the heterogeneity of the distribution, as well as the overall increase with depth reflects more the variations in the shear stress distribution (Figure 3.6 (a)) than that of the width of the fault core. In this simulation, the intrinsic shear viscosity is 2.78×11 Pa yr and the creep slip is extremely small: maximum 5 cm (reached at depth lower than 12 km). This corresponds to a creep-seismic slip ratio of maximum 0.8 %.

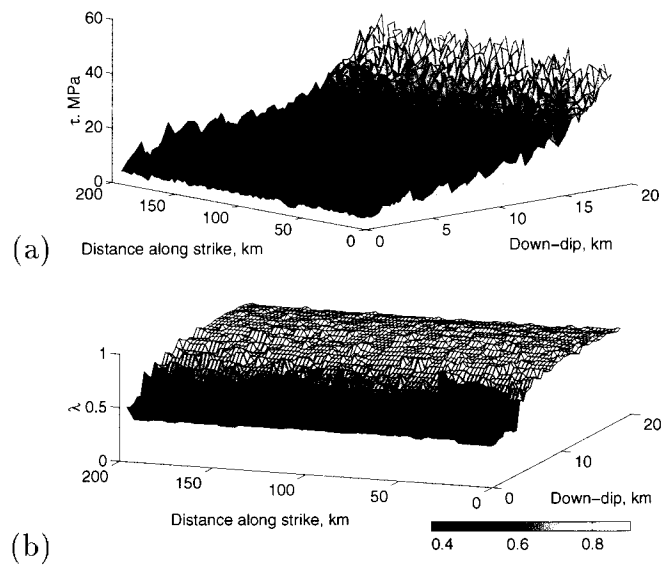


Figure 3.6: Stress and overpressure state on the fault at $t=1020$ years. (a) Shear stress distribution. The distribution shows small scale heterogeneities, as well as an overall increase with depth due to the tectonic loading, (b) Pore pressure to normal stress ratio (λ). The fault is strongly overpressured below 6 km depth and the pore pressure distribution is organized in small compartments.

a similar mean compaction rate (about $3 \times 10^{-5} \text{ yr}^{-1}$). This difference results from the manner in which the new pore pressure state is calculated during the co-seismic propagation of the ruptures. The incremental redistribution used in the present study promotes smaller scale incremental homogenizations of the pore pressures and avoids a significant cell-size effect. This result is in better accordance with the conclusions of Fenoglio et al. (1995) (see discussion) but how these compartments actually may exist is unknown. A second feature of the model is that the fault is strongly overpressured below 6 km depth. Although the persistence of overpressures at this depth is acceptable in view of field observations or inferences (see review in Quattrocchi, 1999), it is a marked difference with the predictions of the 1D model of Sleep and Blanpied (1992). In their model, they expect the interseismic pore pressure increase due to ductile compaction to be compensated by the drop in pressure due to co-seismic pore creation (frictional dilatancy). These differences and implications are discussed below.

3.5 Discussion

3.5.1 Controls on pore pressure evolution

Adapting the 1-D formalism of SB92 to a 3D model that includes in-plane coseismic pore pressure redistribution shows contrasting behavior. In the 1-D formalism, pore pressure changes are controlled by the pressure-dependent compressibility of the fluid. When in-plane processes are considered, this control on the pore pressure state becomes a secondary effect. Section 2.2. made clear that the fluid compressibility controls pore pressure in the 1D (or sealed subfault) case at depth (with temperature about 300°C Burnham et al., 1969). For a constant compressibility, frictional dilatancy is the only agent of co-seismic pore pressure decrease, and is not enough to reduce pore pressure to hydro- or sub-hydrostatic levels.

Consider slip on one subfault. If pore pressure is reduced to hydrostatic (or sub-hydrostatic) because of pressure-dependent compressibility, then it is still surrounded by a region of near-lithostatically pressured fluid which will diffuse into this co-seismically created sink. To illustrate what would happen, consider diffusion of a hydrostatically pressured cell surrounded by its high-pressured neighbors (Figure 3.7). For this calculation, numerical values for porosity and pore pressure were taken from SB92 (Table 3). The post-seismic porosity of the central cell is 8.7%, and the new pore pressure is hydrostatic (137 MPa at 14 km depth). Influx from the surrounding rock would equilibrate the sub-hydrostatic 54 MPa calculated by SB92 and the surrounding hydrostatic pore pressure. The porosity of the surrounding cells is 7.4% and the pore pressure is 270 MPa. The cells are $1.0 \text{ km} \times 0.5 \text{ km}$. The coseismic hydraulics of the 3D model is based on the assumption that the seals between the cells break due to seismic slip. Conceptually, we consider that the in-plane permeability switches from a low value (less than 10^{-19} m^2) to a high value of about 10^{-15} m^2 . A more accurate description would allow for a decrease in permeability within the cells, as a function of the distance to the boundary with the slipped cell. For small cell sizes, this effect is negligible. Figure 3.7 shows results of a finite difference calculation at different times, from 1 to 6 months. We approximate the

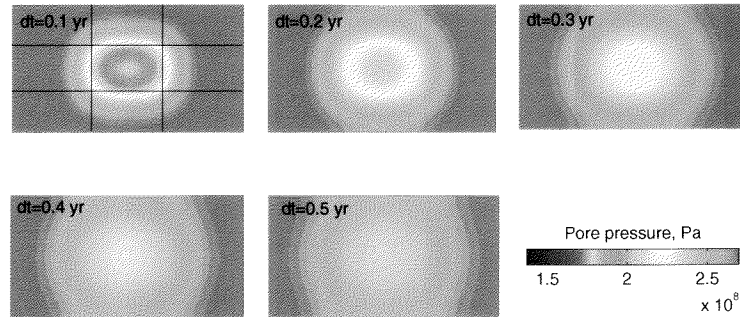


Figure 3.7: Pore pressure re-equilibration after failure (and dilatancy) of the middle cell. After 3 months, pore pressure is almost uniform, above 240 MPa. This value is close to the 255 MPa calculated with equation (3.18). Reasonably homogeneous pore pressure equilibrium is achieved after about 6 months.

low permeability outside of the slipped region by a no-flow boundary condition on the four sides of the model. Permeability inside the model is isotropic and is calculated as $k_o \phi^3$ (Brace, 1978). We chose $k_o = 10^{-11} \text{m}^2$ to get permeabilities about 10^{-15}m^2 in the equilibration area. Results show that after 1 month, pore pressure ranges already between 190 and 230 MPa in the slipped cell. After 3 months, pore pressure is almost uniform, above 240 MPa. This value is close to the 255 MPa calculated with equation (3.18). Reasonably homogeneous pore pressure equilibrium is achieved after about 6 months. This shows is that even if the feedback of pressure on compressibility drastically decreases the pore pressure after an earthquake, the importance of this process is reduced when in-plane processes are considered.

The ductile compaction mechanism is very efficient at increasing pore pressure (much more than tectonic loading, compare slopes of $\tau(t)$ and $P_f(t)$ on Figure 3.4, top), and rapidly results in overpressured faults. Pore pressure reduction results in very small changes because of in-plane equilibration. Results from a 3-D fault model (section 3.4) showed that the frictional strength thus stays low, and that within the time needed to rebuild the shear stress on the fault, pore pressure increases decrease the Coulomb failure stress, leading to shorter recurrence times of seismic events. The slip distributions of the model seismic events are not homogeneous (e.g., the whole fault plane does not rupture at once), and porosity creation happens only where slip occurred while compaction occurs for every subfault. When a subfault (or a group of subfaults) breaks, the porosity increases, but the seal between this (these) cells and their neighbors also breaks, allowing for pore pressure redistribution. As shown on Figure 3.7, the newly created porosity is filled with the fluid excess from the neighboring (not slipped) cells, impeding a large drop in pore pressure. This phenomenon yields to a slow homogenization of the properties of the fault at depth. Later in the simulations, the pore pressure and the slip distributions are very homogeneous.

Although pressure-dependent fluid compressibility has an effect on pore pressure, we conclude that the overpressured behavior of the fault is mostly a result of the 3D fault

hydraulics. This leads us to conclude that within mostly sealed faults, ductile compaction can only lead to overpressured faults. Although this type of fault exists (e.g. Faulkner and Rutter, 2001), it is not a general fault property, so alternative processes accounting for significant flow out of the fault zone are necessary. Potential candidates include the opening of veins and cracks towards the damaged zone that depend on the amount of seismic slip. This idea is supported by field and core observations (Chester et al., 1993; Tanaka et al., 2001). However, including these processes adds many more unconstrained parameters related to the time scales for healing of the cracks compared to time for fluids to flow out (Gratier et al., in press), and is beyond the scope of this paper.

3.5.2 Creep slip distribution

Fault creep is observed through measurements of offsets across active faults through time. Wesson (1988) reviews documented partially creeping strike-slip faults, including the San Andreas and the Calavera faults in California and faults in Guatemala, Turkey and China. Offsets of man-made features that cross faults as well as strains, tilts, and water level changes in wells have been associated with creep events. The depth to which surface fault creep persists is unclear. Inversion of instrumental tilt and strain measurements, and of short-baseline (< 5 km) continuous or frequent line-length measurements, suggest that episodic creep observed at the surface is, in most cases, confined to the uppermost few kilometers or less. On the other hand, aseismic slip is purported to accommodate plate motions at depths greater than the lower limit of earthquake occurrence.

Our model shows a higher creep rate at depth where shear stress is large, than at the surface. The ratio of creep slip to seismic slip at 14 km depth in accordance with the one obtained by SB92. However, the low creep rate near the surface is in disagreement with observations. Because of the low temperatures at shallow depth, thermally activated creep can not be the mechanism directly responsible for near-surface fault creep. Possible mechanisms for initiating stable slip in the upper 4 km include velocity strengthening as observed in laboratory friction experiments when slip is forced to occur within thick gouge (Marone and Scholz, 1988). If natural faults contain thick unconsolidated gouge within their shallow regions, they may exhibit stable slip within those regions and unstable slip below the depth at which the gouge becomes consolidated/indurated (and possibly thinner). For well-developed faults, comparisons of afterslip distribution (confined to the upper 3 km) and hypocenter distributions (4-14 km) are consistent with velocity strengthening at shallow depth, acting to arrest coseismic slip, resulting in a slip deficit that, upon relaxation, produces afterslip (e.g., 1979 Imperial Valley earthquake Marone and Scholz, 1988). For poorly developed faults, seismic slip occurs throughout the upper 6 km (see review in Marone and Scholz, 1988). In the near-surface region, the confining stress is low resulting in a lower grain contact areas than at depth, even for high roughness. This results in low peak strength (Barton, 1976) and large grain-size in the fault gouge. This could be accounted for by a lower intrinsic viscosity (Sleep and Blanpied, 1992).

A possible model improvement would be to add a dependency of the fault width-total slip relationship on confining stress (or depth) to get thicker fault zones in the upper part of the fault zone, and a dependency of the intrinsic viscosity η_i on total slip (e.g.,

accounting for grain-size diminution with slip, or with depth).

3.6 Conclusion and perspectives

We presented a 3D forward fault model including tectonics, fluids and stress transfer for ductile fault zones. Model faults have the properties of fault cores and are viscoelastic thin (decimeter- to meter-scale) vertical ductile bodies embedded in an elastic half-space and hydraulically isolated from the surrounding rocks by a narrow near-impermeable seal (a small leakage term is allowed). The conceptual model includes a simplification of the double porosity model described by Sleep and Blanpied (1992). We introduced the 1D formalism for ductile compaction and shear creep into the model of Fitzenz and Miller (2001), and showed that the fluid compressibility is the dominant effect controlling pore pressure changes in the close-to-1D case. In the 3-D model, slip on the fault is accounted for by viscous shear creep during interseismic periods and seismic slip when the Coulomb failure stress criterion is met. The hydraulic properties of the fault are determined by viscous compaction and frictional dilatancy (for porosity) and a toggle switch in-plane permeability allows for pore pressure redistribution after seismic events (Miller and Nur, 2000). We found that whatever fluid compressibility law we choose, model faults submitted to shear creep and ductile compaction will tend to develop overpressured compartments at depth (below 6 km), because of the heterogeneous slip distributions and in-plane coseismic flow within slipped patches (slipped cells and their neighbors).

We made a number of assumptions to derive the system of equations needed to handle the inclusion of a viscoelastic fault core in an elastic half-space, but more theoretical work is required to get a more general set of equations. Total stress P_T in a ductile layer should be determined analytically or numerically and should include a dependency in shear creep velocity.

The parameters used in our model are poorly constrained (porosities, intrinsic viscosity, fraction of the energy that goes into crack creation, width-slip relationship), revealing the need for more laboratory and field work.

Another issue is how fault zone structures evolve at depth (4-15 km). The structure chosen here is based on observations of the rocks taken from the Nojima fault zone. The depth reached by the boreholes is of the order of 1 km. What would be the picture at greater depth? We know from observations of vein fields (deemed related to faulting episodes that occurred at depths in the range 6 to 10 km, Cox, 1995) and exhumed fault zones that the processes (shear creep, evidences for high pore pressures, as well as coseismic dilatancy) are the same (see review by Sleep and Blanpied, 1992), but what about the width, the porosity and the permeability of each part of the fault zone? Moore et al. (1999) wrote "fault motion may shift to a completely new strand, leaving the old strand outside the damage zone of the new one" and in this case the old gouge layer would be gradually sealed. On the contrary, if the new site of localized shear stress is within the same fault strand, then "the old gouge layer would be limited to dilational fracturing and minor shearing". It would therefore be interesting to reset from time to time, randomly, the porosity to high initial values in the code to simulate a shift to a completely new strand. An additional point is aimed at emphasizing the need for a collection of models: all faults do not have this architecture (Rawling et al., 2001).

A final note. Since many faults have very long recurrence times, the overpressured faults easily activated in this model suggest that the out-of-plane hydraulics need to be understood and probably play a crucial role in the pore pressure regulation.

It remains to be seen if these new hydraulic features, coupled both to a better evaluation of the role of the damaged zone in the pore pressure cycles and to the evolution of fault systems following the evolution of the principal stresses (dynamical fault generation), can lead to realistic fault behavior in the framework of a regional model.

Acknowledgments The authors thank Mike Blanpied for many insightful comments on an early version of the manuscript, Keith Evans for stimulating discussions, Yuri Podladchikov for a decisive theory-afternoon, and Norm Sleep for clarifying parts of his model. This research was supported by the Swiss National Fund, program 2100-054121.98/1.

Chapter 4

Developing regional models of fault systems

The aim of this thesis work was not only to study the earthquake process, but also to develop a model that would help mechanistically assess seismic hazard. In this chapter, we present further model developments and a first step toward the development of regional models. We introduce interseismic in-plane permeability of each subfault as a function of porosity. Permeability is anisotropic, with the up-dip permeability greater than the permeability along strike. The permeabilities are then used in the interseismic in-plane fluid diffusion performed with a finite-difference algorithm. A constant hydraulic head condition is specified at the top of the faults. In a second part, we show simulation results for a regional model of a transpressional San Andreas Fault (SAF) in Central California. Maps of tectonic regimes and Coulomb failure stress provide constraints on the boundary conditions (e.g., tectonic loading). Taking into account the main result of Chapter 3, i.e., the rapid evolution toward an overpressured weak fault when ductile compaction acts on a fault zone, the fault system is loaded to strong faults before creep and ductile compaction are initiated on the faults. Model results include optimal tectonic regimes, stress orientations, and maximum shear stress maps at depth. We discuss the advantages of *CFS* maps in the prediction of the generation of new faults in the model space over ΔCFS maps obtained by a stress triggering approach. We also show the stress state and the slip on both faults, and seismicity timelines and frequency-magnitude statistics.

4.1 Model developments

In the forward fault interaction model presented in Chapter 2, the subfaults are completely sealed from the surrounding rock, both in-plane and out of plane. Chapter 3 introduced the notion of a mostly impermeable seal between the fault core and the surrounding rocks and we added a diffusion term to the pore pressure change rate for each subfault to account for the leakage of fluids out of the fault zone. Here, we acknowledge the fact that although being extremely low, the in-plane permeability in the fault core is not zero. In-plane interseismic fluid flow is therefore expected. Diffusion depends namely on fluid viscosity, pore pressure gradients, permeabilities, and distances. It is therefore not cell-size dependent, a major drawback acknowledged in the previous models. We present the interseismic in-plane permeability calculation and the finite-difference diffusion code we built in in appendix 4.3 and 4.4.

4.2 Constraints on tectonic loading and stress maps from a 3-dimensional forward fault interaction model including tectonics, fluids and stress transfer. Application to the Transpressional Big Bend area in Central California

This section is a paper in preparation.

Abstract

We present preliminary results from a 3-dimensional fault interaction model, with the fault system specified by the geometry and tectonics of the San Andreas Fault (SAF) system in Central California. Our aim is to target measurable properties in or around fault zones (e.g., pore pressures, seismicity patterns, stress orientation, surface strain, triggering, etc.), which may allow inferences on the stress state of fault systems, and model tectonic regimes and stress rotations in the surrounding crust. We use the forward model for earthquake generation on interacting faults of Fitzenz and Miller (2001) that incorporates the analytical solutions of Okada (85,92), GPS-constrained tectonic loading, and undrained poroelastic effects. Model faults are viscoelastic bodies mostly sealed from the surrounding rocks, subjected to ductile compaction and shear creep, embedded in an elastic half-space (Sleep and Blanpied, 1994, Sleep, 1995, Fitzenz and Miller, Submitted). Interseismic in-plane diffusion is also implemented.

The model fault system is centered at the Big Bend, and includes two 200 km-long plate-boundary right-lateral strike-slip faults (each discretized into multiple subfaults). The southern segment is oriented 20° with respect to the northern segment. Tectonic loading is decomposed into basal shear drag parallel to the northern plate boundary with a 35 mm yr^{-1} plate velocity, and East-West compression approximated by a vertical dislocation surface applied at the far-field boundary resulting in fault-normal compression rates in the model space about 3 mm.yr^{-1} . We find that overpressured compartments on model faults through ductile compaction are a necessary consequence of the tectonic loading, specifically where high normal stress acts on long straight fault segments. We show that a transpressive tectonic regime develops South-West of the model Big Bend as a result of the loading boundary conditions. Stress transfers from fault seismicity are shown to induce significant perturbations in the local stress tensor. Large earthquakes initiating on one fault occasionally trigger events on the other fault (coseismic interaction). Maps of maximum shear stress emphasize the need for dynamic generation of faults in further model developments. When considering large spatial and temporal scales, post-seismic relaxation will need to be introduced, e.g., as a time-dependent perturbation in the background stressing rate due to plate motion.

4.2.1 Introduction

Plate boundaries are often a zone of complex deformation over tens or hundreds kilometer wide, leading to complex tectonic regime distributions. Knowledge of the forces, e.g., stresses, acting on these fault systems is essential to understand the mechanics of its deformation. Borehole measurements can give information on the subsurface stress state (Brereton and Muller, 1991; Zoback and Healy, 1992; Tsukahara et al., 1996; Ikeda et al., 2001) and stress orientations at seismogenic depths (Townend and Zoback, 2001, Hardbeck and Hauksson, 1999, 2001; Provost and Houston, 2001) can be determined from earthquake focal mechanisms. Consequently, no direct evaluation of absolute stress values can be determined between 5 and 20 km depth, that is at the focal depth of most earthquakes. However, spatial patterns and temporal evolution of both stress orientation and absolute magnitude are needed to study earthquake mechanics. Together, they indicate whether the spatially complex faulting results from a complex stress state or from

heterogeneous fault properties (e.g., lithology, geometry, friction) and control the stresses acting on the faults. In this context, we present a forward fault interaction model allowing the test of boundary conditions (e.g., tectonic loading) and the investigation of the time-evolution of stress patterns around active faults. Starting from the fluid-controlled forward fault interaction model of Fitzenz and Miller (2001), we implement shear creep and ductile compaction (Fitzenz and Miller, Submitted to *Geophysical Journal International* 2002), as well as in-plane interseismic fluid diffusion and out of plane leakage. We show first simulation results from a regional model of a transpressional San Andreas Fault (SAF) in Central California. Taking into account the main result of (Fitzenz and Miller, Submitted to *Geophysical Journal International* 2002), i.e., the rapid evolution toward an overpressured weak fault when ductile compaction acts on a fault zone, the model faults were loaded to strong faults before any creep and ductile compaction were introduced. Model results include maps of tectonic regimes, stress orientation, and Coulomb failure stress and maximum shear stress at depth. We also show the stress state and the slip on both faults, as well as seismicity timelines and frequency-magnitude statistics.

4.2.2 Tectonic set-up

The model fault system is centered at the Big Bend, and includes two large strike-slip faults; a 200 km, right-lateral segment of the SAF to the North, and a 200 km-long right-lateral segment of the SAF to the South. Tectonic loading is decomposed into basal shear drag parallel to the plate boundary with a 35 mm yr^{-1} plate velocity, and East-West compression approximated by a vertical dislocation surface applied at the far-field boundary resulting in fault-normal compression rates in the model space about 3 mm yr^{-1} (Argus and Gordon, 1991; Prescott et al., 2001).

The validity of the model set-up is tested with maps of calculated tectonic regimes and Coulomb failure stress after 10,000 years of tectonic loading alone. Tectonic regimes are obtained by combining the vertical stress and the ratio $R = \frac{\sigma_2 - \sigma_3}{\sigma_1 - \sigma_3}$, where σ_1 , σ_2 , and σ_3 are the principal stresses (more details are given in the evolved case below). Figure 4.2 shows that the bent plate boundary lies in a pure strike-slip regime. However, a compressive to transpressive regime develops west of the southern part of the plate boundary (for $x > 0$), recalling the transverse ranges and San Gabriel compressions. A large area east of the plate boundary (for $x > 0$) also exhibits a compressive regime. In the crust (e.g., intact rock), friction values are high (e.g., $\mu = 0.9$, Byerlee, 1978) and cohesion is chosen as $c = 20 \text{ MPa}$. Pore pressure is hydrostatic (Townend and Zoback, 2000). The Coulomb failure stress ($CFS = \tau - \mu\sigma_{eff} - c$) was calculated on optimally oriented planes for new fractures and is shown in Figure 4.3. White corresponds to $CFS = 0$. The two model faults, representing two segments of the San Andreas Fault, are shown to be the first faults to accumulate enough stresses to reach the failure criterion. The high values of CFS (up to $7 \times 10^7 \text{ Pa}$) only reflects that these faults would be created well before 10,000 years of plate motion. Using these validated boundary conditions, we started a 4050 year simulation with specified faults as shown on Figure 4.3.

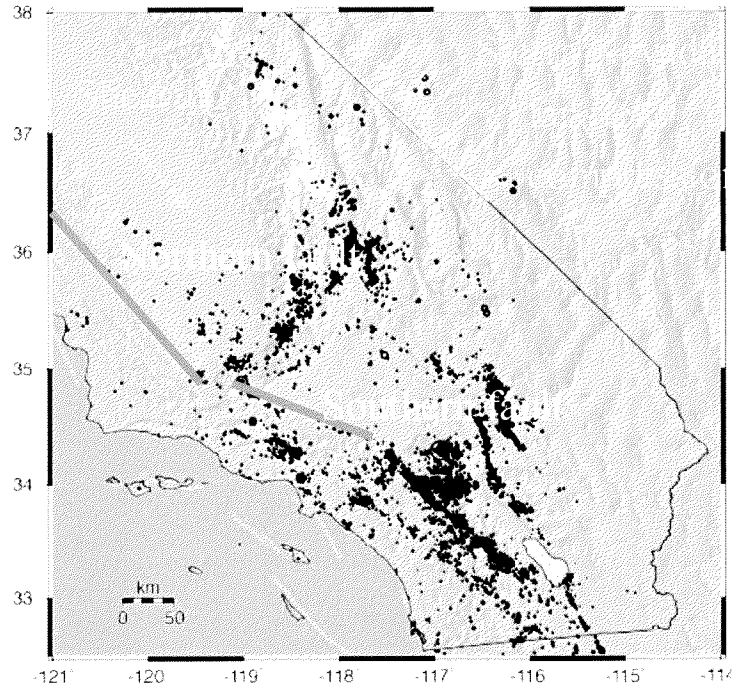


Figure 1. Earthquakes recorded by SCSN/TriNet

Figure 4.1: Seismotectonic map of Southern California showing the major fault traces (red lines) and the seismicity between October 2000 and September 2001 (recorded by SCSN/TriNet). The yellow arrows show the boundary conditions for our model, the basal shear drag parallel to the Northern part of the San Andreas fault and the far-field compression perpendicular to it. The thick red lines show the two segment of the San Andreas fault included in our calculations.

4.2.3 Initial loading conditions

In the initial loading phase, the model includes stress transfer, poroelastic effects, interseismic compaction rate (random around $3 \cdot 10^{-6} \text{ yr}^{-1}$) and coseismic pore pressure redistribution (Fitzenz and Miller, 2001). It also includes interseismic anisotropic in-plane diffusion.

Permeabilities are calculated from porosities using (Brace, 1977):

$$k = k_o \phi^3, \quad (4.1)$$

where k is the permeability, ϕ is the porosity and k_o is proportional to the hydraulic radius. We keep k_o constant during interseismic periods. Faulkner and Rutter (2001) measured fault gouge permeabilities of $\sim 10^{-18} \text{ m}^2$ in a direction parallel to the fault plane in the Carboneras (Spain) strike-slip fault. They also measured an in-plane anisotropy. The vertical permeability (k_z) is more than one order of magnitude higher than the horizontal permeability (k_x). Rawling et al (2001) review fault gouge permeabilities from $\sim 10^{-20} \text{ m}^2$ to $\sim 10^{-19} \text{ m}^2$. Assuming that in-plane permeability is anisotropic and a cubic function of porosity, we get $k_x = k_{ox} \phi^3$ and $k_z = k_{oz} \phi^3$, with $k_{ox} = 10^{-15} \text{ m}^2 < k_{oz} = 10^{-13} \text{ m}^2$.

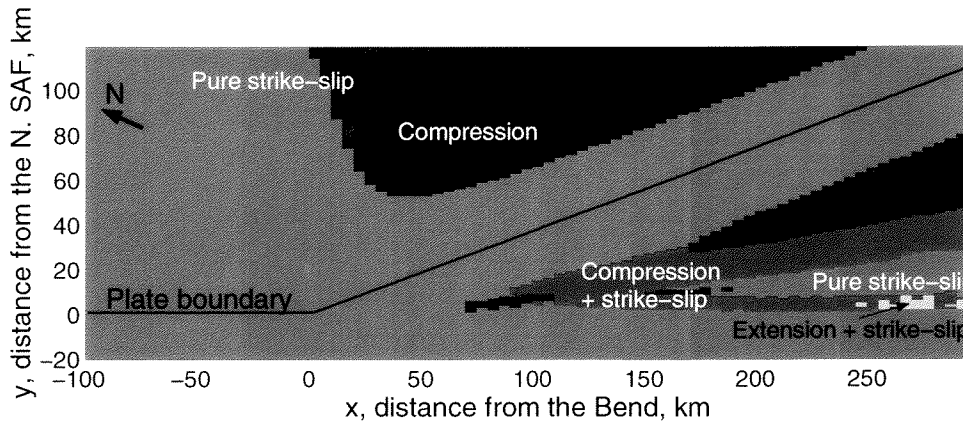


Figure 4.2: Tectonic regimes calculated at 8.5 km depth for 10,000 years of basal shear drag and far field compression. The plate boundary lies in a pure strike-slip regime, while transpression is shown to develop south west of the Bend (e.g., transverse ranges, San Gabriel belt). The y axis shows the distance to the Northern segment of the San Andreas Fault (N. SAF).

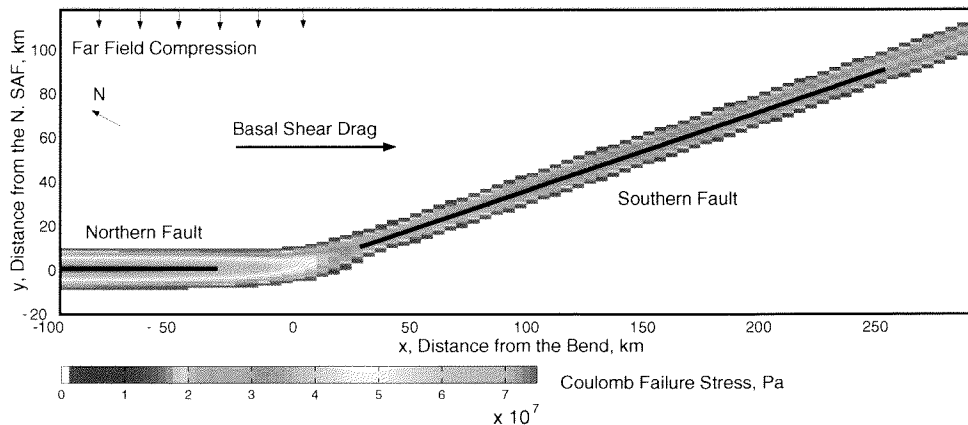


Figure 4.3: Geometry of the model fault system and boundary conditions and Coulomb failure stress (CFS) calculated at 8.5 km depth due to 10,000 yr of tectonic loading. The two model faults, representing two segments of the San Andreas Fault, are shown to be the first faults to accumulate enough stresses to reach the failure criterion. The white color corresponds to $CFS = 0$.

The interseismic permeabilities of the model subfaults range from $\sim 10^{-21}$ to $\sim 10^{-19}$ m², depending on the evolving porosity. These values are used in a finite-difference algorithm to calculate in-plane interseismic diffusion.

4.2.4 Ductile compaction and shear creep

After model conditioning, the fault properties are those of a ductile fault core, hydraulically disconnected from the surrounding rocks by a quasi-impermeable narrow seal between the fault core. A small diffusive leakage out of the fault zone during interseismic periods is expected. Ductile compaction and leakage out of the fault zone are handled as described in (Fitzenz and Miller, submitted). The total interseismic pore pressure change rate is:

$$\frac{\partial P_f}{\partial t} = -\frac{(P_f - \sigma_n)}{\beta_f \phi} \frac{2}{\eta_i} \left[\frac{13 + 4\phi}{63 + 36\phi} \right] \left[\frac{\phi - \phi_{\min}}{\phi_{\max} - \phi_{\min}} \right]^a - \frac{P_f - P_h}{t_h} \quad (4.2)$$

where P_f pore pressure and σ_n normal stress within the fault core, η_i is the intrinsic viscosity of the grains, P_h is the hydrostatic pore pressure of the surrounding rocks and t_h is the out-of plane diffusion time. For simplicity, we keep the maximum porosity constant $\phi_{\max} = 9\%$. The shear creep velocity V is

$$V = \tau W \frac{13 + 4\phi}{9\eta_i}, \quad (4.3)$$

where W is the fault core width. Note that V is the velocity of one wall of the fault zone with respect to the other wall. Stress transfer from creep slip is calculated using Okada's (1992) analytical solutions every 50 years to save computation time. Where not otherwise specified, the model parameters are given in Table 3.1 (Fitzenz and Miller, submitted).

4.2.5 Evolved stress state and seismicity on the model faults

The time evolution of the stress state on both faults is shown on Figure 4.4 for the northern fault and on Figure 4.5 for the southern fault. The seismicity timelines and statistics are shown on Figure 4.6. The three main phases in the model fault history are a stress build-up phase (\sim the first 1800 yr), a phase of self-organization of the stress state, evidenced by the occurrence of the first large ruptures (until $t \sim 3000$ yr), and a phase of fault weakening starting soon after the onset of ductile compaction. On the Northern fault, the first phase is characterized by a steady increase in shear stress τ from tectonic loading, and a decrease in effective stress σ_{eff} , and an increase in overpressure factor λ due to pore compaction (Figure 4.4). On the Southern fault, λ and σ_{eff} appear to remain constant. Due to the oblique orientation of the fault with respect to the basal shear drag, pore pressure increase from compaction are counterbalanced by the tectonic normal stress increase. The seismicity (Figure 4.6) is low on both faults.

The second phase shows an increase in seismicity and the first large events ($M_w > 7$) occur at $t \sim 2500$ yr and $t \sim 3000$ yr on the Northern and the Southern fault, respectively. The advance of the Northern fault is related to its lower frictional strength (e.g., lower σ_{eff}).

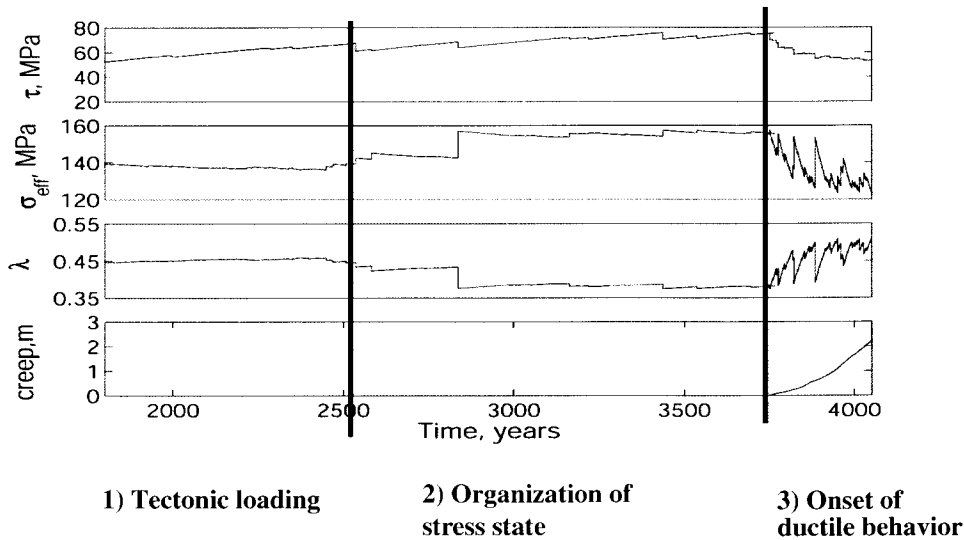


Figure 4.4: Time evolution of the average properties on the Northern strike-slip fault; from top to bottom, shear stress, effective stress, the degree of overpressure λ and the amount of creep slip. The first part ($t = 0$ to $t \sim 2500$ yr) is the stress build-up phase. Seismicity then initiates, and the first large event ($t \sim 3000$ yr) induce large drops in pore pressure. Creep and ductile compaction initiate at $t = 3750$ yr. The pore pressure increase rate is much larger than the shear increase rate. Although the first large events allow the pore pressure to drop back to hydrostatic levels, ductile compaction leads to a progressive weakening of the fault.

At $t = 3750$ yr, the initial loading phase stops and both faults sustain high shear stresses (i.e., strong faults). Shear creep and ductile compaction are introduced. The high effective stresses lead to pore pressure increase rates (equation 4.2) much larger than the shear stress increase rate, promoted by tectonic loading but impeded by shear creep. The combined effects of creep and compaction lead to fault weakening. During this phase, the density of medium size events ($4.5 < M_w < 6$) increases dramatically, very rapidly on the Southern fault and more progressively on the Northern fault (Figure 4.6). On the Northern fault, large events reaching the surface allow for large pore pressure drops, leading to a fault behavior comparable to that obtained in the 1-D fault model of Sleep and Blanpied (1992). However, when the rupture does not reach the surface, fluids can not be expelled, overpressures are maintained, and the fault evolves to a weak fault.

Note the larger creep rate on the Northern fault (7.6 mm yr^{-1}) than on the Southern fault (5 mm yr^{-1}). These are values averaged over the fault planes. Creep slip is maximum at depth, and at 18 km depth the accumulated creep slip over 300 yr yields average creep rates on the order of plate velocity.

The stress and pore pressure state was also monitored on a blind dipping fault oriented 25° to the Northern fault between $x = -200$ and $x = -109$ km. Thrusting appears to be a later time feature.

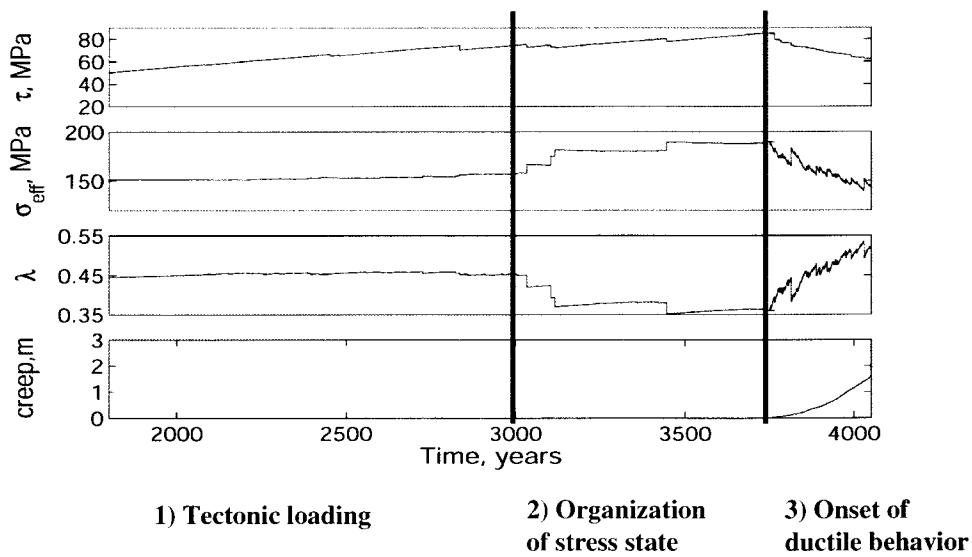


Figure 4.5: Time evolution of the average properties on the Southern strike-slip fault. Same as Figure 4.4. Because of the 20° angle between the fault strike and plate motion, the normal stress build-up rate is larger than in the previous case, initially leading to a stronger fault. As ductile compaction initiates, the larger effective stress leads to a larger compaction rate and faster overpressurization of the fault. The fault can not sustain high shear stresses anymore and evolves to a weaker fault. The average amount of creep is $2/3$ the creep slip on the northern fault.

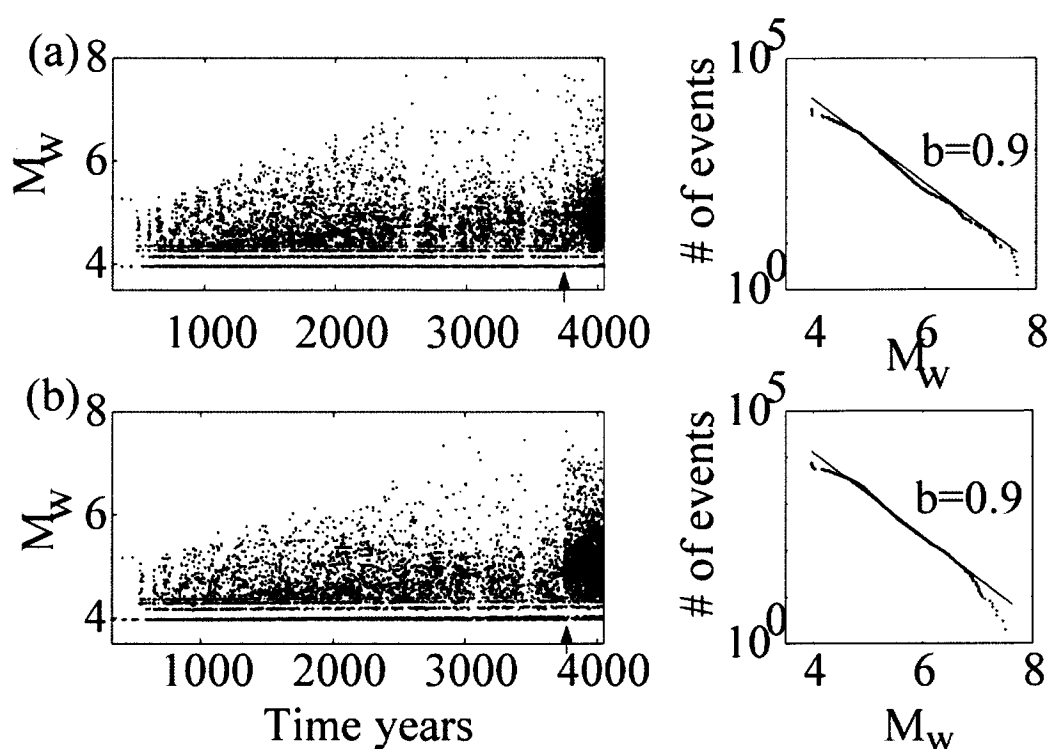


Figure 4.6: Seismicity timelines and frequency-magnitude statistics. (a) for the northern strike slip fault; (b) for the southern strike-slip fault. The first large events occur after $t = 2500$ yr. The arrows show the onset of shear creep and ductile compaction at $t = 3750$ yr. The density of the seismicity reflects the strength of the faults shown in figures 4.4 and 4.5. Thus, it doesn't increase immediately significantly on the first fault since it recovers a high strength after the first large earthquakes occurring after $t = 3750$ yr. The density of medium size events ($4.5 < M_w < 6$) increases dramatically on the second fault. Both faults exhibit Gutenberg-Richter laws with a b-value of 0.9 (shown by the straight line).

4.2.6 Resulting regional tectonic evolution

The bend in the plate boundary leads to a complex distribution of deformation in the crust, as shown in section 4.2.2. The evolution of the stress state and the seismicity on the two faults added perturbations to the local stress tensor. Surface deformation vectors are shown on Figure 4.7. Averaged over 4050 yr, the maximum surface strain rate along x is 32 mm yr^{-1} far from the plate boundary, reflecting the basal shear drag.

The relative variation of principal stresses is expressed by the ratio $R = \frac{\sigma_2 - \sigma_3}{\sigma_1 - \sigma_3}$. R can vary between 0 and 1. Combined with the vertical principal stress, R determines the tectonic regime prevailing in the area. In most of the model space, σ_2 is vertical, indicating a strike-slip environment. In this case, $R \sim 0$ indicates a reverse/strike-slip environment and $R = 0.5$ means pure strike-slip. Figure 4.7 shows the spatial distribution of R calculated at 8.5 km depth. For $x > 80$ km, a large area west of the fault exhibits σ_3 vertical, indicating a compressional environment, with $R \sim 0$ (reverse/strike-slip) or $R \sim 1$ (constrictive). Locally on the second (southern) model fault the vertical stress is also σ_3 , leading to a transpressive regime close to the fault. Lastly, for $x \sim 260$ km and $y \sim 0$, local transtensive environments dominate (e.g., σ_1 vertical and $R \sim 1$).

The maximum shear stress and the orientations of σ_1 are shown on Figure 4.8. Shear stress is maximum along the plate boundary in a 20 km wide zone (~ 70 MPa) and is largely perturbed on the Southern fault. Although the level of shear stress is reduced on both sides of the fault, stress transfer from previous earthquakes locally increased the maximum shear stress near the fault up to 200 MPa. In the same manner, σ_1 is consistently oriented $\sim 45^\circ$ to the Northern fault, and $\sim 55^\circ$ to the Southern fault in a 20 km wide band. However, it locally rotates to be almost perpendicular to the fault strike near the southern fault. No such perturbation is observed on other parts of the faults, suggesting that the stress rotation are an ephemeral result of local seismicity. Further studies should investigate the time evolution of these patterns, focusing on the effect of the on-going tectonic loading and on the effect of seismic slip on adjacent fault segments. Figure 4.8 shows that no significant shear stress has accumulated of fault at this time in the model. However, we can investigate how this two-fault system would evolve with time (see Figure 4.9 for reference of what the Big Bend region really looks like (!)). If this loading conditions were maintained for thousands or million years, new faults would develop. Optimal orientations for failure at $t = 4050$ years already prescribe the initiation of a left-lateral strike-slip fault analog to the Garlock fault, and thrust belts analog to the transverse ranges and the San Gabriel thrust belt (Figure 4.10).

4.2.7 Fluids

Pore pressures are coseismically redistributed within all the slipped cells and their neighbors when the system reaches stress equilibrium. This large-scale redistribution, coupled to the constant head boundary condition at the top of the fault, allows large ruptures to decrease pore pressures on the faults more significantly than the incremental redistribution used in Fitzenz and Miller (submitted). Figure 4.11 shows compartments of low pore pressure where previous ruptures reached the top layer. For a hydrostatic fluid pressure and a normal stress equal to the lithostatic stress, the degree of overpressure $\lambda = P_f/\sigma_n = 0.37$ if the rock density is 2700 kg m^{-3} . The southern fault (b) exhibits

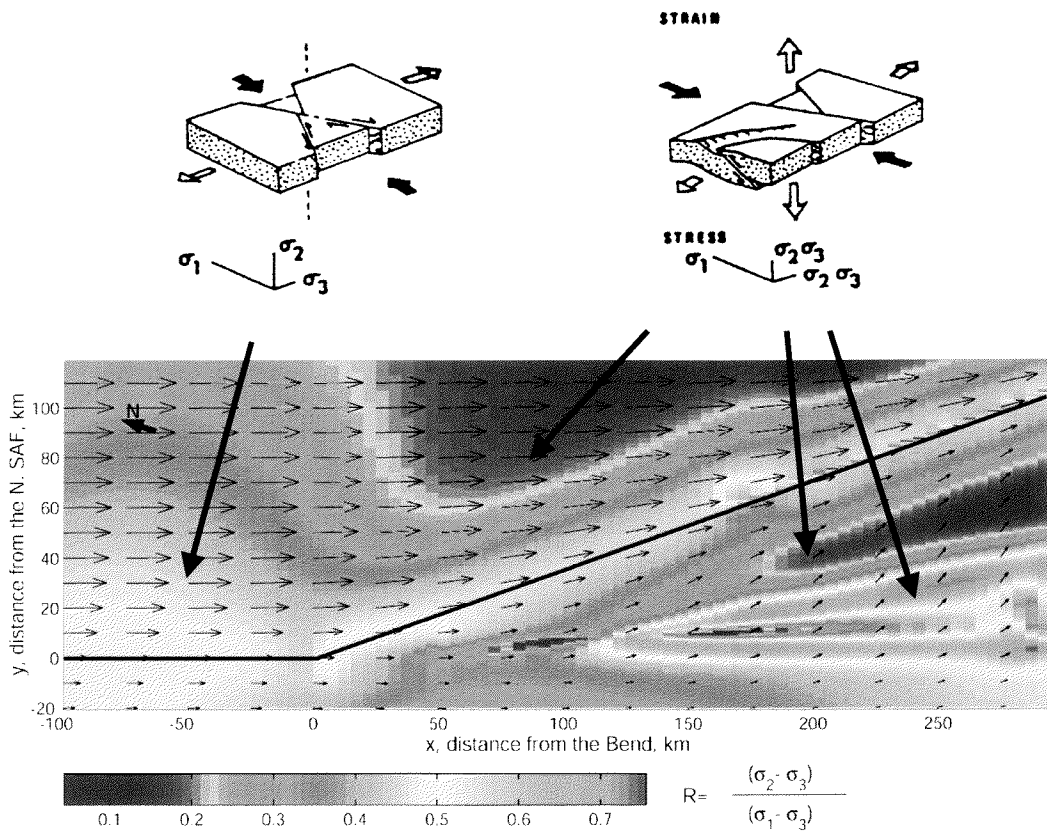


Figure 4.7: Surface deformation (arrows) and spatial variation of principal stresses (R) at $t = 4050$ yr. The maximum surface deformation rate along x is 32 mm yr^{-1} far from the plate boundary and along y 7 mm yr^{-1} . R , calculated at 8.5 km depth, shows values between 0.05 and 0.75 indicating a large spatial heterogeneity of the stress tensor (see text for details).

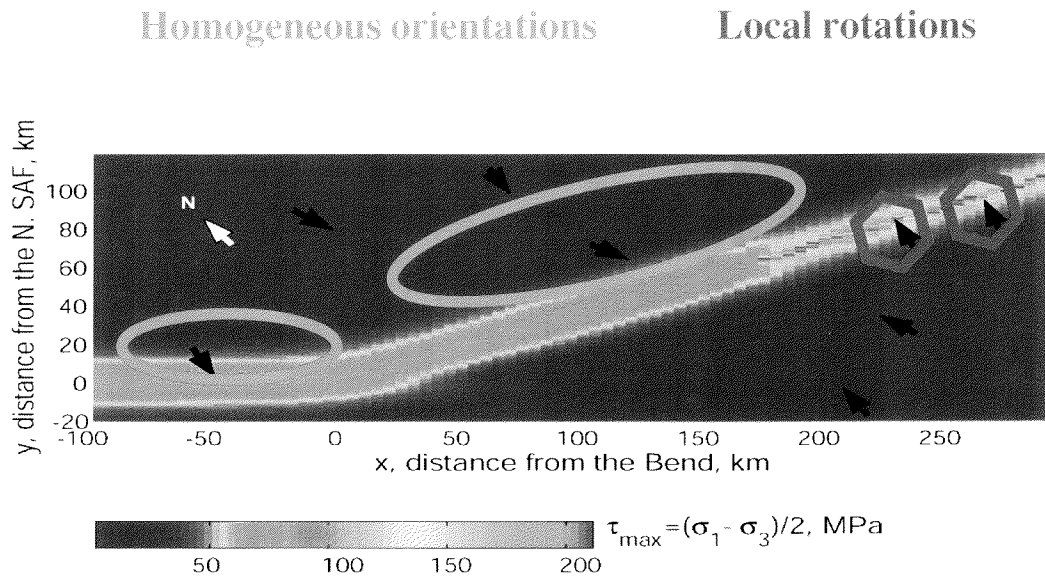


Figure 4.8: Maximum shear stress and orientation of σ_1 (black arrows). Shear stress is maximum along the plate boundary in a 20 km wide zone (~ 70 MPa) and is largely perturbed on the Southern fault. Although the level of shear stress is reduced on both sides of the fault, stress transfer from previous earthquakes locally increased the maximum shear stress near the fault up to 200 MPa. In the same manner, σ_1 is consistently oriented $\sim 45^\circ$ to the Northern fault, and $\sim 55^\circ$ to the Southern fault in a 20 km wide band. However, it locally rotates to be almost perpendicular to the fault strike near the southern fault.

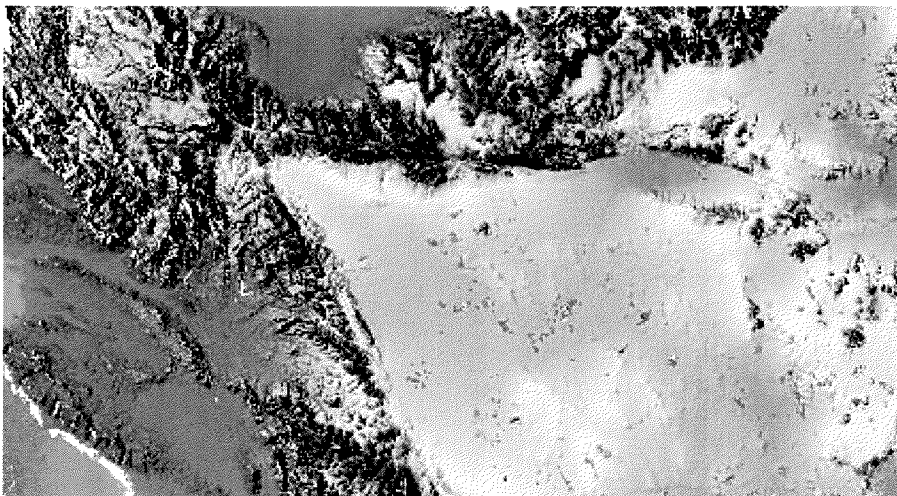


Figure 4.9: Topographic view of the Big Bend (source: JPL)

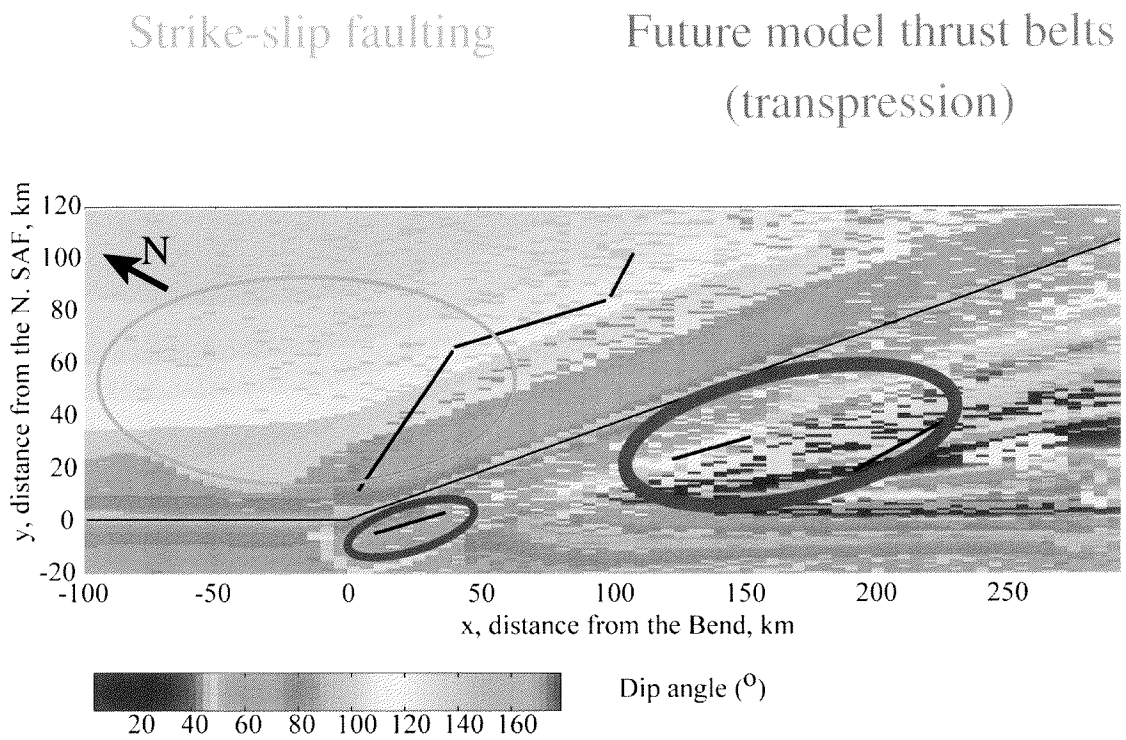


Figure 4.10: Optimal orientation for failure at $t = 4050$ yr calculated at 8.5 km depth. The colors show the dip angle of the optimally oriented planes and the lines show the strike of some noticeable features. The subvertical strike-slip fault shown east of the Bend represents an analog to the Garlock fault, although this fault orientation prevails in the whole area within the red oval. The thrust faults that would develop in the model west of the Bend are analog to the transverse ranges and the San Gabriel thrust belt.

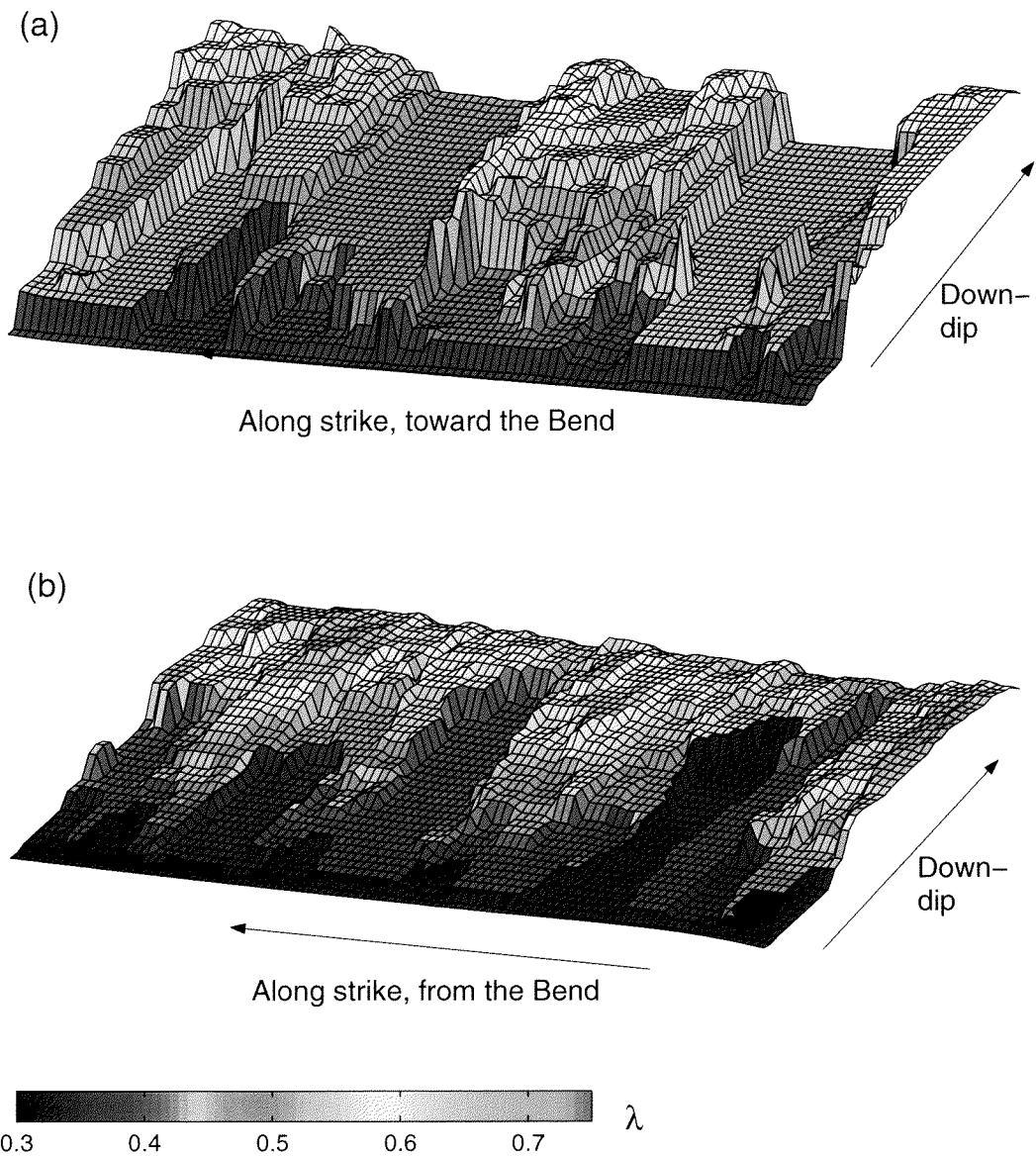


Figure 4.11: Degree of overpressure λ at $t = 4050$ yr (a) on the northern fault, (b) on the southern fault. The second fault is more overpressured than the first one. In both cases, large compartments of low pore pressure (hydrostatic levels) are generated by ruptures that reached the top layer constant head boundary condition.

$\lambda < 0.37$ in several compartments because of a normal stress higher than lithostatic.

A major shortcoming of the model in-plane fault hydraulics (Fitzenz and Miller, submitted) was the cell-size dependency of the results. In-plane diffusion now integrates the length scale of the model subfaults in the pore pressure redistribution. It introduces a small deviation from the quasi-static approach but even though the effects of the diffusion are observable on the pore pressure distributions (e.g., the smooth slopes of λ toward the surface), the calculation of the time steps is still valid.

Ductile compaction is shown to lead to a significant fault weakening within 300 years. Further studies should therefore investigate alternative pore pressure reduction mechanisms, such as coseismic leakage toward the damage zone, as discussed in (Fitzenz and Miller, submitted).

4.2.8 Conclusion

We showed first results of a regional model of the Central San Andreas fault near Big Bend. The model includes tectonic loading, fault zone hydraulics and stress transfer. Maps of Coulomb failure stress and tectonic regimes helped constraining the boundary conditions. We show that when no out-of-plane coseismic flow is allowed, the introduction of shear creep and ductile compaction on initially strong faults induces a rapid increase in pore pressure and leads to fault weakening.

Maps of the evolved maximum shear stress and σ_1 orientations after ~ 4000 years of simulation show that the fundamental basis for inverting a group of fault slip observations or focal mechanisms to infer stress orientations, i.e., the assumption that slip in each event occurred within a uniform stress field (see review in Townend and Zoback, 2001) is not satisfied in the model area. Townend and Zoback (2001) expressed doubts about the homogeneity of the stress field in the Fort Tejon area, where the SAF exhibits a $c.20^\circ$ change of strike. On the other hand, Hardebeck and Hauksson (1999) chose to invert together focal mechanisms separated by as much as 80 km in that same Big Bend area.

Another debate is whether large earthquakes can trigger stress rotations. Stress perturbations due to seismicity on the model faults are significant and are localized in a very narrow zone (± 5 km). They are not persistent with time.

Regional fault models prove to be a powerful tool. The proposed procedure to build such a model consists of 1) infer possible boundary conditions (in the form of dislocations) by confronting optimal orientation and absolute Coulomb failure stress of fault planes with actual fault map for different model tectonic loading geometries; 2) adopt this tectonic loading and a simplified fault system in a forward model including tectonic loading, fluids, and stress transfer; 3) analyze seismicity results and stress state on the model faults and calculate maps of the maximum and minimum horizontal stresses in the model area, including effects from tectonic loading, the isotropic overburden and the local seismicity, at different times and at different depths; 4) compare stress orientations before and after a large earthquake; compare with changes in the fault pore pressure distributions; 5) confront these maps with similar maps obtained from focal mechanism inversion; 6) feedback of the results of these comparisons into the model, e.g., tectonic loading, fault geometry, fault zone hydraulics. Considering the long time-scale and the large spatial scale of such a study, a coupling of our model to postseismic relaxation codes would be needed. This

could be achieved via evolving boundary conditions (e.g., basal drag) calculated with a viscous lower crust, after each large earthquake occurring in or at the boundaries of the modeled fault system.

4.3 Appendix A: permeability evaluation

Porosity of model fault cores is monitored in the forward models we developed. Applying interseismic fluid diffusion requires the knowledge of the permeability tensor for each subfault during quiescence. We present here a discussion on permeability anisotropy and porosity-permeability relationships.

Faulkner and Rutter (2001) measured oriented fault gouge permeabilities in the Carboneras (Spain) strike-slip fault. They show a significant anisotropy to three orders of magnitude: $\sim 10^{-18}$ m² in a direction parallel to the fault plane and $\sim 10^{-21}$ m² perpendicular to the fault plane. They also measured an in-plane anisotropy. The vertical permeability (k_z) is more than one order of magnitude higher than the horizontal permeability (k_x).

Gueguen and Dienes (1989) show that if the permeability is mostly due to fissure porosity and assuming a constant pore density, the permeability is a cubic function of porosity (i.e., $k \propto \phi^3$). Lockner and Evans (1995) evaluated channel and pore volumes of hot-pressed quartz using an electrical conductivity-porosity model and evaluated the porosity sensibility of permeability using Poiseuille formula. They find $k \propto \phi^{3.8}$. We assume here the permeability to be dependent on porosity through the relation (Brace, 1977):

$$k = k_o \phi^3, \quad (4.4)$$

where k is the permeability, ϕ is the porosity and k_o is proportional to the hydraulic radius. We keep k_o constant during interseismic periods. Assuming that in-plane permeability is anisotropic and a cubic function of porosity, we get $k_x = k_{ox} \phi^3$ and $k_z = k_{oz} \phi^3$, with $k_{ox} < k_{oz}$.

4.4 Appendix B: Interseismic in-plane fluid diffusion

The 2-dimensional diffusion equation for the anisotropic permeability case is

$$\frac{\partial P_f}{\partial t} = \frac{1}{\eta_f \beta_f} \left[k_x \frac{\partial^2 P_f}{\partial x^2} + k_z \frac{\partial^2 P_f}{\partial z^2} \right] \quad (4.5)$$

where P_f is pore pressure, η_f and β_f are the viscosity and compressibility of the fluid, respectively. The subscript x refers to the coordinate along strike and z is the up-dip coordinate. We specify no-flow boundary conditions on the fault except at the top where the pore pressure is maintained at the hydrostatic value.

For completeness, we give here a short summary of the derivation of the finite difference algorithm we use to solve the in-plane diffusion equation. We show the method for the 1-dimensional case $\frac{\partial P_f}{\partial t} = \frac{k_x}{\eta_f \beta_f} \frac{\partial^2 P_f}{\partial x^2}$. Time and spatial coordinates are discretized in $(t_1, \dots, t_n, t_{n+1})$ and $(x_1, \dots, x_n, x_{n+1})$, respectively. We apply a Taylor expansion at the points defined in time and space by (t_n, x_{i+1}) and (t_n, x_{i-1}) :

$$\begin{aligned} P_f(t_n, x_{i+1}) &= P_f(t_n, x_i) + \Delta x \frac{\partial P_f}{\partial x}(t_n, x_i) + \frac{(\Delta x)^2}{2} \frac{\partial^2 P_f}{\partial x^2}(t_n, x_i) + O((\Delta x)^2) \quad (a) \\ P_f(t_n, x_{i-1}) &= P_f(t_n, x_i) - \Delta x \frac{\partial P_f}{\partial x}(t_n, x_i) + \frac{(\Delta x)^2}{2} \frac{\partial^2 P_f}{\partial x^2}(t_n, x_i) + O((\Delta x)^2) \quad (b) \end{aligned} \quad (4.6)$$

where Δx is the distance between consecutive nodes (i.e., $x_{i+1} - x_i$). Adding (a) and (b) yields:

$$P_f(t_n, x_{i+1}) + P_f(t_n, x_{i-1}) = 2P_f(t_n, x_i) + (\Delta x)^2 \frac{\partial^2 P_f}{\partial x^2}(t_n, x_i) + O((\Delta x)^2). \quad (4.7)$$

Rearranging equation (4.7):

$$\frac{\partial^2 P_f}{\partial x^2}(t_n, x_i) = \frac{P_f(t_n, x_{i-1}) - 2P_f(t_n, x_i) + P_f(t_n, x_{i+1}))}{(\Delta x)^2} + O((\Delta x)^2). \quad (4.8)$$

In the same manner, the time derivative of the pressure in x_i is

$$\frac{\partial P_f}{\partial t}(t_n, x_i) = \frac{P_f(t_{n+1}, x_i) - P_f(t_n, x_i)}{\Delta t} + O(\Delta t). \quad (4.9)$$

Combining (4.8) and (4.9), the diffusion equation is:

$$P_f(t_{n+1}, x_i) = P_f(t_n, x_i) + G_x(P_f(t_n, x_{i-1}) - 2P_f(t_n, x_i) + P_f(t_n, x_{i+1})) \quad (4.10)$$

where $G_x = \frac{\Delta t}{(\Delta x)^2} \frac{k_x}{\eta_f \beta_f}$.

Following the same logic, the solution to the 2-dimensional problem is:

$$\begin{aligned} P_f(t_{n+1}, x_i, z_j) &= P_f(t_n, x_i, z_j) \\ &+ G_x(P_f(t_n, x_{i-1}, z_j) - 2P_f(t_n, x_i, z_j) + P_f(t_n, x_{i+1}, z_j)) \\ &+ G_z(P_f(t_n, x_i, z_{j-1}) - 2P_f(t_n, x_i, z_j) + P_f(t_n, x_i, z_{j+1})) \end{aligned} \quad (4.11)$$

with $G_z = \frac{\Delta t}{(\Delta z)^2} \frac{k_z}{\eta_f \beta_f}$. The permeability between two nodes is calculated as the average of the permeability of each node, for both directions of fluid flow:

$$\begin{cases} \text{Between } (x_{i-1}, z_j) \text{ and } (x_i, z_j), & k_x = k_{ox} \frac{\phi(x_{i-1}, z_j)^3 + \phi(x_i, z_j)^3}{2} \\ \text{Between } (x_i, z_{j-1}) \text{ and } (x_i, z_j), & k_z = k_{oz} \frac{\phi(x_i, z_{j-1})^3 + \phi(x_i, z_j)^3}{2} \end{cases} \quad (4.12)$$

and equation (4.11) is modified accordingly.

Chapter 5

Conclusions and perspectives

The reader is referred to the different chapters for detailed conclusions concerning each study.

5.1 Summary of the principal results

We developed and used a set of modular, flexible, physics-based forward fault models as a tool to investigate the dominant physical and chemical processes at work in the earthquake process. The results of this study form the foundation for developing time-forward mechanistic assessment of seismic hazard for large-scale potentially destructive fault systems.

5.1.1 From semi-forward stress transfer to a fluid-controlled forward model

We developed a stress transfer model using the analytical solutions giving the internal displacement field due to a finite dislocation in an elastic half-space in the framework of the stress transfer theory. Using the slip distribution inverted for the Izmit earthquake, we investigated how the main event changed the proximity to failure on the surrounding optimally oriented planes. We also compared maps of volumetric strain and Coulomb failure stress changes with the aftershock distribution and the location of the hypocenter of the Duce earthquake which stroke four months later. The latter was in a zone of increased proximity to failure. However, no significant conclusion could be drawn about what drives aftershocks, namely because of the limited knowledge on the regional stress and on the pore pressure state, and due to the lack of reliably relocated aftershocks. The complexity of the stress transfer patterns near the fault, reflecting both the changes in fault strike and the heterogeneity of the slip on the main fault, defined regions of enhanced proximity to failure (or the opposite) on the scale of the error on the aftershock location. The limits of this semi-forward study pointed to the need for a forward 3-dimensional fluid-controlled fault model, in which the local stress tensor is determined by both the tectonic loading and the seismicity. The pore pressure is monitored and fault interaction can be investigated. The construction and simulation results of such a model was presented in Chapter 2. Although the model leads to slip and stress distributions and seismicity statistics in general agreement with observation, the development of pore pressure compartments and the significant role of poroelastic effects in fault interaction pointed to the need for better constrained fault hydraulics.

5.1.2 Rheology and hydraulics of fault zones

A model fault having properties of a ductile fault core was considered and shear creep and ductile compaction were introduced in the 3-D forward model (Chapter 3). We showed the development of weak overpressured faults as a result of ductile compaction and small-scale coseismic pore pressure redistribution, whether the fluid compressibility is pressure dependent or kept constant. Because many faults exhibit creep slip, which are not purported to be weak or overpressured, we propose two alternative mechanisms

to regulate the pore pressure cycle in fault zones. The first one is related to the role of the highly permeable damage zone (Tanaka et al, 2001) and the second relates to the in-plane pore pressure redistribution length-scale. Because such hypotheses have to be tested against data, we built a regional model.

5.1.3 Regional model

Chapter 4 shows first results from a regional model of the transpressional San Andreas Fault near the Big Bend (California). To avoid cell-size effects in the pore pressure distribution, we computed and introduced a 2-dimensional finite difference algorithm that calculates the diffusion of fluid pressure during interseismic periods. We present the choice of the boundary conditions (tectonics) and the evolved stress maps and tectonic regimes around the model fault system due to the pore pressure and stress state and to seismic and aseismic slip on the two specified faults. Small-scale seismicity-induced stress perturbations develop near the model faults. Maps of R show complex distribution of the relative magnitude of the principal stresses. The hypothesis of homogeneous stress used in focal mechanism inversions is therefore to be handled with care in tectonically active regions exhibiting a bend in the plate boundary. Maps of Coulomb failure stress, maximum shear stress, and optimal orientation for failures calculated with the evolved 3-dimensional local stress tensor show the advantage of the forward approach compared to the stress triggering approach.

5.2 Methodological aspects

The earthquake process involves processes spanning over 21 orders of magnitude in time and 15 orders of magnitude in space. It is studied by laboratory experiments (e.g., short nucleation process experiments or long deformation experiments, from microseconds to days and from micrometers to meters), field measurements and geophysics (e.g., structural geology, fault mapping, plate boundary, mantle convection, earthquakes, from milliseconds to million years and from micrometers to thousand kilometers), and space-borne observations (e.g., coseismic surface deformation, subsidence, erosion, long-term surface strain rates, from seconds to years and from millimeters to thousands of kilometers). Forward modeling earthquake generation on interacting faults including large-scale tectonics and a detailed handling of fault zone hydraulics is therefore a difficult task.

5.2.1 The quasi-static approach

We considered the problem of earthquake mechanics from a tectonic scale while keeping small-scale processes intact. We made significant approximations to simplify the physics, while ensuring that these approximations had substantial supporting evidence. The advantage of the quasi-static approach shown here is utilizing analytic solutions for the internal displacement field due to slip on a model subfault. This guarantees accuracy of the solutions along with other significant advantages. There is no need for a 3-dimensional mesh covering the model space; the exact displacement (and subsequent stress) field on a subfault is calculated directly from the dislocation that causes the perturbation and does

not require the convergence of a numerical method (e.g., finite elements) on a series of nodes linking the perturbation to the observation point. This saves considerable computation time and also gives more freedom in the choice of the model geometry and the range of spatial scales considered. Thus, the tectonic loading is applied on dislocation planes much larger than the model faults (e.g. 800 km long, to avoid lateral boundary effects) whereas the stresses are monitored on 2 km long subfaults and creep slip is calculated using the tens of centimeter wide fault zone width. Note that in principle, the subfault size can be reduced (or alternatively, the resolution can be increased), but this results in the usual compromise between resolution and computation time.

5.2.2 A modular, flexible tool

The computer code is made of a series of modules articulated within a main fault interaction loop and synchronized namely through the time step calculation. After the definition of the initial conditions, a module calculates the time step required to reach failure on exactly one subfault. Once slip on a subfault is initiated, the subsequent rupture is controlled by the physics of a propagating elastic dislocation. Other modules include in-plane fluid diffusion, slip calculation to get the assumed stress drop, pore pressure redistribution, strain redistribution and stress calculation. Other processes that have to be incorporated depend mainly on the drained vs undrained assumptions. For instance, pore pressure redistribution occurs only once the system is in stress equilibrium, and porosity is updated for frictional dilatancy before pore pressure redistribution. This occurs because although fluids do not fill the new porosity instantaneously, we consider that pore pressure aids the propagation of the cracks responsible for the increase in porosity. This structure is very convenient both to test different approaches (e.g., different pore pressure redistribution methods, different boundary conditions in terms of pore pressure, see differences between Chapter 2 and Chapter 3) and to easily add modules.

5.3 Perspectives

The results of this thesis form a basis for many future directions in modeling the earthquake process, with the long-term goal of building physics-based, real-time self-learning models that describe the physics of major active faults. Such models can be tailored to particular tectonic regimes and fault systems that pose a major seismic risk (e.g., the North Anatolian Fault near Istanbul, the San Andreas fault at Parkfield, the Nojima Fault near Kobe), and of intraplate deformation in particularly sensitive densely populated areas. A number of future developments and studies are necessary before achieving this goal, and some of these are discussed below.

5.3.1 Test of model hypotheses

The first test concerns the validity of the quasi-static approach. The quasi-static approach assumes that during a rupture, all stress transfer due to increments of slip is instantaneous whereas the dynamic approach explicitly includes compressional and shear wave propagation from the part of the fault that slips to the surrounding area. In particular,

if slip continues behind the rupture front, the waves that arrive at a point ahead of it will come from both the rupture front and behind it. A numerical test can be conducted that compares two sets of results (rupture propagation, stress drop distribution and the interaction between nearby faults) for identical initial conditions generated by our quasi-static model (at the onset of a large rupture), one obtained through a dynamic (wave propagation) code (Harris and Day, 1999), and the other one by our quasi-static codes.

The second test will place independent constraints on the rates of porosity creation and permeability reduction (e.g., crack sealing) under anticipated in-situ conditions to test which co-seismic processes (e.g., process zone creation, frictional dilatancy, slip propagation) behave essentially undrained (i.e., faster than fluid flow). Data to be used in this portion of my study would be derived from laboratory and field studies conducted by others, including: 1) measurements of porosity creation and/or destruction during slip on simulated faults in the lab (Marone et al., 1990) and comparison of the acoustic emissions with pore pressure evolution during the fracturing of rock samples (Sammonds et al., 1992), 2) modeling results of reactive transport in fractured media (Heinrich et al., 1996), and 3) field studies of the relative rates and mechanisms of hydrothermal alteration and crack sealing along exhumed faults (e.g., Boullier et al., 2001). Further investigations would require more in situ data (namely from boreholes).

5.3.2 Theoretical follow-ups

Model results have pointed to several directions of research for future work. These include calculation of the total stress in a 3-dimensional ductile fault zone subjected to shearing and compaction. Continuum models will likely be used to study the response of a ductile fault zone because analytical solutions for these processes are scarce. The term creep compaction, used extensively in the literature, is actually a misnomer. Calculation of the total stress in a ductile fault zone will introduce a dependency between the shear creep rate and the compaction rate. Such a model will be self-consistent and will not be limited by the approximation shown in Sleep and Blanpied (1992) and Chapter 3. Controls on the temporal and spatial distribution of creep vs unstable (seismic) slip along faults and the loading process for repeating earthquakes (Ellsworth, Elsevier Science Ltd., 1995) could be mechanically assessed with such a model advancement.

An important aspect emphasized in this work is a study of the role of the damage zone in the pore pressure cycle in fault zones. We considered a relatively low permeability fault core consisting of a coseismic fault surface embedded in a zone composed of breccia and/or cataclaste, or gouge. This is surrounded by a high permeability damaged zone surrounding the core. The processes and hydraulic coupling between the fault core and the damage zone were not adequately treated here, but could play a major role in modulating fault zone pore pressures. Rawling et al. (2001) review permeability data for contrasting types of fault-zones and show, in the case of a granitic protolith, permeability ratios of 10^3 and 10^{-3} , for the damage zone and the fault core, respectively, with respect to the intact rock. Veins between the fault core and the damage zone were observed (e.g., Tanaka et al, 2001), indicating rapid fluid flow in the direction normal to the fault strike.

Conceptually, flux normal to the fault could be much faster than in-plane flow because of the much higher cross-sectional area. A criterium for crack opening and insight in the rate of sealing would help constrain the permeability changes of fault zones during earthquake cycles, both in-plane and perpendicular to the fault. Note that a realistic pore pressure redistribution together with knowledge of the normal stress and static friction leads to a better estimation of the Coulomb failure stress, i.e., the quantity of shear stress that a fault can sustain before producing an earthquake. However, all fault zones do not exhibit a damage zone, so additional alternative fault structures should also be investigated.

Earthquake-induced stress perturbations (Chapter 2 and 4) as well as the evolution toward an overpressured fault of the misoriented thrust fault (Chapter 2) pointed to the need for the monitoring of the evolved stress tensor and subsequent tectonic regimes in the model space. This provides the basis for investigating the time-evolution of fault systems. In such an investigation, new faults will be generated in response to the evolving stress state, while fault segments no longer stressed to failure will be abandoned. Another related investigation should focus on identifying characteristic events and the long-term effect of stress triggering in the generated seismicity on the model fault system.

Another aspect relates to earthquake-related surface deformation. Except within the fault zone, we consider only elastic deformation and we show coseismic elastic surface deformation fields. To provide geomorphologists with a long-term topography of tectonically active areas, a criterium for keeping permanent deformation should be determined. The resulting topography can then be eroded by coupling to erosion modules.

5.3.3 Investigation of, and coupling to, alternative models

Models we have developed thus far are quite effective in examining the role of fluids in the earthquake process, fluid pressure changes (e.g., poroelasticity, viscous compaction, etc.) and their possible effects in controlling earthquake interaction and recurrence. However, it is not known if such fluid pressure changes actually occur along natural fault zones or whether alternative models may be just as plausible. Alternative earthquake failure models derived from laboratory rock mechanics studies to see if alternative physics may be just as effective in explaining the physics of earthquakes, including clustering, interaction and recurrence along the central San Andreas fault.

These alternative models include 1) rate- and state-dependant friction (e.g., Dieterich, 1978 & 1992), low-temperature brittle creep rate-limited by sub-critical crack growth (e.g., Lockner, 1998), 2) models incorporating complete or partial creep of parts of the fault, such as models in which a locked patch is embedded in and loaded by an aseismically creeping fault plane (Vidale et al., 1994; Ellsworth, Elsevier Science Ltd., 1995; Nadeau and Johnson, 1998, e.g.), and models in which the locked patch itself exhibits either small (Sleep and Blanpied, 1992) or large (Beeler et al., in press 2001a) amounts of creep during the interseismic period. To model partial fault creep, a number of questions will need to be addressed, namely how the intrinsic viscosity evolves with time or with slip in a fault core (e.g., with relation to grain size variations, pressure solution, pseudotachylites, etc.),

and how to account for the observed larger creep slip rates at the subsurface than at depth. This observation is in contradiction with the shear creep formulation as used by Sleep and Blanpied, 1992. New laboratory work on creep rheologies of gouge like materials (e.g., at Stanford university) will provide a good basis for new theoretical modeling of fault zone rheology and a possible process-oriented alternative to the rate and state approach.

Finally, time-dependant processes are needed to model the recovery of fault strength during the interseismic period, in addition to changes in fault zone fluid pressure. This includes increases in the intrinsic frictional strength, either as observed in dry room-temperature experiments (e.g., Marone, 1998; Beeler and f. Wong, in press 2001b) or solution-transport healing of contacting asperities (e.g., Angevine et al., 1982, Hickman and Evans, 1992). For studies over large time periods, postseismic relaxation should be included after earthquake generation on the model faults (Pollitz et al., 2001).

5.3.4 Test against data, example of Central California

Once the models are developed, they will need to be tested against data. Any tectonic environment could be chosen to perform such tests, subduction zones as well as extensional environments. We will describe here the example of the recurring (characteristic) earthquakes in Central California, especially around Parkfield.

The goal is to see which - if any - of these models (or combination of models) is capable of explaining the observed recurrence times and source characteristics of individual repeating microearthquakes at Parkfield, and the temporal and spatial interactions between nearby microearthquakes. As an illustration of the latter point, following on ideas originally proposed by Nur in the 1970's, Johnson and McEvilly (1995) claimed that the spatial migration of microearthquakes at Parkfield supported a fluid diffusion model for earthquake triggering. However, other models (such as the rate-and-state model) might explain these apparent microearthquake interactions equally well. The study of remarkable features (e.g., streaks, or repeating characteristic earthquakes, or migrating microearthquakes) will lead to the set up of initial conditions (e.g., locked patch in a creeping segment) as observed and to the test of different models or combination of models to produce output comparable at least in some way to what is observed. The result will be a set of models and initial conditions that are satisfactory (or have satisfactory features). It would be extremely useful, both as a stand-alone scientific study and as a precursor to eventual drilling into the San Andreas fault zone through SAFOD (San Andreas Scientific Drilling Project), to see if and in what manner the recurrence behavior of individual characteristic earthquakes and the spatial and temporal interactions of microearthquakes at Parkfield might discriminate between competing earthquake physics models.

5.4 Concluding remark

This thesis showed some of the significant progress made by the community in the field of earthquake mechanics and forward modeling of the earthquake process. However, it

also pointed out to a number of difficulties. Earthquakes happen at depth and a direct observation is therefore not possible. If the time scale for stress build-up on fault systems and recurrence time of major seismic events are large compared to human life (hundreds to several thousands of years), the time-scales for earthquake nucleation and propagation are extremely small (< 1 s to max. 1 min), making it difficult for researchers to capture the governing physical and chemical processes at work. Despite the development or improvement of techniques to measure or evaluate it (e.g., borehole break-outs, focal mechanism inversion), the stress state is still not well known in the crust, i.e., the magnitude, orientation, and origin of the forces acting on the faults are not known precisely. Even though seismically active areas (in particular if they are populated areas) become the subject of extensive studies, some large earthquakes occurred in urban areas on faults that were not mapped (e.g., the Kobe earthquake, Japan, 1995).

In this context, our modeling required a number of assumptions concerning the dominant processes, and numerous approximations concerning the (many) unconstrained parameters. A genuine reader might curiously wonder how we make these choices. Well, as one renowned physicist once noted

“In general we look for a new law by the following process:
First we guess it.”

Richard P. Feynman, *The Character of Physical Law*

And so forms the basis of attempting to model the natural world. Building and studying these models then provides the basis for better guesses in the future. We described how a forward fault model such as developed in this PhD work can be used (alone or combined with other modules such as postseismic deformation) to constrain tectonic loading on a portion of crust and can help test the prevailing hypotheses in the earthquake physics and chemistry communities by comparing model results and data in the framework of a regional model. Feynman goes on ...

“Then we compute the consequences of that guess to see what would be implied if this law that we guessed is right. Then we compare the results of the computation to nature, with experiment or experience, compare it directly with observation, to see if it works. If it disagrees with experiment it is wrong. In that simple statement is the key to science.”

Richard P. Feynman, *The Character of Physical Law*

Since the models (or combination of models) can provide the long-term behavior of the model space in terms of seismicity, overpressures, fault interaction, stable sliding, and evolution of stress, tectonic regime and optimal orientation for failure, the optimistic reader, concerned with seismic hazard assessment, might still ask “When will you (researchers) be able to predict where, when and how earthquakes will strike?”. Or “will you ever be able to predict where, when and how earthquakes will strike?”

Another well-known physicist put it succinctly:

“Prediction is difficult. Especially about the future.”

Niels Bohr

But then, where would be the challenge if it were not the case?

Bibliography

- Angevine, C. L., Turcotte, D. L., Furnish, M. D., 1982. Pressure solution lithification as a mechanism for the stick-slip behavior of faults. *Tectonics* 1, 151–160.
- Argus, D. F., Gordon, R. G., 1991. Current Sierra Nevada-North America motion from very long baseline interferometry: Implications for the kinematics of the western United States. *Geology* 19, 1085–1088.
- Bak, P., Tang, C., 1989. Earthquakes as a self-organized critical phenomenon. *J. Geophys. Res.* 94 (B11), 15,635–15,637.
- Barnes, H. A., Hutton, J. F., Walters, K., 1993. An introduction to rheology. Vol. 3 of Rheology series. Elsevier.
- Barton, N., 1976. The shear strength of rock and rock joints. *Int. J. Rock Mech. Min. Sci. & Geomech. Abstr.* 13, 255–279.
- Beeler, N., f. Wong, T., in press 2001b. Stress drop and laboratory-inferred interseismic strength recovery. *J. Geophys. Res.* .
- Beeler, N., Lockner, D. A., Hickman, S. H., in press 2001a. A simple creep-slip and stick-slip model for repeating earthquakes and its application to micro-earthquakes at Parkfield. *Bull. Seismol. Soc. Am.* .
- Beeler, N., Simpson, R., Hickman, S., Lockner, D., 2000. Pore fluid pressure, apparent friction, and Coulomb failure. *J. Geophys. Res.* 105 (B11), 25,533–25,542.
- Ben-Zion, Y., Rice, J. R., 1993. Earthquake failure sequences along a cellular fault zone in a three-dimensional elastic solid containing asperity and nonasperity regions. *J. Geophys. Res.* 98 (B8), 14,109–14,131.
- Ben-Zion, Y., Rice, J. R., 1995. Slip patterns and earthquake populations along different classes of faults in elastic solids. *J. Geophys. Res.* 100 (B7), 12,959–12,983.
- Blanpied, M. L., Lockner, D. A., Byerlee, J., 1992. An earthquake mechanism based on rapid sealing of faults. *nature* 358, 574–576.
- Blanpied, M. L., Tullis, T. E., Weeks, J. D., 1998. Effects of slip, slip rate, and shear heating on the friction of granite. *J. Geophys. Res.* 103 (B1), 489–511.
- Bos, B., Peach, C. J., Spiers, C. J., 2000. Frictional-viscous flow of simulated fault gouge caused by the combined effects of phyllosilicates and pressure solution. *Tectonophysics* 327 (3-4), 173–194.
- Bouchon, M., Campillo, M., Cotton, F., 1998a. Stress field associated with the rupture of the 1992 Landers, California, earthquake and its implications concerning the fault strength at the onset of the earthquake. *J. Geophys. Res.* 103 (B9), 21,091–21,097.
- Bouchon, M., Sekiguchi, H., Irikura, K., Iwata, T., 1998b. Some characteristics of the stress field of the 1995 Hyogo-Ken Nanbu (Kobe) earthquake. *J. Geophys. Res.* 103 (B10), 24,271–24,282.

- Boullier, A.-M., Ohtani, T., Fujimoto, K., Ito, H., Dubois, M., 2001. Fluid inclusions in pseudotachylites from the Nojima fault, Japan. *J. Geophys. Res.* 106 (B10), 21,965–21,977.
- Brace, W., 1977. Permeability from resistivity and pore shape. *J. Geophys. Res.* 82, 3343–3349.
- Brereton, R., Muller, B., 1991. European stress - contributions from borehole breakouts. *Phil. Trans. Roy. Soc. London A* 337 (1645), 165–179.
- Burnham, C., Holloway, J., Davis, N., 1969. *Thermodynamic Properties of Water to 1,000°C and 10,000 Bars*. Geological Society of America, 96 p., Boulder, Colorado.
- Byerlee, J., 1978. Friction of rocks. *Pure Appl. Geoph.* 116 (4-5), 615–626.
- Byerlee, J., 1993. Model for episodic flow of high-pressure water in fault zones before earthquakes. *Geology* 21, 303–306.
- Chester, F. M., Evans, J. P., Biegel, R. L., 1993. Internal structure and weakening mechanisms of the San Andreas fault. *J. Geophys. Res.* 98 (B1), 771–786.
- Cohee, B., Beroza, G., 1994. Slip distribution of the 1992 Landers earthquake and its implications for earthquake source mechanism. *Bull. Seismol. Soc. Am.* 84, 692–712.
- Cox, S. F., 1995. Faulting processes at high fluid pressures: an example of fault valve behavior from the Wattle Gully fault, Victoria, Australia. *J. Geophys. Res.* 100 (B7), 12841–12859.
- Dascalu, C., Ionescu, I., Campillo, M., 2000. Fault finiteness and initiation of dynamic shear instability. *Earth Planet. Sci. Lett.* 177 (3-4), 163–176.
- Delouis, B., Lungren, P., Salichon, J., Giardini, D., 2000. Joint inversion of InSAR and teleseismic data for the slip history of the 1999 Izmit (Turkey) earthquake. *Geophys. Res. Lett.* 27 (20), 3389–3392.
- Dieterich, J. H., 1979. Modeling of rock friction -1. Experimental results and constitutive equations. *J. Geophys. Res.* 84 (B5), 2161–2168.
- Ekström, G., Stein, R. S., Eaton, J. P., Eberhart-Phillips, D., 1992. Seismicity and geometry of a 110-km-long blind thrust fault 1. The 1985 Kettleman Hills, California, earthquake. *J. Geophys. Res.* 97 (B4), 4843–4864.
- Ellsworth, W. L., Elsevier Science Ltd., 1995. Characteristic earthquakes and long-term earthquake forecasts: implications of central California seismicity. in *Urban Disaster Mitigation: the Role of Engineering and Technology*, edited by F.Y. Cheng and M.S. Sheu, pp. 1–14.
- Evans, J. P., Forster, C. B., Goddard, J. V., 1997. Permeability of fault-related rocks, and implications for hydraulic structure of fault zones. *J. Struct. Geol.* 19 (11), 1393–1404.

- Faulkner, D. R., Rutter, E. H., 2001. Can the maintenance of overpressured fluids in large strike-slip fault zones explain their apparent weakness? *Geology* 29 (6), 503–506.
- Fenoglio, M. A., Johnston, M. J. S., Byerlee, J. D., 1995. Magnetic and electric fields associated with changes in high pore pressure in fault zones: application to the Loma Prieta ULF emissions. *J. Geophys. Res.* 100 (B7), 12,951–12,958.
- Fitzenz, D. D., Miller, S. A., 2001. A forward model for earthquake generation on interacting faults including tectonics, fluids, and stress transfer. *J. Geophys. Res.* 106 (B11), 26,689–26,706.
- Gomberg, J., Beeler, N., Blanpied, M. L., 2000. On rate-state and Coulomb failure models. *J. Geophys. Res.* 105 (B4), 7857–7871.
- Gratier, J.-P., Favreau, P., Renard, F., in press. Modeling fluid transfer along Californian faults when integrating pressure solution crack-sealing and compaction processes. *J. Geophys. Res.* .
- Guatteri, M., Spudich, P., 1998. Coseismic temporal changes of slip direction: The effect of absolute stress on dynamic rupture. *Bull. Seismol. Soc. Am.* 88 (3), 777–789.
- Gueguen, Y., Dienes, J., 1989. Transport properties of rocks from statistics and percolation. *Math. Geol.* 21, 1–13.
- Hardebeck, J. L., Hauksson, E., 1999. Role of fluids in faulting inferred from stress field signatures. *Science* 285 (5425), 236–239.
- Hardebeck, J. L., Hauksson, E., 2001. Crustal stress field in southern California and its implications for fault mechanics. *J. Geophys. Res.* 106 (B10), 21859–21882.
- Harris, R. A., Day, S. M., 1999. Dynamic 3d simulations of earthquakes on en echelon faults. *Geophys. Res. Lett.* 26 (14), 2089–2092.
- Heinrich, C., Walshe, J. L., Harrold, B. P., 1996. Chemical mass transfer modelling of ore-forming hydrothermal systems; current practise and problems. in *The conjunction of processes resulting in the formation of orebodies* , *Ore Geology Reviews*, vol.10, no. 3–6, pp.319–338.
- Henderson, J. R., Maillot, B., 1997. The influence of fluid flow in fault zones on patterns of seismicity: A numerical investigation. *J. Geophys. Res.* B2, 2915–2924.
- Hickman, S., Evans, B., Academic, San Diego, Calif., 1992. Growth of grain contacts in halite by solution transfer: Implications for diagenesis, lithification, and strength recovery. in *Fault Mechanics and Transport Properties of Rocks*, *Int. Geophys. Ser.* , vol.51, edited by B. Evans and T.-f. Wong, pp. 253–280.
- Honkura, Y., Işikara, A. M., Oshiman, N., Ito, A., üçer, B., Ş. Barış, Tuncer, M. K., Matsushima, M., Pektaş, R., Çelik, C., Tank, S. B., Takahashi, F., Nakanishi, M., Yoshimura, R., Ikeda, Y., Komut, T., 2000. Preliminary results of multidisciplinary

observations before, during and after the Kocaeli (Izmit) earthquake in the western part of the north Anatolian fault zone. *Earth Planets and Space* 54 (4), 293–298.

Hubbert, M. K., Rubey, W. W., 1959. Role of fluid pressure in mechanics of overthrust faulting. *Bull. Geol. Soc. Am.* 70, 115–166.

Ikeda, R., Iio, Y., Omura, K., 2001. In situ stress measurements in NIED boreholes in and around the fault zone near the 1995 Hyogo-ken Nanbu earthquake, Japan. *Island Arc* 10 (3-5), 252–260.

Johnson, P., McEvilly, T., 1995. Parkfield seismicity: Fluid driven? *J. Geophys. Res.* 100 (B12), 12,937–12,950.

Kame, N., Yamashita, T., 1999. A new light on arresting mechanism of dynamic earthquake faulting. *Geophys. Res. Lett.* 26 (13), 1997–2000.

King, G. C. P., Stein, R. S., Lin, J., 1994. Static stress changes and the triggering of earthquakes. *Bull. Seismol. Soc. Am.* 84 (3), 935–953.

Labatut, P., Moretti, I., 2001. Diagenesis-dependence of cataclastic thrust fault zone sealing in sandstones. example from the Bolivian sub-andean zone. *J. Struct. Geol.* 23, 1659–1675.

Lachenbruch, A. H., Sass, J. H., 1980. Heat flow and energetics of the San Andreas fault zone. *J. Geophys. Res.* 85 (B11), 6185–6222.

Lockner, D. A., 1998. A generalized law for brittle deformation of westerly granite. *J. Geophys. Res.* 103, 5107–5123.

Lockner, D. A., Byerlee, J. D., 1993. How geometrical constraints contribute to the weakness of mature faults. *Nature* 363, 250–252.

Lockner, D. A., Evans, B., 1995. Densification of quartz powder and reduction of conductivity at 700°. *J. Geophys. Res.* 100 (B2), 13,081–13,092.

Marone, C., 1998. The effect of loading rate on static friction and the rate of fault healing during the earthquake cycle. *Nature* 391 (1 JAN), 69–72.

Marone, C., Raleigh, C. B., Scholz, C. H., 1990. Frictional behavior and constitutive modeling of simulated fault gouge. *J. Geophys. Res.* 95 (B5), 7007–7025.

Marone, C., Scholz, C. H., 1988. The depth of seismic faulting and the upper transition from stable to unstable slip regimes. *Geophys. Res. Lett.* 15 (6), 621–624.

Mase, C. W., Smith, L., 1985. Pore-fluid pressures and frictional heating on a fault surface. *Pure Appl. Geoph.* 122, 583–607.

Massonnet, D., Rossi, M., Carmona, C., Adragna, F., Peltzer, G., Feigl, K., Rabaute, T., 1993. The displacement field of the Landers earthquake mapped by radar interferometry. *Nature* 364, 138–142.

- Meghraoui, M., Camelbeeck, T., Vanneste, K., Brondeel, M., Jongmans, D., 2000. Active faulting and paleoseismology along the Bree fault, lower Rhine graben, Belgium. *J. Geophys. Res.* 105 (B6), 13,809–13,841.
- Miller, S. A., Ben-Zion, Y., Burg, J.-P., 1999. A three dimensional fluid-controlled earthquake model: Behavior and implications. *J. Geophys. Res.* 104 (B5), 10,621–10,638.
- Miller, S. A., Nur, A., 2000. Permeability as a toggle switch in fluid-controlled crustal processes. *Earth Planet. Sci. Lett.* 183 (1-2), 133–146.
- Miller, S. A., Nur, A., Olgaard, D. L., 1996. Earthquakes as a coupled shear stress-high pore pressure dynamical system. *Geophys. Res. Lett.* 23, 197–200.
- Moore, D. E., Lockner, D. A., Ito, H., Ikeda, R., 1999. Correlation of deformation textures with laboratory measurements of permeability and strength of Nojima fault zone core samples. in *Proceedings of the International workshop on the Nojima fault core and borehole data analysis*, USGS Open-file report 00-129, pp.159–166.
- Morrow, C., Lockner, D. A., Hickman, S., Rusanov, M., Rockel, T., 1994. Effects of lithology and depth on the permeability of core samples from the Kola and KTB drillholes. *J. Geophys. Res.* 99, 7274–7623.
- Morrow, C., Shi, L., Byerlee, J., 1984. Permeability of fault gouge under confining pressure and shear stress. *J. Geophys. Res.* 89, 3193–3200.
- Nadeau, R. M., Johnson, L. R., 1998. Seismological studies at Parkfield V: Moment release rates and estimates of source parameters for small repeating earthquakes. *Bull. Seismol. Soc. Am.* 88 (3), 790–814.
- Nalbant, S. S., Hubert, A., King, G. C. P., 1998. Stress coupling between earthquakes in northwest Turkey and the north Aegean Sea. *J. Geophys. Res.* 103 (B10), 24,469–24,486.
- Nur, A., Booker, J., 1972. Aftershocks caused by pore fluid flow? *Science* 175, 885–887.
- Nur, A., Byerlee, J. D., 1971. An exact effective stress law for elastic deformation of rock with fluids. *J. Geophys. Res.* 76 (26), 6414–6419.
- Okada, Y., 1985. Surface deformation due to shear and tensile faults in a half-space. *Bull. Seismol. Soc. Am.* 75 (4), 1135–1154.
- Okada, Y., 1992. Internal deformation due to shear and tensile faults in a half space. *Bull. Seismol. Soc. Am.* 82 (2), 1018–1040.
- Okumura, K., Yoshioka, T., Kuscu, I., 1993. Faulting on the North Anatolian fault in these two millennia. in *USGS Open-file report 94-568*, pp.143–144.
- Pacheco, J. F., Scholz, C. H., Sykes, L. R., 1992. Changes in frequency-size relationship from small to large earthquakes. *Nature* 355, 71–73.

- Pantosti, D., Schwartz, D. P., Valensise, G., 1993. Paleoseismology along the 1980 surface rupture of the Irpinia fault: Implications for earthquake recurrence in the southern Apennines, Italy. *J. Geophys. Res.* 98 (B4), 6561–6577.
- Perfettini, H., Stein, R. S., Simpson, R. W., Cocco, M., 1999. Stress transfer by the 1988-1989 $M=5.3$ and 5.4 Lake Elsmar foreshocks to the Loma Prieta fault: Unclamping at the site of peak mainshock slip. *J. Geophys. Res.* 104, 20,169–20,182.
- Pollitz, F. F., Wicks, C., Thatcher, W., 2001. Mantle flow beneath a continental strike-slip fault: postseismic deformation after the 1999 Hector Mine earthquake. *Science* 293, 1814–1818.
- Prescott, W. H., Savage, J., Svarc, J. L., Manaker, D., 2001. Deformation across the Pacific-North America plate boundary near San Francisco, California. *J. Geophys. Res.* 106 (B4), 6673–6682.
- Provost, A., Houston, H., 2001. Orientation of the stress field surrounding the creeping section of the San Andreas fault: Evidence for a narrow mechanically weak fault zone. *J. Geophys. Res.* 106 (B6), 11,373–11,386.
- Quattrocchi, F., 1999. In search of evidence of deep fluid discharges and pore pressure evolution in the crust to explain the seismicity style of the Umbria-Marche 1997-1998 seismic sequence (central Italy). *Ann. Geofis.* 42 (4), 609–636.
- Rawling, G. C., Goodwin, L. B., Wilson, J. L., 2001. Internal architecture, permeability structure, and hydrologic significance of contrasting fault-zone types. *Geology* 29, 43–46.
- Renard, F., Gratier, J.-P., Jamtveit, B., 2000. Kinetics of crack-sealing, intergranular pressure solution, and compaction around active faults. *J. Struct. Geol.* 22, 1395–1407.
- Rice, J. R., 1993. Spatio-temporal complexity of slip on a fault. *J. Geophys. Res.* 98 (B6), 9885–9907.
- Rice, J. R., Academic, San Diego, Calif., 1992. Fault stress states, pore pressure distributions, and the weakness of the San Andreas fault. in *Fault Mechanics and Transport Properties of Rocks*, Int. Geophys. Ser. , vol.51, edited by B. Evans and T.-f. Wong, pp. 9885–9907.
- Rice, J. R., Cleary, M. P., 1976. Some basic stress diffusion solutions for fluid-saturated elastic porous media with compressible constituents. *Rev. Geophys. Space Phys* 14 (2), 227–241.
- Robert, F., Boullier, A.-M., 1993. Mesothermal gold-quartz veins and earthquakes. in *The Mechanical Involvement of Fluids in Faulting* edited by S. Hickman, R. Sibson and R. Bruhn, pp. 18–30, U.S. Geol. Surv., Reston, Va.
- Robinson, R., Benites, R., 1995. Synthetic seismicity models of multiple interacting faults. *J. Geophys. Res.* 100 (B9), 18,229–18,328.

- Robinson, R., Benites, R., 1996. Synthetic seismicity models for the wellington region, new zealand: implications for the temporal distribution of large events. *J. Geophys. Res.* 101 (B12), 27,833–27,844.
- Rudnicki, J. W., John Wiley, New York, 1985. Effect of pore fluid diffusion on deformation and failure of rock. in *Mechanics of Geomaterials*, edited by Z. Bazant, pp. 315–346.
- Rundle, J. B., 1988. A physical model for earthquakes, 1, Fluctuations and interactions. *J. Geophys. Res.* 93 (B6), 6237–6254.
- Rundle, J. B., 1989. Derivation of the complete Gutenberg-Richter magnitude-frequency relation using the principle of scale invariance. *J. Geophys. Res.* 94 (B9), 12,337–12,342.
- Sammonds, P. R., Meredith, P. G., Main, I. G., 1992. Role of pore fluids in the generation of seismic precursors to shear fracture. *Nature* 289, 228–230.
- Scholz, C. H., 1990. *The Mechanics of Earthquakes and Faulting*. Cambridge Univ. Press, New York.
- Scholz, C. H., 1992. Weakness amidst strength. *Nature* 359, 677–678.
- Scholz, C. H., 1998. Earthquakes and friction laws. *Nature* 391 (1 JAN), 37–42.
- Scholz, C. H., 2000. Evidence for a strong San Andreas fault. *Geology* 28 (2), 163–166.
- Segall, P., Rice, J. R., 1995. Dilatancy, compaction, and slip instability of a fluid-infiltrated fault. *J. Geophys. Res.* 100 (B11), 22,155–22,171.
- Sibson, R. H., 1973. Interaction between temperature and pore fluid pressure during an earthquake faulting and a mechanism for partial or total stress relief. *Nature* 243, 66–68.
- Sibson, R. H., 1992. Fault-valve behavior and the hydrostatic-lithostatic fluid pressure interface. *Earth-Science Reviews* 32, 141–144.
- Sibson, R. H., 1993. Geological evidence of fluid involvement in the rupture processes of crustal earthquakes, in: *The Mechanical Involvement of Fluids in Faulting* edited by S. Hickman, R. Sibson and R. Bruhn, pp. 31–38, U.S. Geol. Surv., Reston, Va.
- Sleep, N., 1995. Ductile creep, compaction and rate and state dependent friction within major fault zones. *J. Geophys. Res.* 100 (B7), 13,065–13,080.
- Sleep, N., Blanpied, M. L., 1992. Creep, compaction and the weak rheology of major faults. *Nature* 359, 687–692.
- Sleep, N., Blanpied, M. L., 1994. Ductile creep and compaction: A mechanism for transiently increasing fluid pressure in mostly sealed faults zones. *Pure Appl. Geoph.* 143, 9–40.
- Spray, J. G., 1995. Pseudotachylite controversy: Fact or friction? *Geology* 23 (12), 1119–1122.

- Spudich, P. K. P., 1992. On the inference of absolute stress levels from seismic radiation. *Tectonophysics* 211, 99–106.
- Stein, R. S., Barka, A. A., Dieterich, J. H., 1997. Progressive failure on the North Anatolian fault since 1939 by earthquake stress triggering. *Geophys. J. Int.* 128 (3), 594–604.
- Steketee, J. A., 1958. On Volterra's dislocations in a semi-infinite elastic medium. *Can. J. Phys.* 36, 192–205.
- Stewart, I. S., Sauber, J., Rose, J., 2000. Glacio-seismotectonics: ice sheets, crustal deformation and seismicity. *Quaternary Science Reviews* 19 (14-15), 1367–1389.
- Streit, J. E., Cox, S. F., 2000. Asperity interactions during creep of simulated faults at hydrothermal conditions. *Geology* 28 (3), 231–234.
- Talwani, P., Cobb, J. S., Schaeffer, M. F., 1999. In situ measurements of hydraulic properties of a shear zone in northwestern South Carolina. *J. Geophys. Res.* 104 (B7), 14,993–15,003.
- Tanaka, H., Fujimoto, K., Ohtani, T., Ito, H., 2001. Structural and chemical characterization of shear zones in the freshly activated Nojima fault, Awaji island, southwest Japan. *J. Geophys. Res.* 106 (B5), 8789–8810.
- Terzaghi, K., 1923. Die berechnung der durchlässigkeitsziffer des tones aus dem verlauf der hydrodynamischen spannungerscheinungen. *Sber. Adad. Wiss.* 132, 105–.
- Townend, J., Zoback, M. D., 2000. How faulting keeps the crust strong. *Geology* 28 (5), 399–402.
- Townend, J., Zoback, M. D., Special Publication of the Geological Society of London, 186, 2001. Implications of earthquake focal mechanisms for the frictional strength of the San Andreas fault system. in *The Nature and Tectonic Significance of Fault Zone Weakening*, edited by R.E. Holdsworth, R. A. Strachan, J. MacLoughlin, and R. J. Knipe, pp. 13–21.
- Tsukahara, H., Ikeda, R., Omura, K., 1996. In-situ stress measurement in an earthquake focal area. *Tectonophysics* 262 (1-4), 281–290.
- Vidale, J. E., Ellsworth, W. L., Cole, A., Marone, C., 1994. Rupture variation with recurrence interval in 18 cycles of a small earthquake. *Nature* 368, 624–626.
- Voisin, C., Campillo, M., Ionescu, I., Cotton, F., Scotti, O., 2000. Dynamic versus static stress triggering and friction parameters: Inferences from the November 23, 1980, Irpinia earthquake. *J. Geophys. Res.* 105 (B9), 21,647–21,659.
- Walsh, J., 1981. Effects of pore pressure and confining pressure on fracture permeability. *International journal of rock mechanics mineral science and geomechanical abstract* 18, 429–435.

- Ward, S. N., 1997. Dogtails versus rainbows: synthetic earthquake rupture models as an aid in interpreting geological data. *Bull. Seismol. Soc. Am.* 87 (6), 1422–1441.
- Wesson, R. L., 1988. Dynamics of fault creep. *J. Geophys. Res.* 93 (B8), 8929–8951.
- Yamashita, T., 1998. Simulation of seismicity due to fluid migration in a fault zone. *Geophys. J. Int.* 132, 674–686.
- Yamashita, T., 1999. Pore creation due to fault slip in a fluid-permeated fault zone and its effect on seismicity: Generation mechanism of earthquake swarms. *Pure Appl. Geoph.* 155, 625–647.
- Zanzerkia, E., Beroza, G., 2001. Evidence of pore-fluid effects in aftershock triggering from the 1992 landers and 1999 Hector mine earthquakes. *Eos Trans. AGU*, 82(47), Fall Meet. Suppl., Abstract S12F-05 .
- Zhang, S., Tullis, T., Scruggs, V., 2001. Implications of permeability and its anisotropy in a mica gouge for pore pressures in fault zones. *Tectonophysics* 335 (1-2), 37–50.
- Ziv, A., Rubin, A. M., 2000. Static stress transfer and earthquake triggering: No lower threshold in sight? *J. Geophys. Res.* 105 (B6), 13,631–13,642.
- Zoback, M. D., Healy, J. H., 1992. In situ stress measurements to 3.5 km depth in the Cajon Pass scientific research borehole: Implications for the mechanics of crustal faulting. *J. Geophys. Res.* 97, 5039–5057.
- Zoback, M. L., 1992. First- and second order patterns of stress in the lithosphere”: The World Stress Map Project. *J. Geophys. Res.* 97, 11,703–11,728.

Curriculum Vitae

DELPHINE D. FITZENZ**Geophysics engineer**

Department of Earth Sciences

Swiss Federal Institute of Technology, CH8093 Zürich, Switzerland,

Phone: +41-1-633 2751, Fax: +41-1-633 1108, Email: fitzenz@erdw.ethz.ch

Single, French national.

Date of birth: 06/06/1976.

RELEVANT WORK EXPERIENCE

- 1999-present** **PhD student**, *Engineering Geology, Geology Institute, ETH Zurich.*
Research work: Generalization of a 3-D fluid-driven fault interaction model. (Referents: Prof. S. Loew and Dr. S.A. Miller).
Assistant work: 1) assistance work for the course on 3D geometrical modeling for geologists (GOCAD); 2) co-system administrator of the UNIX system.
- July-Sept 1998** **Engineering training (M.S. Eng. work)**, *Laboratoire de Mesures en Forage (Aix-en-Provence, France)* - Improvement of the mineralogical inversion method obtained during the DEA training, obtention of profiles of mineralogy, overpressures and permeability for several holes.
- Feb-June 1998** **DEA (M.S.) work**, *it Laboratoire de Mesures en Forage (Aix-en-Provence, France)* - Mineralogical inversion of downhole measurements of physical properties and characterization of fluids circulation in the Barbados accretionary prism.
- July-Aug 1997** **Engineering training**, *BRGM Luminy - AFPS (Marseille, France)* - Contribution to the probabilistic evaluation of seismic hazard in France.
- Nov-April 1997** **Research project**, *IPG - Marine Geophysics Laboratory (Strasbourg, France)* - Paleomagnetic study of basalts dragged along the Central Indian Ridge and link with segmentation.
- July 96** **Summer training**, *Laboratoire de Mesures en Forage (Marseille, France)* - Creation of a database gathering physical and chemical ODP data on Hole 504B.

EDUCATION

- 1999-present** PhD student in the Engineering Geology Team (ETH- Swiss Federal Institute of Technology, Zürich).
- Nov. 1998** M.S. Engineer Geophysicist with honors (Mention Bien), EPGS (Ecole de Physique du Globe de Strasbourg, France).
- June 1998** D.E.A. (M.S. Degree) in Physics and Chemistry of the Earth with honors (Mention Bien), University of Strasbourg I, France. Option: Geophysics.
- 1995-1998** University Engineering School in Geophysics (EPGS)
- 1993-1995** Mathématiques Supérieures and Mathématiques Spéciales classes (College), Orléans, France.
- 1993** Scientific Baccalauréat C with honors (Mention Bien), L'Isle s/Sorgue, France.
-

MAIN FIELD EXPERIENCE

- Sept 1997** **Seismic profiling in the Ligurian Sea**, *Observatoire d'Océanologie, Villefranche sur mer, France*;
Geophysical study of a salt dome in South Alsace (seismic, gravimetry, magnetism, electrical sounding), *Geophysics Institute, Strasbourg, France*.

RESEARCH INTERESTS

- Fault mechanics and the role of fluids in faulting.
- Evolution of fault systems, i.e., how deformation localizes until a fault breaks, and then how the seismic activity on a fault can change the local stress tensor around it, such that the fault either interacts with other pre-existing faults or promotes the creation of new, better oriented faults.
- Multidisciplinary, integrative modeling approaches to study geological processes (from the grain-scale, with structural geology, to the tectonic plate scale, with seismology, geodesy and field geology).

LANGUAGES

French: mother tongue, **English:** fluent, **German:** read, written, spoken (not fluent).

COMPUTER EXPERTISE

- Computer environment: UNIX (use and system management of an SGI workstation network), MACINTOSH, WINDOWS
- Programming experience in: Fortran (77, 90,95), OpenMP, Matlab, LaTeX (and TurboC, TurboPascal)
- Softwares : Gocad, FeFlow, Grapher, Surfer, Kaleidagraph, MSoffice, Canvas, Netscape, etc.

TECHNICAL REPORTS

- Fitzenz, D.D., 1997, Contribution à l'évaluation probabiliste de l'aléa sismique à l'échelle du territoire national, Note technique BGRMSGNUPERNGNT97014, pp 26.
- Dominique, P., Fitzenz, D.D., Samarq, F., 1997, Evaluation probabiliste de l'aléa sismique à l'échelle du territoire national, BRGM R39774, pp 54.

ABSTRACTS

- Miller, S.A., Fitzenz, D.D., 1999, The Izmit, Turkey (Mw=7.4) Earthquake as a direct test of an earthquake model, *AGU Fall meeting (poster)*.
- Fitzenz, D.D., Miller, S.A., 2000, Forward modeling of fault systems controlled by tectonics and crustal fluids: a strong link between field and laboratory observations and modeling techniques, *Swiss Tectonic Group Meeting STSGS (oral)*.
- Fitzenz, D.D., Miller, S.A., 2000, Forward modeling of a coupled thrust/strike-slip fault system controlled by tectonics and crustal fluids, *European Geological Society (oral)* .
- Fitzenz, D.D., Miller, S.A., 2000, Time Evolution of a Generic Coupled Blind Thrust/Strike-Slip Fault System Controlled by Tectonics and Crustal Fluids, *AGU Fall Meeting (oral)*.
- Miller, S.A.,Fitzenz, D.D., 2000, The Dynamical and Self-organizing Influence of Fluids on the Earthquake Process, *AGU Fall Meeting (poster)*.
- Fitzenz, D.D., Miller, S.A., 2001, A 3-D fault interaction model to investigate the topographical process associated with active tectonics, *European Union of Geophysics (poster)*.
- Fitzenz, D.D., Miller, S.A., 2001, The SAFOD project: an opportunity to combine field and laboratory data to constrain forward modeling parameters, *EarthScope Workshop*.

- Fitzenz, D.D., Miller, S.A., 2001, First Results from a Forward, 3-Dimensional Regional Model of a Transpressional San Andreas Fault System, *AGU Fall Meeting (oral)*.

PUBLICATIONS

- Dominique, P., A. Autran, J.-L. Bles, D.D. Fitzenz, F. Samarq, M. Terrier, M. Cushing, J.-C. Gariel, B. Mohammadioun, Ph. Combes, Ch. Durouchoux and X. Goula, 1998, Part two: Probabilistic approach: Seismic hazard map of the national territory (France), *Proc. 11th Europ. Conf. on Earthquake Engineering, CD, Paris Sept. 98*.
- Fitzenz, D.D. and S.A. Miller, 2001, A Forward Model for Earthquake Generation on Interacting Faults Including Tectonics, Fluids, and Stress Transfer, *J. Geophys. Res., Vol.106 , B11 , p.26,689*.
- Fitzenz, D.D. and S.A. Miller, 2002, Fault compaction and overpressured faults: Results from a 3D model of a ductile fault zone, submitted to *Geophysical Journal International*.